UNIVERSITY OF CALIFORNIA

Los Angeles

Solution-Processed Magnetic and Magnetoelectric Materials for the Development of Future Low Power Devices

A dissertation submitted in partial satisfaction of the
requirements for the degree of Doctor of Philosophy
in Chemistry

by

Shreya Kiritbhai Patel

2023

ABSTRACT OF THE DISSERTATION

Solution-Processed Magnetic and Magnetoelectric Materials for the

Development of Future Low Power Devices

by

Shreya Kiritbhai Patel

Doctor of Philosophy in Chemistry

University of California, Los Angeles, 2023

Professor Sarah H. Tolbert, Chair

In this thesis, we focus on designing new material systems that could help reduce Ohmic loss to enable future, low-power electro-magnetic devices. The first part of this thesis details *voltage*-control magnetism, which contrasts to conventional *current*-controlled magnetism. We

specifically investigate strain-mediated magnetoelectric composites, which couple a ferroelectric material that strains in response to a voltage, to a magnetostrictive material, which changes magnetization in response to strain. We introduce a new category of magnetoelectric nanocomposites with residual porosity engineered into them. In the synthesis, block-copolymer templating is used to create a porous ferromagnetic framework, and then atomic layer deposition (ALD) is used to partly coat the inside of the pores with ferroelectric material. Residual porosity increases the mechanical flexibility of the composites, and thus allows for more fully-realized magnetoelectric coupling than conventional layered composites. Thus, we find large (> 50 %) changes in magnetization in samples with the most residual porosity.

While the first part of this thesis focuses on making nanostructured magnetoelectric materials, the second part of this thesis discusses our work in building new bulk/thin-film spintronic materials. For the ideal spintronic device material, low magnetic loss and high magnetostriction are desirable, but spin-orbit coupling prevents both from occurring in the same material. Here we study systems based on yttrium iron garnet (YIG), a low magnetic loss material, and dope them to increase their magnetostriction. Using sol-gel chemistry, we surveyed a range of dopant stoichiometries of Ce:YIG and Ru:YIG, and made the exciting discovery that Ru:YIG films actually exhibit lower Gilbert damping than undoped YIG, which has previously been predicted by Kittel. Since inhomogeneous broadening is quite large in these polycrystalline films due to magnon scattering at grain boundaries, we turned to polymer-assisted deposition, a solution-based method that allows for the deposition of epitaxial films. Interestingly, we found that Ru:YIG films grown on (111) GGG exhibited perpendicular magnetic anisotropy, which necessitates high magnetostriction. Furthermore, these films were found to have lower damping than undoped YIG, echoing previous findings in sol-gel films. Thus, we have shown that low-cost solution-phase methods can be used to produce high-magnetostriction, low-magnetic-loss materials for potential spintronic applications.

This dissertation of Shreya Kiritbhai Patel is approved.

Justin R. Caram

Alexander M. Spokoyny

Jane P. Chang

Sarah H. Tolbert, Committee Chair

University of California, Los Angeles

2023

To my parents, whose sacrifices gave me the opportunity to become a doctor, and my brother, whose sense of humor got me through the process.

TABLE OF CONTENTS

LIST OF FIGURES

Chapter 2. Strain Transfer in porous multiferroic composites of $CoFe_2O_4$ and $PbZr_xTi_{1-x}O_3$

Chapter 3. Increased Magnetoelectric Coupling in Porous Nanocomposites of $CoFe_2O_4$ and $BiFeO_3$ with Residual Porosity for Switchable Magnetic Devices

Chapter 6. Perpendicular Magnetic Anisotropy in Solution-Processed Epitaxial Ru-doped Yttrium Iron Garnet Thin Films

Appendix A. Supporting Information for Chapter 3

Appendix B. Supporting Information for Chapter 4

Appendix C. Supporting Information for Chapter 5

Appendix D. Supporting Information for Chapter 6

LIST OF TABLES

Chapter 5. Delineating magnetization dynamics in solution-processed doped yttrium iron garnet thin films

Chapter 6. Perpendicular Magnetic Anisotropy in Solution-Processed Epitaxial Ru-doped Yttrium Iron Garnet Thin Films

ACKNOWLEDGEMENTS

This thesis would not be possible had it not been for the sacrifices my parents and grandparents made for me. Therefore, I first want to thank my biggest cheerleaders, my family. My dad taught me to work hard and to take risks, both of which have made me a better scientist. My mom has comforted me through some of the most challenging points of graduate school, and I would not have been able to do this without her. My little brother, Kevan, made me laugh through some of the toughest times and really put things in perspective when I needed it most. Outside of my immediate family, I would like to thank my close friends who have supported me throughout my career. I particularly want to thank my 'flock', Brittony, Victoria, and Chelsea, who have been rooting for me from the start.

I want to thank the many professors I had before even coming to graduate school. Most people are lucky if they get one or two good professors in their undergraduate study that inspires them, I was lucky to have all of my professors at Southern Methodist University have that kind of impact on me. First, I have to thank my undergraduate research advisor, Alex. I had always known that he was an amazing undergraduate research advisor, but I fully came to appreciate everything he taught me in graduate school. I came to UCLA with so many skills thanks to his above-and-beyond dedication to my career. Alex fostered my scientific creativity and pushed me to challenge the bounds of what I thought was possible. Even to this day, he still mentors and advises me. I would also like to thank Dr. O'Brien, who was the professor who inspired me to pursue a career in chemistry and who jump-started my research career. I would never have ended up in chemistry had it not been for her. I'd also like to thank my other SMU professors, Dr. Patty, Dr. Lattman, and Dr. Son, all of whom went above and beyond to help me pursue my chemistry career and inspire me to want to become a professor one day.

Of course, I have to thank Sarah for being the best PhD advisor I could have asked for. Anyone that has met Sarah knows that she is an outstanding teacher. She is an excellent scientific communicator and has taught me so much of what I know about how to make physical chemistry approachable at all levels. She is also incredibly patient. I am not an easy graduate student to handle. I like to take a lot of risks, but with risk, comes some broken equipment and lots of mistakes. Despite this, Sarah's always encouraged me to try new things, which has molded me into a better scientist. Sarah goes above and beyond for her students, even if that means staying up through the night to get the work done. She defends and protects her students, particularly those that come from disadvantaged backgrounds. She is truly an amazing role model and I consider myself so lucky to have done my PhD with her.

One of the best parts of working for Sarah is being a part of the Tolbert research group, which has given me some of the best colleagues and friends I could have ever asked for. Of course, I would like to thank the magnetics subgroup, Stephen, Ty, Jeff, Kat, and Ethan, whom have been truly outstanding collaborators and close friends. The magnetics subgroup always sticks together (pun intended). Magnetics is a tough field, and so I am so grateful to have had an amazing subgroup to work in. Ty was an outstanding mentor and teacher who taught me much of what I know about the complexities of magnetics systems. Jeff and Kat have not only been great people to work with, but also great friends – thank you both for cheering me on when I had a bad day and helping me wherever you could in every way possible. Ethan, my mentee, has also been wonderful to work with and easy to teach. He's grown so much as a scientist already in the short time I've known him, and I am excited to see where he takes the project in the coming years.

In addition to the magnetics subgroup, I would like to thank my other fellow tolbies: Yiyi, Edgar, Joe, Shanlin, Yutong, Helen, Casey, Spencer, David, Susan, Kodi, Nesibe, Grace, and

Xinyu, all of whom made working in the Tolbert lab so enjoyable. In particular, I'd like to thank KJ and Patrick, who are close friends and have been like second mentors to me, and were always there for me to give me advice on science and life generally. I would like to thank Vivian, Tori, Andrew, and Sophia who have both been great colleagues have remained close friends even after they have graduated. Of course, I'd like to thank my adoptive Tolbert lab cohort, Natalie, Danny, and Charlene. Natalie - I would not want to be constantly mistaken for anyone else, it's truly been an honor. Danny has been a huge part of my thesis, both scientifically (all the beautiful TEMs in my thesis came from Danny) and as a friend, as he has always been there to encourage me when I'm down and celebrate with me when something (finally) works. I will greatly miss our weekly (maybe biweekly) climbing sessions, our dinner parties, and just being able to nerd out on all things science with you. I also have to thank my labmate-turned-roommate, Charlene. We've shared an office, an apartment, and sometimes it feels like we share one brain. While he is not a tolbie, I also want to thank my first friend at UCLA, Zach. We have been through it all together since day one and, six years later, I am so proud of us for making it to the finish line.

My doctoral work was supported by the NSF Translational Applications of Nanoscale Multiferroic Systems Engineering Research Center (TANMS-ERC). I have been so lucky to not only have had amazing coworkers in the Tolbert lab, I also have had incredible colleagues in TANMS-ERC who have helped me take my research in directions I never imagined would be possible. I'd first like to thank Professor Greg Carman, the center leader, who has essentially been a second advisor to me. Greg has given me constant and unwavering support, mentoring me in both science and life generally. Greg has always made room for me to have a voice in the center and always ensured that I had 'a seat at the table'. I am so grateful for his guidance. I'd also like to thank Tsai-Tsai and Michelle, the glue that holds TANMS-ERC together. Both of them have

facilitated so much behind the scenes and have always been around when I just want to talk, I am so lucky to have met them in TANMS. I would like to thank my colleagues that I've worked with in the materials thrust, including Professor Chang, Kevin, Adrian, Professor Sun, Cunzheng, Alex, Suraj, Professor Salahuddin, Adi, and Mohan, for their help with nearly all of my research. Additionally, I would like to thank Emily, Siddhant, Ben, Paymon, Ruoda, Yu-ching, Nancy, Tao, and Devin, who all helped me with various parts of my research and have all been wonderful to work with. They honestly pushed my research into directions I never imagined possible. Outside of science, these people are wonderful to work with and have also become close friends. As a part of TANMS, I undertook many education efforts, including the Research Experiences in Mentoring program (REM), the Research Experiences for Undergraduates program (REU), the Undergraduate Research Program (URP) and the development of a Mathematics, Engineering, Science, Achievement (MESA) high-school course, all of which were overseen by Dr. Pilar O'Cadiz. Pilar has been a great maternal presence within TANMS and truly goes above and beyond for its students, including myself. I would like to thank Malcom, Matthew, Victor, Michael, Kevin, and Adrian, who also were heavily involved in these efforts and so became my close friends, making my time working in these programs so much fun.

I would like to thank the rest of my committee as well. I'm not even in their groups, but Justin and Alex have both advised me in my career as if I was one of their group members. Justin and I started at UCLA at the same time, which is when I was making a big jump from organic chemistry to physical chemistry. I was nervous to make this jump because I barely survived my quantum course in college, but Justin encouraged me and made me feel welcome in the field. Similar to Sarah, he's a great scientific communicator, so he helped me gain confidence in my skills. Alex has also always supported me. He cares so much about broadening participation

amongst underrepresented groups, which I witnessed first-hand when we served on the chemistry department graduate school admissions committee together. I would also like to thank Professor Chang for being on my committee. Throughout the years, we've worked together on a number of scientific collaborations, community outreach efforts, and leadership roles within TANMS-ERC, and she's been great to work with on all fronts.

Finally, I'd like to thank some of the staff scientists that helped me with my research. First, I would like to thank Dr. Ignacio Martini for all his help with much of the instrumentation I used in my research. I'd also like to thank Dr. Bob Taylor for his help with electron paramagnetic resonance and the staff at the Center for High Frequency Electronics for their help with other RF measurements. The cleanroom staff were incredibly helpful and insightful, particularly Krissy, Tony, Joe, Angelica, and Lorna. I would also like to thank Dr. Bart A. Johnson, Dr. Kevin H. Stone, Dr. Christopher Tassone, and Dr. Vivek Thampy, all of whom were instrumental in the high-resolution diffraction experiments performed at Stanford Synchrotron Radiation Lightsource.

A. Previous Publication and Contributions of Co-Authors

Chapter 2 is the published version of Abraham N. Buditama, Kevin Fitzell, Diana Chien, C. Ty Karaba, Shreya K. Patel, Hye Yeon Kang, Jane P. Chang, and Sarah H. Tolbert's manuscript titled "Strain Transfer in porous multiferroic composites of $CoFe_2O_4$ and $PbZr_xTi_{1-x}O_3$". Professor Tolbert and Professor Chang supervised the research. Abraham, Kevin, Diana, and Ty synthesized the multiferroic nanocomposite. Abraham, Kevin, Diana, Ty, Hye Yeon, and I performed the experiments. Professor Tolbert, Abraham Buditama, and I wrote the manuscript. All remaining authors gave approval for the final version of the manuscript.

Chapter 3 is the published version of Shreya K. Patel, C. Ty Karaba, Daniel D. Robertson, Jeffrey Chang, Kevin Fitzell, Charlene Z. Salamat, Jane P. Chang and Sarah H. Tolbert's

manuscript titled "Increased Magnetoelectric Coupling in Porous Nanocomposites of $CoFe_2O_4$ and $BiFeO_3$ with Residual Porosity for Switchable Magnetic Devices". Ty and I contributed equally to the manuscript. Professor Tolbert and Professor Chang supervised the research. Jeffrey, Kevin, and I synthesized the multiferroic nanocomposite – Ty and I made the porous CFO framework, then Jeffrey and Kevin filled the inside of the pores with ferroelectric BFO using atomic layer deposition. Ty, Daniel, Charlene, Jeffrey, and I performed the experiments. Professor Tolbert and I wrote the manuscript. All remaining authors gave approval for the final version of the manuscript.

Chapter 4 is the published version of Shreya K. Patel, Daniel D. Robertson, Suraj S. Cheema, Sayeef Salahuddin, and Sarah H. Tolbert's manuscript titled "*In-situ* Measurement of Magnetoelectric Coupling and Strain Transfer in Multiferroic Nanocomposites of $CoFe_2O_4$ and $Hf_{0.5}Zr_{0.5}O_2$ with Residual Porosity". Professor Tolbert and Professor Salahuddin supervised the research. Suraj and I synthesized the multiferroic nanocomposite – I made the porous CFO framework, then Suraj filled the inside of the pores with ferroelectric HZO using atomic layer deposition. Suraj, Daniel, and I performed the experiments. Professor Tolbert and I wrote the manuscript. All remaining authors gave approval for the final version of the manuscript.

Chapter 5 is the published version of Shreya K. Patel, C. Ty Karaba, and Sarah H. Tolbert's manuscript titled "Delineating magnetization dynamics in solution-processed doped yttrium iron garnet thin films". Ty and I contributed equally to this paper. Professor Tolbert supervised the research. Ty and I synthesized the doped YIG films – Ty synthesized the Ru-doped series, and I synthesized the Ce-doped series. Ty and I performed all the experiments. Professor Tolbert and I wrote the manuscript. All remaining authors gave approval for the final version of the manuscript.

Chapter 6 is the published version of Shreya K. Patel, Michael E. Liao, Dorian Luccioni, Ethan J. Savage, Charlene Z. Salamat, Mark S. Goorsky, and Sarah H. Tolbert's manuscript titled "Perpendicular Magnetic Anisotropy in Solution-Processed Epitaxial Ru-doped Yttrium Iron Garnet Thin Films". Professor Goorsky and Professor Tolbert supervised the research. I synthesized the doped YIG films. Michael, Dorian, Ethan, Charlene, and I performed all the experiments. Professor Tolbert and I wrote the manuscript. All remaining authors gave approval for the final version of the manuscript.

The research presented in this dissertation was directed by Professor Sarah H. Tolbert and was supported by: The National Science Foundation Nanosystems Engineering Research Center for Translational Applications of Nanoscale Multiferroic Systems (TANMS) under Cooperative Agreement Award No. EEC-1160504 and the National Science Foundation Graduate Research Fellowship under Grant Nos. DGE-1650604 and DGE-2034835. Much of the diffraction data presented here was collected at the Stanford Synchrotron Radiation Lightsource, a national user facility operated by Stanford University on behalf of the U.S. Department of Energy, Office of Basic Science under contract DE-AC02-76SF00515. This work makes use of the California NanoSystems Institute (CNSI), including the Nanoelectronics Research Facility, the Molecular Instrumentation Center, and the Electron Imaging Center for NanoMachines (supported in part by the NIH (1S10RR23057 to ZHZ). This work heavily relies on superconducting quantum interference device (SQuID) magnetometry, purchased with support from the NSF-MRI award 1625776. Electron paramagnetic resonance was collected using a Bruker EMXplus, purchased with the support of NSF-MRI award 2117480.

VITA

Education

University of California, Los Angeles — **Los Angeles, CA**
Ph.D. Track Chemistry – Materials Concentration — (*expected*) June 2023

M.S. Chemistry – Materials Concentration March 2019
Advanced to Candidacy September 2019

Southern Methodist University **Dallas, TX**
Bachelor of Science: Chemistry May 2017

Publications

1. **Patel, S. K.**; Lippert, A. R. (Southern Methodist University) "System and Method for a Three - Dimensional Optical Switch Display (OSD) Device." U.S. Provisional Patent Application 62,293,128, filed October 9, 2015.
2. **Patel, S. K.**; Lippert, A. R. (Southern Methodist University) "System and Method for a Three - Dimensional Optical Switch Display (OSD) Device." U.S. Patent Application 15,287,906, filed October 7, 2016.
3. **Patel, S. K.**; Cao, J.; Lippert, A. R. "A Volumetric Digital Light 3D Photoactivatable Dye Display." *Nature Commun.* **2017**, *8*, 15239. doi:10.1039/C7AY01238A.
4. Li, B.; Haris, U.; Aljowni M.; Nakatsuka, A.; **Patel, S.K.**; Lippert, A.R. "Tuning the Photophysical Properties of Spirolactam Rhodamine Photoswitches." Cover article, *Isr. J. Chem*. **2020**, *61*, 244-252. https://doi.org/10.1002/ijch.202000083.
5. Buditama, A.N.; Fitzell, K.; Chien, D.; Karaba, C.T.; **Patel, S.K**.; Kang, H.; Chang, J.P.; Tolbert, S.H. "Strain Transfer in Porous Multiferroic Composites of $CoFe_2O_4$ and $PbZr_xTi_{1-x}O_3$" *Appl. Phys. Lett.* **2022,** *120*, 192902. https://doi.org/10.1063/5.0090702.
6. Huang, S.; Karaba, C.T.; **Patel, S.K.**; Neal, A.; Tolbert, S.H.; Marian J. "Understanding the non-monotonic strain response of nanoporous multiferroic composites under electric field control" *Appl. Phys. Lett.* **2022**, *120*, 213501. https://doi.org/10.1063/5.0090252.
7. **Patel, S.K.**; Karaba, C.T.; Chang, J.; Fitzell, K.; Chang, J.P.; Tolbert, S.H. "Increased Magnetoelectric Coupling in Porous Composites of $CoFe_2O_4$ and $BiFeO_3$ with Residual Porosity" *ACS Appl. Nano Mater*. **2023**, *6*, 4141-4150. https://doi.org/10.1021/acsanm.2c04888.
8. **Patel, S.K**.; Karaba, C.T.; Tolbert, S.H. "Delineating Magnetization Dynamics in Solution-Processed Doped Yttrium Iron Garnet Thin Films*" J. Appl. Phys*. **2023**, *133*, 014102. https://doi.org/10.1063/5.0119353.
9. Will-Cole, A.R.; Hart, James L.; Mattzelle, M.; Podpirka, A.; Battacharjee, N.; **Patel, S.K.;** Tolbert, S.H.; Bansil, A.; Cha, J.J.; Heiman, D.; Sun, N.X. "Antiferromagnetic $FeTe_2$ 1T-phase formation at the $Sb_2Te_3/Ni_{80}Fe_{20}$ Interface" *Phys. Rev. Mater.* **2023**, *7*, 024406. https://doi.org/10.1103/PhysRevMaterials.7.024406.
10. **Patel, S.K.**; Robertson, D.D.; Cheema, S.S.; Salahuddin; S., Tolbert, S.H. "*In-situ* measurement of magnetoelectric coupling in multiferroic nanocomposites with residual porosity" *Nano Lett.* **2023**, *23*, 3267-3273. https://doi.org/10.1021/acs.nanolett.3c00083.
11. **Patel, S.K**.; Liao, M.E.; Luccioni, D.; Robertson, D.D.; Salamat, C.Z.; Savage, E.J.; Will-Cole, A.; Sun, N.X.; Goorsky, M.S.; Tolbert, S.H. "Perpendicular Magnetic Anisotropy in Solution-Processed Epitaxial Ru-doped Yttrium Iron Garnet Thin Films" *In preparation.*

Awards and Honors

1. Hanson-Dow Excellence in Teaching Award *September 2018*
2. National Science Foundation Graduate Research Fellowship *June 2019*
3. TANMS-ERC Perfect Pitch Competition Honorable Mention *September 2019*

4. Chen & Liang Inspiring Multiferroic Brilliance (CLIMB) Award *May 2022*
5. International Institute for Nanotechnology (IIN) Postdoctoral Fellowship *January 2023*
6. James D. McCullough Dissertation Award *June 2023*
7. National Science Foundation Mathematical and Physical Sciences Ascending (MPS-Ascend) Postdoctoral Research Fellowship *June 2023*

Presentations

1. American Chemical Society (ACS) National Meeting in Philadelphia (August 2016) "Synthesis and spectroscopic investigations of fluorescent photoswitches for use in optical materials." **Shreya K. Patel**, Jian Cao, Alexander R. Lippert
2. American Chemical Society (ACS) National Meeting in San Francisco (April 2017) "A Volumetric Three- Dimensional Digital Light Photoactivable Dye Display." **Shreya K. Patel**, Jian Cao, Alexander R. Lippert.
3. DFW Regional American Chemical Society (ACS) Meeting (April 2017) "Volumetric 3D Digital Light Photoactivatable Dye (3D Light PAD) Display." **Shreya K. Patel**, Alexander R. Lippert.
4. Translational Applications of Nanoscale Multiferroic Systems NSF Engineering Research Center (TANMS-ERC) Annual Site Review (June 2018) "Solution-Processed Yttrium Iron Garnet Thin Films as Novel Magnetostrictive Materials." **Shreya K. Patel**, Christopher T. Karaba, Sarah H. Tolbert.
5. Translational Applications of Nanoscale Multiferroic Systems NSF Engineering Research Center (TANMS-ERC) Annual Research Strategy Meeting Conference (January 2019) "Increasing Magnetoelectric Coupling in Nanocomposites of Bismuth Ferrite and Cobalt Ferrite." **Shreya K. Patel**, Christopher T. Karaba, Sarah H. Tolbert.
6. Translational Applications of Nanoscale Multiferroic Systems NSF Engineering Research Center (TANMS-ERC) Annual Site Review (June 2019) "Increasing Magnetoelectric Coupling in Nanocomposites of Bismuth Ferrite and Cobalt Ferrite." **Shreya K. Patel**, Christopher T. Karaba, Sarah H. Tolbert.
7. Conference on Magnetism and Magnetic Materials in Las Vegas (November 2019) "Solution-Processed Yttrium Iron Garnet Thin Films as Novel Magnetostrictive Materials." **Shreya K. Patel**, Christopher T. Karaba, Sarah H. Tolbert.
8. Translational Applications of Nanoscale Multiferroic Systems NSF Engineering Research Center (TANMS-ERC) Annual Research Strategy Meeting Conference (January 2020) "Solution-Processed Yttrium Iron Garnet Thin Films as Novel Magnetostrictive Materials." **Shreya K. Patel**, Sarah H. Tolbert.
9. Translational Applications of Nanoscale Multiferroic Systems NSF Engineering Research Center (TANMS-ERC) Annual Site Review (June 2020) "Solution-Processed Magnetostrictive Materials for Multiferroic Antenna Applications" **Shreya K. Patel**, Sarah H. Tolbert.
10. Translational Applications of Nanoscale Multiferroic Systems NSF Engineering Research Center (TANMS-ERC) Annual Research Strategy Meeting Conference (January 2021) "Solution-Processed Yttrium Iron Garnet Thin Films as Novel Magnetostrictive Materials." **Shreya K. Patel**, Sarah H. Tolbert.
11. Translational Applications of Nanoscale Multiferroic Systems NSF Engineering Research Center (TANMS-ERC) Annual Research Strategy Meeting Conference (January 2021)

"Solution-Processed Yttrium Iron Garnet Thin Films as Novel Magnetostrictive Materials." **Shreya K. Patel**, Sarah H. Tolbert.

12. Materials Research Society (MRS) Spring Meeting and Exhibit (April 2021) "Solution-Processed Yttrium Iron Garnet Thin Films as Novel Magnetostrictive Materials." **Shreya K. Patel**, Ty Karaba, Sarah H. Tolbert.
13. Translational Applications of Nanoscale Multiferroic Systems NSF Engineering Research Center (TANMS-ERC) Annual Research Strategy Meeting Conference (January 2022) "Controlling Strain Transfer in Porous Multiferroic Composites through Nanoscale Structure." **Shreya K. Patel**, Sarah H. Tolbert.
14. Materials Research Society (MRS) Fall Meeting and Exhibit (November 2022) "Controlling Strain Transfer in Porous Multiferroic Composites through Nanoscale Structure." **Shreya K. Patel**, Ty Karaba, Sarah H. Tolbert.

CHAPTER 1

Introduction

Conventional electronic and magnetic devices have become very difficult to downsize since their operation relies on current. Current generates heat, known as Ohmic loss, and as devices get smaller, these losses become so large that devices cannot function properly. Thus, it is essential to mitigate Ohmic loss to make devices smaller and more energy efficient. The central focus of this thesis has thus been building new materials systems that mitigate Ohmic loss for the development of future, low-power devices.

In the first part of this thesis, we discuss a new avenue to reducing Ohmic loss in magnetic devices by using voltage to control magnetism, rather than current. Here, we utilize strain-mediated composites that can couple electricity and magnetism through strain. Such composites couple a ferroelectric material, which strains in response to a voltage, to a magnetostrictive material, which changes magnetization in response to stress. Thus, voltage control of magnetism is achieved through strain. Dense, layered composites have been successful to this end, but we seek to push the magnetoelectric coupling in such composites even further. Nanostructuring strain-mediated composites, so that there is maximal interfacial surface area between the magnetostrictive and ferroelectric material, has been a proven strategy in improving the magnetoelectric coupling between the two materials. Here, we push the performance of nanostructured strain-mediated composites even further by introducing residual porosity into the composite. We synthesize these composites in two steps; first, we utilize block copolymer templating to create a porous magnetostrictive framework, and second, we utilize atomic layer deposition to coat the inside of the pores with ferroelectric materials. We have found that residual porosity leaves room for the pores to flex, allowing for greater strain and thus magnetization

changes than composites with no residual porosity. We've built a whole series of nanostructured magnetoelectric composites with residual porosity to fully understand this system.

The first composite in this series utilized lead zirconate titanate ($PbZr_xTi_{1-x}O_3$, or PZT) as our ferroelectric and cobalt ferrite ($CoFe_2O_4$, or CFO) as our magnetostrictive material to make PZT-CFO nanocomposites. In the second chapter of this thesis, we discuss a new technique to use synchrotron-enabled high-resolution X-ray diffraction to measure very small strain changes in PZT-CFO composites. While work on the PZT-CFO composites was exciting, we set out to improve upon this system. One of the largest challenges to magnetoelectric coupling in the PZT-CFO composites is that the ferroelectricity is much less stabilized in the ultrathin film regime we utilize in the nanocomposites here (2 - 3 nm). We then focused on optimizing this system for better magnetoelectric coupling by using bismuth ferrite ($BiFeO_3$, or BFO) as our ferroelectric, since it is less sensitive to thickness scaling than PZT. This work is described in the third chapter of this thesis. The BFO-CFO composites resulted in remarkable magnetoelectric coupling, exhibiting almost a 60% decrease in magnetization with electrical poling. Finally, we made a third nanocomposite in this series, utilizing a relatively new ferroelectric known as hafnium zirconium oxide ($Hf_{0.5}Zr_{0.5}O_2$, or HZO). Unlike most ferroelectrics, HZO is better stabilized in the ultrathin regime used in the nanocomposites, so it was a natural material choice. In chapter four, we therefore synthesize HZO-CFO composites and study their magnetoelectric coupling. Importantly, in this work, we utilize *in-situ* electrical poling in both the magnetization and the strain measurements, allowing us to measure and understand the magnetoelectric and strain coupling more than ever before.

In the second part of this thesis, we switch gears to discussion of our work in building new materials for spintronic devices. Electronics operate by forcing electrons through a circuit, but

their spintronic device analogues use spin waves, or collective oscillations of the spin of electrons, to perform the same functions and can therefore be made much more energy-efficient than electronics. For spintronic device functionality, spin waves need to be able to propagate through a magnetic material for as long of a distance as possible, or in other words, need to have low magnetic loss. Thus, for the ideal spintronic material, we would like something with low magnetic loss and high magnetostriction, but spin-orbit coupling prevents both from occurring in the same material. While most efforts to generate spintronic materials aim to take a metallic, high-magnetostriction material and lower its losses, here, we take an insulating, low magnetic loss material and attempt to increase its magnetostriction. Specifically, we focus on yttrium iron garnet ($Y_3Fe_5O_{12}$, or YIG), as it is one of the lowest magnetic-loss materials known.

In this thesis, we have built a library of doped YIG materials. In chapter five of this thesis, we synthesize a series of YIG thin films using sol-gel chemistry. We doped YIG with both cerium (substituting at the yttrium site) and ruthenium (doping in at the iron site) in order to increase its spin-orbit coupling, which is known to increase YIG's magnetostriction. We perform a wide range of dynamic magnetic characterization to delineate the magnetic losses in these materials, and show that there is a regime in ruthenium-doped YIG where YIG can be doped without increasing magnetic loss, as predicted by modelling from Kittel. In the final chapter of this thesis, chapter six, we build on this work to build practical spintronic materials. We found that the sol-gel chemistry resulted in polycrystalline films, which increased the magnetic loss due to spin wave scattering at the grain boundaries. Instead, we utilized polymer-assisted deposition, which allows us to synthesize epitaxial films while maintaining the advantages of solution-based chemistry (i.e. cost effectiveness and scalabilities). We tested both the effect of depositing on two different orientations of substrate (one with a more anisotropic face) and ruthenium-doping. Most magnetic

films have a magnetic preference for the in-plane direction. However, in this work, we found that both using a more anisotropic orientation of substrate and Ru-doping resulted in perpendicular magnetic anisotropy (PMA), or out-of-plane preference for magnetization. This finding is very desirable for spintronic devices, since it allows devices to be integrated with existing top-down read-write memory heads. We find that these films also have lower magnetic loss, since they also fit into modelling by Kittel discussed in chapter 5. Thus, we have built materials practical for spintronic devices.

CHAPTER 2.

Strain Transfer in porous multiferroic composites of $CoFe_2O_4$ and $PbZr_xTi_{1-x}O_3$

Chapter 2 describes strain transfer in mesoporous multiferroic nanocomposites of cobalt ferrite and lead zirconate titanate, where high-angular resolution X-ray diffraction was used to measure strain in the ferroelectric and strain transfer to the magnetic material.

This chapter was reproduced from Buditama, A.N.; Fitzell, K.; Chien, D.; Karaba, C. Ty; Patel, S.K.; Kang, H.; Chang, J.P.; Tolbert, S.H. "Strain Transfer in porous multiferroic composites of $CoFe_2O_4$ and $PbZr_xTi_{1-x}O_3$". *J. Appl. Phys.* **2023**, *133*, 014102, with the permission of AIP Publishing.

Strain Transfer in Porous Multiferroic Composites of $CoFe_2O_4$ and $PbZr_xTi_{1-x}O_3$

Abraham N. Buditama,[1] Kevin Fitzell,[2] Diana Chien,[2] C. Ty Karaba,[1] Shreya K. Patel,[1] Hye Yeon Kang,[1] Jane P. Chang,[2,3,4*] and Sarah H. Tolbert[1,3,4,*]

Abstract

This manuscript examines the mechanism of strain-coupling in a multiferroic composite of mesoporous cobalt ferrite (CFO), conformally filled with lead zirconate titanate (PZT). We find that when the composites are electrically poled, remanent strain from the piezoelectric PZT layer can be transferred to the magnetostrictive CFO layer. X-ray diffraction shows that this strain transfer is greatest in the most porous samples, in agreement with magnetometry measurements, which show the greatest change in sample saturation magnetization in the most porous samples. Strain analysis shows that porosity both accommodates greater lattice strain and mitigates the effects of substrate clamping in thin film strain-coupled composites.

Multiferroics are materials that simultaneously exhibit more than one ferroic order parameter such as ferromagnetism or ferroelectricity; they are of interest because of their potential applications in a wide range of nanoscale devices.[1–3] In particular, magnetoelectric multiferroic materials couple a magnetic and an electric polarization, but single-phase materials that show this property at room temperature are rare.[1,2,4–7] Composite materials, however, offer another route to magnetoelectric behavior. Such materials generally use strain-coupling and consist of layers of piezoelectric and magnetostrictive materials. As an electric field is applied to the composite, the piezoelectric is strained, and this strain is transferred to the magnetostrictive material, which in turn affects the magnetization. This coupling allows the magnetization to be controlled by applied

electric fields, and vice versa.[8–16] Because this technique requires intimate coupling between the two phases, numerous synthetic methods and architectures of strain-coupled multiferroics have been investigated in the literature, including sequentially deposited two-dimensional stacks, spontaneously phase-separated nanopillar arrays, and other three-dimensional arrangements.[10,11,20–27,12–19]

We have recently shown that porosity is an important control parameter in the synthesis of multiferroic composites.[16] In our previous work, a mesoporous, magnetostrictive cobalt ferrite ($CoFe_2O_4$ or CFO) film was filled using atomic layer deposition (ALD) with piezoelectric lead zirconate titanate ($PbZr_xTi_{1-x}O_3$ or PZT). The result was an interconnected, three-dimensional network containing both CFO and PZT. The final porosity in such a composite can be controlled by the initial pore size, which is determined by the polymer template used in the synthesis of the initial mesoporous CFO, and the thickness of the deposited PZT layer. Our results showed that the final composite porosity was correlated to a change in magnetic saturation that could be achieved upon electrical poling. It was hypothesized that this correlation was due to a link between porosity and mechanical flexibility of the composite, but no direct evidence for that hypothesis was obtained. Here, we examine the mechanism of magnetoelectricity in these thin film composites by depositing a range of thicknesses of PZT in the mesoporous CFO framework and measuring the resultant voltage-dependent strain in the CFO framework.

The mesoporous CFO framework was synthesized using block copolymer–templating of sol-gel films, a technique that has been used to produce a wide range of metal oxide materials of varying nanoarchitectures.[28–37] The CFO sol was templated with an amphiphilic diblock copolymer that forms micelles in solution. As the solution is deposited, the micelles self-assemble

into periodic structures within the film. Upon pyrolysis, the polymer is removed, leaving a stable porous network of CFO.

This porous film is then conformally coated with PZT using ALD, which grants uniformity over the entire structure because this technique obtains layer-by-layer growth through a self-limiting surface reaction. Alternating pulses of gaseous precursors completely saturate all available surface sites, allowing conformal deposition over the entire porous network. ALD also allows for fine control over the thickness deposited, and thus over the final porosity of the composite material. This method thus provides new functionality compared to composites in the literature, which thus far have been dense structures that lack porosity. Here we aim to use high-resolution X-ray diffraction on films as a function of *ex situ* poling field to explore the mechanisms of strain coupling in this porous composite.

Synthetic details for both CFO and PZT have been discussed previously.[16,28,38] Briefly, poly((ethylene-*co*-propylene)-*block*-poly-(ethylene oxide) with a mass ratio of PEP(3900)-*b*-PEO(4000) was used to template a sol based on nitrate salts of Co and Fe. Films were dip-coated onto silicon wafers in a humidity-controlled chamber set to 10–20% relative humidity. The withdrawal rate was usually 2 mm/s but can be varied, depending on desired thickness. To form rigid inorganic/organic structures, the films were calcined in air at 80°C for 6 hours, at 130°C for 8 hours, and at 180°C for 6 hours for a total heating time of 24 h including temperature ramps. Once calcined, films were annealed at 550 °C with a 10 °C/min ramp for 5 minutes.

PZT was deposited via ALD using $Pb(TMHD)_2$, $Ti(O\text{-}i\text{-}Pr)_2(TMHD)_2$, and $Zr(TMHD)_4$ as precursors. PZT was deposited at no more than 180 °C in an amorphous form and then crystalized into tetragonal PZT by rapid thermal annealing at 700 °C under oxygen for one minute. Here, the PZT layer thicknesses range from 3 nm to 10 nm.

The morphology and thickness of the nanocomposites was confirmed using a JEOL JSM-6700F field-emission scanning electron microscopy (FE-SEM). Ellipsometric porosimetry (EP) was performed on a Semilab PS-1100 in the spectral range of 1.24 eV to 4.5 eV. A UV-vis CCD detector adapted to a grating spectrograph analyzes the signals reflected by the sample from a 75 W Hamamatsu Xe lamp. Toluene was used as the adsorbent and the EP analysis was performed using the associated SEA software. Angular-dependent X-ray diffraction (XRD) was collected at the Stanford Synchrotron Radiation Laboratory (SSRL) using beamline 7-2 at wavelengths λ = 0.9919 Å and 1.0332 Å. Magnetic measurements were carried out on a Quantum Design MPMS 5T SQUID magnetometer with RSO detection.

Because our previous work indicated the importance of residual porosity in multiferroic composites, we first characterized the porosity of the composites using ellipsometric porosimetry (EP). EP adsorption/desorption curves for samples with various PZT layers (Figure 1a) show that as thicker PZT layers are deposited, less porosity is observed. The samples with 0 nm and 3 nm of PZT show a distinct type IV isotherm, which signifies an

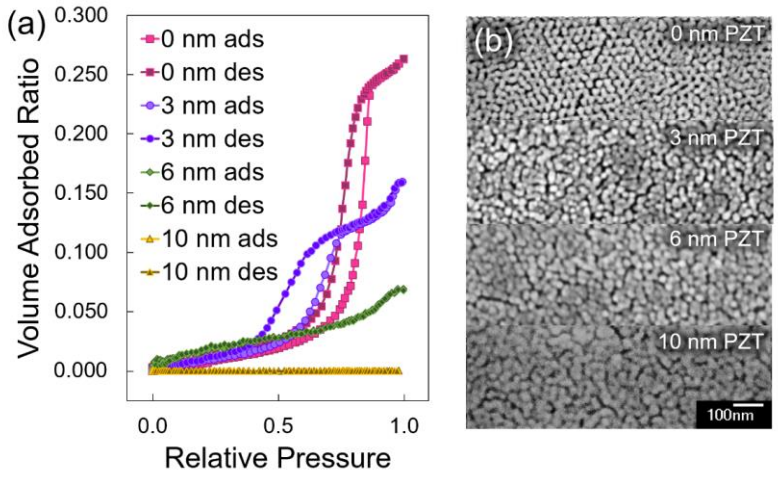

Figure 2-1. Ellipsometric porosimetry adsorption/desorption curves (a) show reduced porosity with increasing PZT thickness. Calculated porosity values are 26.0%, 15.3%, 6.6%, and 0.03%, respectively. SEM images (b) show gradual filling of the CFO framework. From the top, the CFO layer is filled with 0 nm, 3 nm, 6 nm, and 10 nm of PZT.

interconnected porous network. The calculated porosity values are 26.0% for the 0 nm PZT sample, 15.3% for 3 nm, 6.6% for 6 nm, and 0.03% for 10 nm. The PZT in these as deposited films are amorphous, but previous work[16] has shown that the PZT can be crystallized to the ferroelectric tetragonal phase. We find that redistribution of the PZT in the pores can block the small necks in the structure, impeding toluene access to the pores. As a result, SEM was used to characterize the samples after crystallization. SEM images of the samples with crystallized PZT layers (Figure 1b), from top to bottom, show reduced porosity as thicker PZT layers are deposited. The unfilled CFO framework exhibits ordered porosity, which is distorted by grain growth upon annealing of the PZT layer. For this reason, the 10 nm sample still appears to be somewhat porous by SEM, even though access into the porous interior is stopped by pore necks that had been completely stoppered by PZT, as seen from the EP adsorption/desorption curves.

To determine the magnetoelectric coupling of these thin film composites, they were electrically poled *ex situ* with the electric field applied

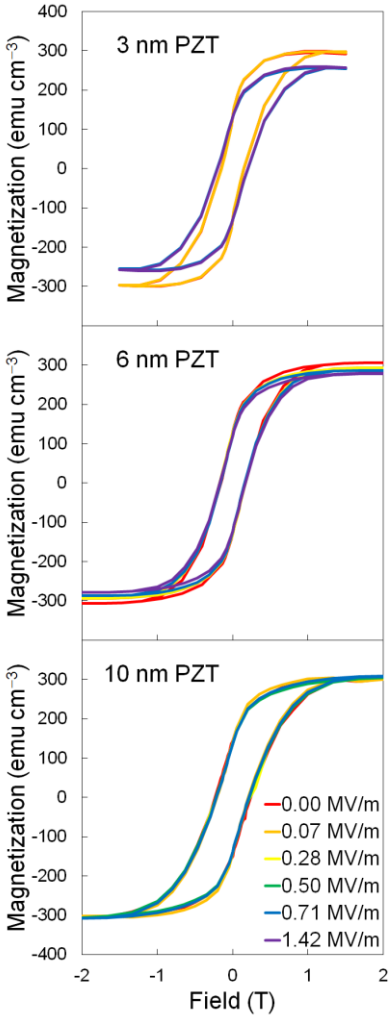

Figure 2-2. *M–H* loops of the CFO/PZT composites show a reduced change in magnetization saturation upon application of an electric field in less porous samples. The direction of the applied electric field and the measured magnetization were both out-of-plane (perpendicular to the sample substrate).

perpendicular to the sample surface (henceforth referred to as out-of-plane). The films were covered with a 13 μm polyvinylidene chloride spacer and physically sandwiched between two Al electrodes 1.28 cm in diameter. The nanocomposite was electrically poled for 10 min with applied electric fields ranging from 0 MV m^{-1} to 1.42 MV m^{-1}. As such, the strains and polarizations explored in this paper are remanent ones. While it is true that much of the strain and polarization will be lost upon removal of the applied field, the remanent polarization stabilizes within milliseconds and can be assumed to be constant throughout the measurement.[39,40]

Magnetization measurements show a decrease in out-of-plane saturation magnetization upon electrical poling, which is correlated with porosity of the composite (Figure 2). The sample with the thinnest PZT layer shows the largest change in saturation magnetization, and the sample with the thickest PZT shows hardly any change. Because polarization in ultrathin PZT is known to decrease with thickness,[41,42] this trend is likely due to the mechanical properties of the porous composite, rather than any favorable change in the PZT itself. The films with the thinnest PZT are also the ones with the highest porosity, and therefore the greatest mechanical flexibility, as pore flexion accommodates significant strain changes in the material.[28,29,43]

The role of porosity in magnetoelectric coupling is corroborated by strain analysis of the CFO layer. Synchrotron high-resolution XRD was used to probe the differences in both out-of-plane and in-plane (parallel to the substrate) lattice spacings. The CFO{311} and PZT{200} peaks were relatively well resolved and were treated as representative of overall strain changes in both materials. Because these films consist of polycrystalline CFO and PZT with no preferred orientation with respect to the substrate, any lattice plane can be used to report on the overall strain state of the material. As shown in Figure 3 and expected based on the magnetization data, the CFO{311} out-of-plane lattice spacing increased upon *ex situ* electrical poling, and the magnitude

of the change was directly correlated to the porosity of the composite. As the porosity decreased, the strain transferred upon electrical poling also decreased (Figure 3). CFO exhibits negative magnetostriction, and so out-of-plane tension directly corresponds to the reduced magnitude of change in out-of-plane magnetization saturation.

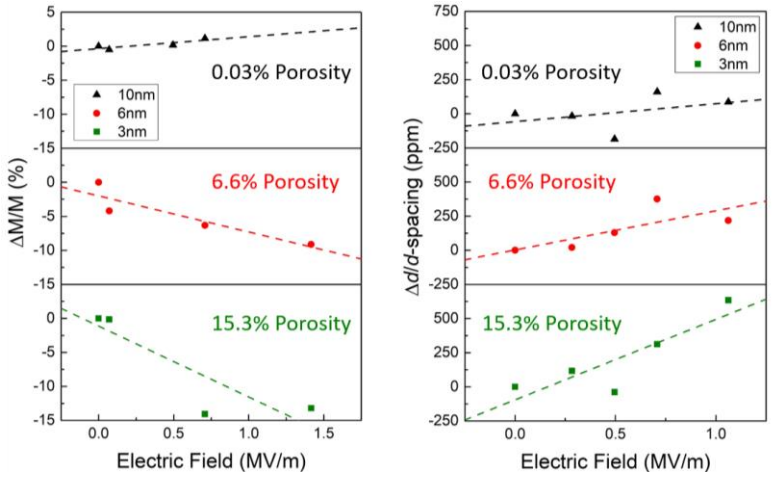

Figure 2-3. Samples with less PZT and thus greater porosity show greater change for both CFO out-of-plane saturation magnetization (a) and strain (b). The saturation magnetization is obtained from the data shown in Figure 2. The strain is calculated by measuring the peak shifts in the XRD spectra of the CFO{311} peak positions.

Even though CFO is not a piezoelectric, it is strain-coupled to one, and so we can calculate the strains when 1 MV m^{-1} has been applied and then removed from the sample. While this strain is not a real piezoelectric coefficient, it relates a remanent strain to an *ex situ* electric field, and so we give it the symbol d'_{33}. Values of d'_{33} ranging from d'_{33} = 590 × 10^{-12} m V^{-1} for the composite with the highest porosity (3 nm PZT), to d'_{33} = 130 × 10^{-12} m V^{-1} for the composite with lowest porosity (10 nm PZT), which is comparable to true piezoelectric coefficients of PZT.[44–46] These values demonstrate more than a fourfold reduction in strain transferred when porosity is removed from the sample. Again, we emphasize that these calculated values are not true piezoelectric coefficients because they relate the remanent strain to an *ex situ* applied field instead of the instantaneous strain to an *in situ* field; the instantaneous piezoelectric coefficient should be higher indeed.

No significant change upon electrical poling was found in the in-plane saturation magnetization nor in the CFO in-plane strain. The CFO framework is covalently bound to the substrate and is unable to move in plane because of substrate clamping. Because its strain is unchanged, the CFO in-plane magnetization is also unchanged. However, the PZT layer is deposited onto the CFO framework itself, and as such is not constrained by the substrate. As the PZT deforms due to the out-of-plane electric field, strain can be expressed as out-of-plane tension or in-plane compression. This strain is transferred to the clamped CFO framework and can be expressed only as the aforementioned out-of-plane tension. Interestingly, analysis of PZT strain reveals contribution from both in-plane compression and out-of-plane tension. Similar d' coefficients calculated for PZT show comparable strains to the CFO, but with more noise, because the PZT layer is mere nanometers thin and thus diffracted intensity is weaker. The greatest PZT strains are in the most porous sample (3 nm PZT) and are shown in Figure 4. The data shows changes in both in-plane and out-of-plane lattice constants, and demonstrate that the PZT is not at all substrate clamped. The strains are calculated to be $d'_{31} = -670 \times 10^{-12}\,\mathrm{m\,V^{-1}}$ in-plane and $d'_{33} = 130 \times 10^{-12}\,\mathrm{m\,V^{-1}}$ out-of-plane. These values are comparable to that of the CFO, suggesting that much of the strain had indeed been transferred.

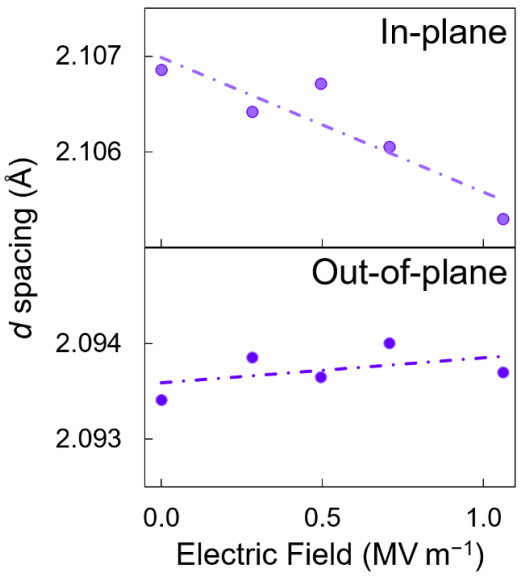

Figure 2-4. The magnitudes of the in-plane and out-of-plane PZT strains are comparable to those of the CFO. PZT strains are calculated by measuring the shifts in the XRD spectra of the PZT{200} peak positions.

Thus, from strain analysis of this free PZT layer, we see that three-dimensional porosity has an advantage over traditional two-dimensional structures where multiple layers are clamped together and to the substrate. In a three-dimensional structure like this one, the pore-filled material can remain unclamped if sufficient residual porosity is retained.

Overall, these experiments have allowed us to explore the mechanism of strain-coupling in porous magnetoelectric CFO/PZT composites. These thin films are composed of a templated mesoporous CFO framework, which is subsequently filled by ALD PZT of varying thicknesses. As the samples are electrically poled out-of-plane, X-ray diffraction shows that the piezoelectric PZT layer may exhibit both out-of-plane tension and in-plane compression. This strain is transferred to the magnetostrictive CFO layer, which results in decreased out-of-plane saturation magnetization as measured by SQUID magnetometry. The strain transfer is greatest in samples with the greatest porosity, as pore flexion accommodates greater strains in the material. This porous architecture thus offers not only greater mechanical flexibility than traditional composite architectures, but also mitigates the effects of substrate clamping for the ALD layer. Perhaps more importantly, the observation of in-plane compression in what could have been a clamped PZT layer provides insight into the use of porosity in the design of future porous multiferroic composites.

ACKNOWLEDGEMENTS.

This work was supported by the NSF Nanosystems Engineering Research Center for Translational Applications of Nanoscale Multiferroic Systems (TANMS) under Cooperative Agreement Award EEC-1160504. Additionally, author S.K.P acknowledges support from a National Science Foundation Graduate Research Fellowship under Grant No. DGE-1650604 and DGE-2034835. This work made use of the UCLA Molecular Instrumentation Center (MIC). This manuscript

contains data collected at the Stanford Synchrotron Radiation Lightsource (SSRL), experimental station 7-2. Use of the Stanford Synchrotron Radiation Lightsource, SLAC National Accelerator Laboratory, is supported by the U.S. Department of Energy, Office of Science, Office of Basic Energy Sciences under Contract No. DE-AC02-76SF00515.

CHAPTER 3.

Increased Magnetoelectric Coupling in Porous Composites of $CoFe_2O_4$ and $BiFeO_3$ with Residual Porosity

Chapter 3 describes mesoporous multiferroic nanocomposites of cobalt ferrite and bismuth ferrite, which demonstrates that porosity can allow for more efficient strain transfer and thus high magnetoelectric coupling.

This chapter was reprinted with permission from Patel, S.K.; Karaba, C.T.; Robertson, D.D.; Chang, J.; Fitzell, K.; Salamat, C.Z.; Chang, J.P.; Tolbert, S.H. "Increased Magnetoelectric Coupling in Porous Composites of $CoFe_2O_4$ and $BiFeO_3$ with Residual Porosity" *ACS Appl. Nano Mater.* **2023**, *6*, 4141-4150.

A reprint of the supporting information is given in Appendix A.

Increased Magnetoelectric Coupling in Porous Nanocomposites of $CoFe_2O_4$ and $BiFeO_3$ with Residual Porosity for Switchable Magnetic Devices

Shreya K. Patel,[1‡] C. Ty Karaba, [1‡] Daniel D. Robertson,[1] Jeffrey Chang,[2] Kevin Fitzell,[2] Charlene Z. Salamat,[1] Jane P. Chang,[2,3,4] Sarah H. Tolbert[1,3,4,*]

ABSTRACT. In this work, multiferroic thin film nanocomposites were synthesized by coating the inside of mesoporous, cobalt ferrite ($CoFe_2O_4$, or CFO) with varying thicknesses of piezoelectric bismuth ferrite (BiFeO3, or BFO) grown by atomic layer deposition (ALD). Since ALD allows for precise control of the BFO layer thickness, the amount of residual porosity inside the pores can be controlled. Upon electrical poling, the piezoelectric BFO strains to be under out-of-plane tension, and since BFO is covalently bound to CFO, this tensile stress is transferred from BFO to CFO. CFO is a negative magnetostrictive material, meaning its magnetization should decrease in the direction of tension. This decrease in magnetization was observed in out-of-plane magnetometry experiments. Interestingly, the magnetization changes were found to be largest in the samples with the most residual porosity, despite the fact that they contained the smallest volume of BFO. Indeed, while the fully-filled samples had a similar magnetoelectric coefficient to other dense nanostructured BFO-CFO composites reported in the literature, composites with the most residual porosity showed an exceptionally large converse magnetoelectric coefficient of 1.2 $\times 10^{-6}$ s·m^{-1}, an order of magnitude higher than dense composites. Strain transfer was confirmed using high-resolution X-ray diffraction. Samples with more residual porosity showed larger strain changes, corroborating the magnetization data. This suggests that magnetoelectric coupling can be optimized by engineering residual porosity into multiferroic composites. Such systems have

profound effects for a broad range of switchable magnetic devices, particularly in the microwave and spintronic space.

1. INTRODUCTION. Conventional electromagnets use *current* to control magnetism, but for the development of nanoscale devices, it is crucial to be able to control magnetization with *voltage* to mitigate Ohmic losses.[47] Multiferroics, materials that exhibit multiple forms of ferroic ordering (including ferroelectricity, ferromagnetism, and ferroelasticity), can enable voltage-control of magnetism for such devices.[1,4] Because there are only a few known room temperature multiferroic materials, strain-mediated multiferroic composites have been developed to address the demand for voltage control of magnetism.[5,6] Such composites couple a piezoelectric material, which strains in response to an electric field, to a magnetostrictive magnetic material, which changes magnetization as its magnetic domains rotate in response to strain. In the composite, when the piezoelectric is electrically poled, the magnetostrictive material will also be strained, which changes its magnetization. The field of strain-mediated magnetoelectric composites has flourished in the past few decades, with a wide range of bulk[48] and thin film[49–53] systems showing large magnetization changes. Indeed, these materials have already been successfully integrated into real devices, especially in the microwave space.[27,54,55] For example, the size of traditional antenna devices is dictated by its signal wavelength, which makes downsizing very difficult. However, multiferroic antenna devices offer a unique design solution allowing conventional antenna devices to be downsized by orders of magnitude.[56–58] These devices utilize strain mediated composites to read/transmit signals. Out-of-plane strain in the magnetostrictive material creates an acoustic wave in response to the incoming electromagnetic wave. This magnetostrictive material is coupled to a piezoelectric, which can convert the acoustic wave into a voltage that is usable as an electric signal.

Thus, the multiferroic antenna is able to convert an electromagnetic signal into a readable voltage, without the same size constraints as traditional antenna devices.

While this class of composite materials has already had a large impact in the field, the efficacy of strain-mediated multiferroics can be greatly enhanced with nanoscale architecture. Increased interfacial surface area between the magnetostrictive material and the piezoelectric materials can result in greater magnetoelectric coupling. Additionally, nanostructured architecture offers an additional advantage over bulk or bilayer films, since they can reduce the effect of substrate clamping, or the prevention of in-plane strain due to covalent binding of a thin film to the substrate. Thus, many nanoscale architectures have been employed in magnetoelectric multiferroic coupling, such as in co-deposited systems with spontaneous phase separation[21,59,60], multilayer thin films[61–63], solution-based systems of nanoparticles in a matrix[64–66], polymer assisted deposition[67,68], and core-shell nanoparticle systems[23,69,70].

Although previous work has shown many methods of maximizing the magnetostrictive-piezoelectric interface, the strain in dense nanostructured materials is still limited by clamping at the interfaces.[59,71] In other words, if there is no room for the materials to flex within the composite, that limits the maximum strain that can be achieved. In this work, we employ a unique strategy in strain-mediated multiferroic systems – engineering *residual porosity* into the composites. This poses a unique advantage over, say, epitaxial multiferroic composites. In epitaxial composites, there is maximum contact between the ferroelectric and the magnetostrictive materials. This results in very high strain transfer between the two materials and has thus resulted in a wide range of systems that exhibit large magnetoelectric coupling.[17,72–75] However, one of the primary limitations in epitaxial films is that they suffer from substrate clamping – the thin composite film is still bound by the lattice constant of the substrate that the films are grown on. Porosity helps alleviate substrate

clamping because porous structures are more mechanically flexible than their dense counterparts, which will make them easier to strain in magnetoelectric composites.[76–78] This theory was reinforced by previously performed finite element modeling on similar multiferroic composites with residual porosity.[79] We found that there are two competing effects in the overall strain response from the porous composite – strain from the mass fraction of piezoelectric in the composite, and the increase in mechanical flexibility in the composite from the porosity. It was found that, in piezoelectric layers of the same thickness as those used in this work, that the increase in strain from increased mechanical flexibility outweighed the effect from larger mass fractions of the piezoelectric. Thus, the porosity makes the composite more mechanically flexible than epitaxial films, which makes them easier to strain.

Recently, we were able to demonstrate that residual porosity could be engineered into multiferroic composites.[16,79,80] We developed the nanocomposite architecture by filling a mesoporous, magnetostrictive template with a piezoelectric material. Here, we specifically chose cobalt ferrite ($CoFe_2O_4$, or CFO) as our magnetic material for its large magnetostriction value.[81] To make porous CFO, block copolymer templating of a sol gel synthesis with Co and Fe precursors was used.[28] In sol gel chemistry, metal precursors are dissolved in a 'sol', and then undergo condensation reactions to form a metal-oxide polymer matrix known as a gel. Amphiphilic block copolymers are added to the sol, which self-assemble into micelles. The gel can then be solution processed to make thin films on a variety of substrates. Here, the templated gel was spin-coated onto platinized silicon substrates (Pt (100 nm)/Ti (5 nm)/SiO_2 ($\sim$ 1 μm)/Si). Upon annealing, the CFO is crystallized into polycrystalline thin films and the polymer micelles are pyrolyzed, leaving pores behind in the structure. This technique is robust and has been used to make a wide range of porous metal oxide materials.[30,82,83]

With the CFO framework in place, we then use atomic layer deposition (ALD) to coat the inside of the pores. ALD is a deposition method where metal precursors are volatilized and then react with available surface sites. Since ALD is a gas phase deposition, precursors can easily pass through the pores and bind to the surface sites inside the CFO framework. ALD is also known as a conformal technique, meaning that it is highly capable of homogeneously coating extremely high aspect ratio structures; this should allow for uniform deposition of BFO throughout our porous CFO structures. Importantly, because the number of surface sites are finite, the reaction is self-limiting. Therefore, ALD provides precise control of film thickness and stoichiometry, on the near-angstrom level. The residual porosity can thus be carefully controlled through the ALD layer thickness. Once deposited, the amorphous ALD films were crystallized using rapid thermal annealing (RTA) under oxygen for 1 minute at 700 °C.

In our previous work, we were able to synthesize CFO using block copolymer templating, as described above, that was fill with ALD-grown lead zirconate titanate ($PbZr0_{0.48}Ti_{0.52}O_3$, or PZT).[16,38] Here, we hypothesized that upon out-of-plane electrical poling, that the PZT would strain to be under out-of-plane tension and in-plane compression. Since the CFO is covalently bound to PZT, and thus is strain-coupled to it, we expected it to also be under out-of-plane tension and in-plane compression. Since CFO is a negative magnetostrictive material, its magnetization should decrease in the direction of tension. Thus, in these composites, we were able to measure the out-of-plane tensile strain change with high-resolution X-ray diffraction and observe the corresponding decrease in magnetization with magnetometry experiments in poled samples. The PZT layer thickness was varied, leaving composites with a range of residual porosity. That was the first system where we found that increasing residual porosity in these samples could lead to larger changes in magnetization. Magnetization changes correlated well to the strain changes, as

probed by high-resolution X-ray diffraction, with samples that showed larger residual porosity also showing increased strain change upon application of an external electric field.[79,80] Additionally, finite element modeling performed on this system confirms that the driving reason for increased strain is because the porous composite is less stiff, which effectively competes with the loss of piezoelectric mass fraction. The non-monotonic strain response was modeled to account for these two competing effects and was found to match the experimental strain values obtained from high-resolution diffraction in the CFO-PZT composites. While the dependence on porosity was clear from that work, the absolute magnetization change was fairly small, since the piezoelectricity in PZT is very sensitive to thickness.

In this work, we build upon those previous results and show both that this phenomenon can be generalized to multiple piezoelectric materials and that the performance can be optimized by selecting materials with ideal properties. As described above, magnetization and strain changes in the CFO/PZT composites were the largest in the thinnest PZT coated samples. However, the piezoelectricity of PZT becomes unstable below a certain thickness, greatly reducing its d_{33}, or piezoelectric coefficient (longitudinal strain change for a given electric field).[84–86] Bismuth ferrite ($BiFeO_3$, or BFO), however, maintains higher d_{33} values than PZT in the ultrathin (< 5 nm) regime.[38,87,88] Thus, while PZT has a higher d_{33} than BFO in the bulk, BFO is expected to have a higher d_{33} in ultrathin films, meaning the magnetization changes are also expected to be larger. In this work, we thus focus on CFO/BFO composites, and show that the trend of increasing multiferroic coupling with increasing porosity is robust across materials systems. We also show dramatically increased performance in this more optimized materials system.

2. EXPERIMENTAL SECTION.

2.1. **Synthesis of CFO-BFO Nanocomposite**. Synthesis of porous CFO[28,80,89] and ALD deposition of BFO[87,88] have been discussed previously. A schematic of the synthesis can be found in Fig. 1(a). For the porous CFO template, a sol gel synthesis containing stoichiometric amounts of Co and Fe precursors (in this work, $Fe(NO_3)_3 \cdot 9H_2O$(0.31 g) and $Co(NO_3)_2$ $6H_2O$ (0.11 g)) were dissolved in 1 mL of 2-methoxyethanol, 1 mL of ethanol, and 20 μL of glacial acetic acid. Once dissolved, the sol was templated with poly((butadiene)(5500)-*block*-poly-(ethylene oxide)(7500)) (Polymer Source Inc, catalog number P2952_BdEO). In this work, a templating solution containing 40 mg of the block copolymer was added to 1 mL of ethanol, then was stirred, and heated on a 50 °C hot plate to dissolve the polymer for approximately an hour. Once homogenous, the templating solution was added to the sol.

Films were then dip-coated from this solution onto silicon with a platinum back electrode (Ti(5 nm)/Pt (100) deposited on thermally oxidized silicon) under 10-20% humidity. Films were calcined in air at 80 °C for 6 hours, at 130 °C for 8 hours, and at 180 °C for 6 hours. Once calcined, films were crystallized through annealing overnight at 550 °C with a 10 °C/min ramp and cool.

For ALD BFO, metal alkoxide precursors β-diketonate, tris(2,2,6,6-tetramethyl-3,5-heptanedionato) iron(III) ($Fe(TMHD)_3$), and $Bi(TMHD)_3$ were co-reacted and oxidized with radicals, forming amorphous films. It should be noted that further heating beyond the temperature required for crystallization (550 °C) can warp the pore network, so we limited the crystallization time to 1 minute using an RTA process to maintain the ordered pore structure. Therefore, once deposited, ALD BFO was crystallized through rapid thermal annealing at 700 °C under oxygen for 1 minute in a tube furnace.

2.2. **Instrumentation**. Ellipsometric porosimetry (EP) was performed using a Semilab PS-1100 in the spectral range of 1.0 eV to 5.0 eV. Toluene was used as the adsorbent and the EP analysis

was performed using SEA software. Imaging and energy-dispersive X-ray spectroscopy on the nanocomposites was confirmed using a JEOL JSM-6700F field-emission scanning electron microscopy (FE-SEM). XPS was performed on a Kratos Axis Ultra DLD spectrometer with a monochromatic Al Kα radiation source. A charge neutralizer filament was used to prevent the charging of the BFO/CFO films. Both spectra were calibrated using the adventitious Carbon 1s peak. Analysis was performed on CASA XPS Software using the CASA XPS Library. S/TEM imaging was performed using a FEI Titan scanning transmission electron microscope operated at an accelerating voltage of 300 kV. This instrument is equipped with Oxford X-MaxTEM 100 N TLE Windowless silicon drift detector (SDD) 100 mm 2 EDS and a Gatan Ultrascan 2 K × 2 K charge-coupled device (CCD) camera. To prepare samples, films were detached from the substrate with a razor blade, suspended in ethanol, and drop-cast onto copper grids for analysis. Grazing incidence wide angle scattering (GIWAXS) was collected at Stanford Synchrotron Radiation Laboratory (SSRL) using beamline 11-3. 2D patterns were reduced to 1D patterns using IgorPro 6.37. 1D patterns were then compared to JCPDS reference cards #00-001-1121 (for CFO) and #00-014-0181 (for BFO) using X'Pert Highscore Plus 2.0.1. Magnetic measurements were carried out on a Quantum Design MPMS3 superconducting quantum interference device (SQuID) magnetometer. Polarization – electric field characterization was carried out on a precision RT66C Ferroelectric Tester (Radiant Technologies). For magnetoelectric coupling testing, samples were poled in between two aluminum stubs, with a dielectric spacer (12.7 μm thick) on top to prevent shorting (see Fig. S8). The stubs were wired to an Agilent power supply connected to an amplifier. High angular resolution X-ray diffraction (XRD) was collected at SSRL using beamline 7-2 at wavelengths λ = 0.886 Å.

3. RESULTS AND DISCUSSION.

First, we set out to characterize the unfilled CFO framework. An SEM image showing the morphology of the unfilled CFO template is shown in Fig. 1(b). The porosity is relatively ordered, with pore sizes ranging from 10-13 nm. We then turned to characterize the composite with elemental mapping. Energy-dispersive X-ray spectroscopy (EDS) was used to observe the relative elemental ratio between the cobalt and iron in the composite films, which show the expected 1:2

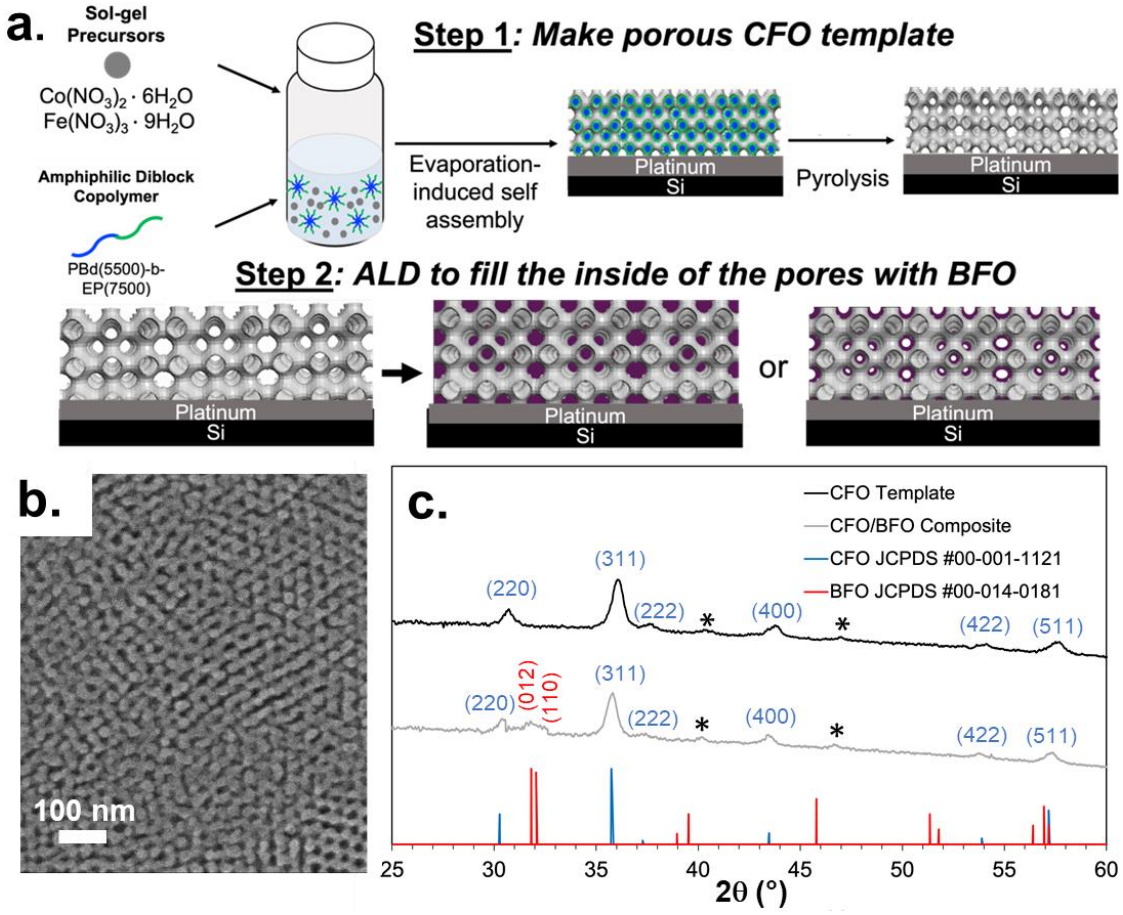

Figure 3-1. Synthesis and characterization of multiferroic nanocomposites. (a) Schematic illustrating the synthesis of multiferroic nanocomposites with residual porosity, (b) SEM image of unfilled, porous CFO template with pores from 10-13 nm, (c) GIWAXS 1D pattems for the porous CFO template alone (black), 12 nm filled BFO nanocomposite (grey). Asterisks represent likely Pt back electrode peaks.

atomic ratio for CFO [Fig. S1(a-b)]. The quantification of cobalt and iron is echoed by STEM-EDS of the 6 nm composite (Fig. S2). We also used grazing incidence wide angle scattering (GIWAXS) to confirm the crystal structure of the CFO template [Fig. 1(c)]. GIWAXS confirms the porous CFO template is crystalline and has the expected Spinel crystal structure in the composite. CFO template films for all the composites was intentionally kept the same film thickness in order to keep the strain from substrate clamping the same. We note that the CFO template itself and the composite films are under some strain from the difference in thermal expansion coefficient. More discussion of the initial macrostrain state of the CFO template (Fig. S3) and the composites (Fig. S4), as well as the microstrain state of the composites (Fig. S5) can be found in the supporting information.

The thickness of the BFO layer in the composites was varied across samples, filling the pores of CFO to approximately 3 nm, 6 nm, 9 nm, 12 nm filled. First, we set out to perform elemental analysis on the resulting composites. In both composites, we see the cobalt and iron L-edges in the appropriate 1:2 atomic ratio expected for CFO. In EDS, we observe a small peak at 2.4 keV that matches the bismuth M edge energy level in both the 3 and 6 nm sample [Fig. S1(a-b)]. The bismuth fraction can be quantified for the 6 nm film [Fig. S1(b)], but the error is too large for the 3 nm sample. The quantification of bismuth, cobalt, and iron is echoed by STEM-EDS of the 6 nm composite (Fig. S2). Since the volume of BFO is so small, we turned to XPS to more clearly observe the BFO layer [Fig. S1(c)]. In the 3 nm sample, we observe the bismuth 4*f*, 5*p*, and 5*d* energy levels [Fig. S1(c)]. We also observe cobalt and iron, as we would expect for CFO. In the 6 nm sample, however, we only see the bismuth and iron from BFO, and no cobalt [Fig. S1(d)]. This result nicely confirms the presence of thicker surface films in the 6 nm sample, as 6 nm should be

greater than the XPS penetration depth and the CFO component of the composite should not be observable in this sample.

Following the synthesis and characterization of the composites, we then set out to characterize their morphology. As can be seen from SEM images of the filled composites, the pore diameters were found to be about 10-13 nm in unfilled CFO [Fig. 1(b)] and then gradually decrease with increased BFO layer thickness [Fig. 2(a)]. The residual porosity was determined using ellipsometric porosimetry with toluene gas vapor as the adsorbent [Fig. 2(b)].[90] The isotherms for each sample show a hysteretic response, indicating that the nanocomposites have an interconnected pore network.[91] As can be seen in the isotherms in Fig. 2(b), as the BFO layer thickness is increased, the sample porosity decreases, down to nearly 0% porosity in the fully-filled nanocomposite. This monotonic trend is what we would expect with the BFO layer thickness from

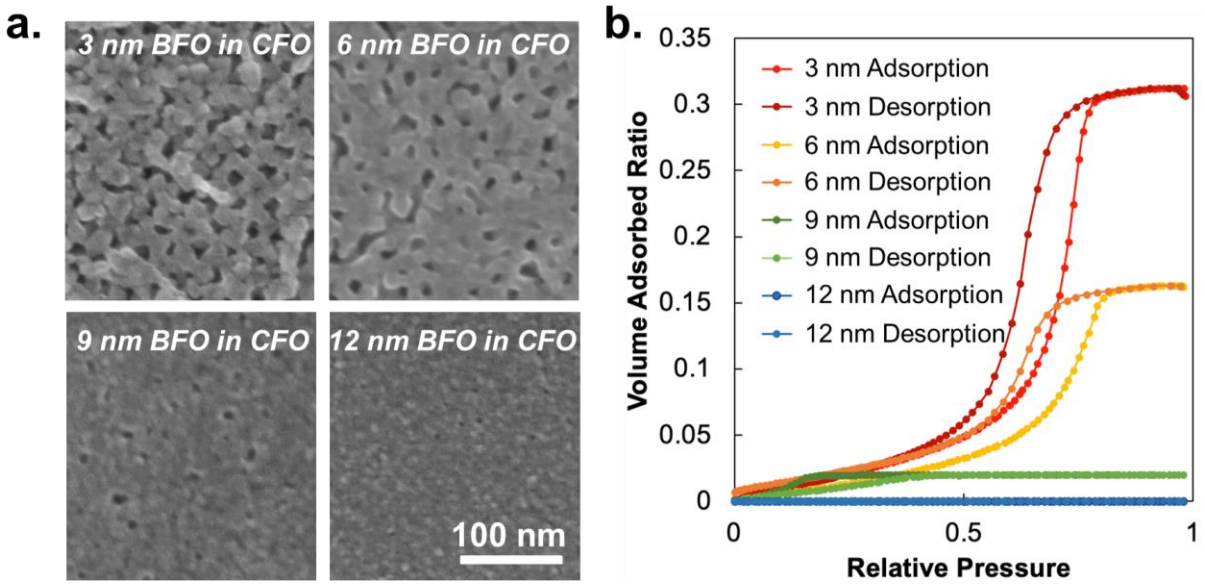

Figure 3-2. Morphology and residual porosity in multiferroic nanocomposites visualized through (a) SEM images and (b) ellipsometric porosimetry isotherms. Residual porosity is greatest in composites with the thinnest ALD layers (25% filled) and decreases with increasing ALD layer thickness.

the ALD deposition. It is important to note here that although the isotherm shows near 0% gas adsorption, it is possible that there is still some residual porosity in these samples. ALD filling can fill the pore necks, 'blocking' toluene from entering the interior of the structure. Nevertheless, it is clear from SEM and ellipsometric porosimetry that the residual porosity is very low with the thickest ALD BFO layers.

In addition to observing the morphology of the composites, we wanted to characterize the CFO/BFO distribution with STEM (Fig. 3). Bright field and High-Angle Annular Dark Field (HAADF) images both show the film with well-defined residual porosity [Fig. 3(a-b)]. We then turned to elemental mapping to see where the BFO and CFO are. Elemental mapping is done in STEM-EDS mode, which has significantly reduced resolution relative to standard STEM imaging [Fig. 3(c)]. Because both phases contain Fe, we can use the relative mapping of cobalt to see where the CFO lies, and the mapping of bismuth to see where the BFO is. As seen from the elemental mapping, the bismuth is found homogeneously distributed throughout the network, demonstrating that BFO does, in fact, infiltrate the inside of the pores to form a uniform coating inside the pore structure [Fig. 3(c-f)]. To see

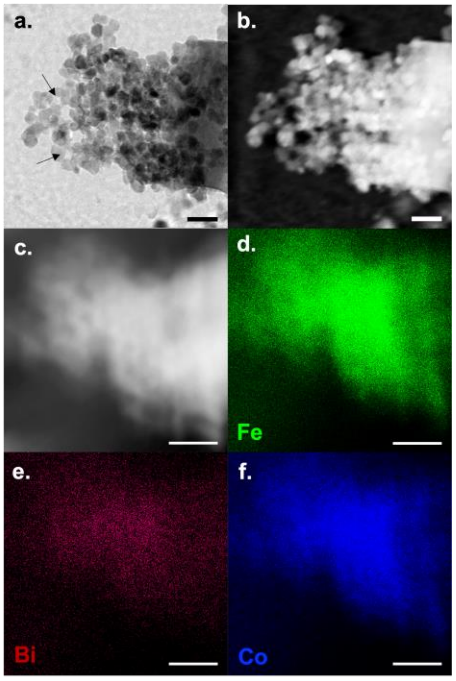

Figure 3-3. Scanning Transmission Electron Microscopy (STEM) of composite film (6 nm). Bright field images (a) and High-angle annular dark field (HAADF) (b) STEM images of the composite, showing well-defined residual porosity (c) STEM-EDS image with elemental mapping of Fe (d), Bi (e), and Co (f). Bi is spread over the entire area of the film. All scale bars are 50 nm.

the spatial variation in Co and Bi, we plotted a quantitative elemental line scan over regions containing clear pores to visualize the BFO/CFO distribution (Fig. S6). Though the resolution is poor due to both the multilevel sample and ferroelectric nature of the sample (making them very susceptible to charging and thus drifting in electron microscopy), there is a distinct anticorrelation between the cobalt and bismuth in the line scan, with a periodicity that approximately matches the distance of one pore (10-13 nm) apart. When a Pearson correlation coefficient is calculated form the data in Fig. S6, the Bi and Co are found to be anticorrelated with a correlation coefficient of -0.4. This data thus strongly supports the picture of a CFO framework coated homogeneously by BFO.

Having characterized the material interfaces with TEM, we turned to observing the magnetic and piezoelectric properties of CFO and PZT, respectively. Since ferrimagnetism and piezoelectricity are ferroic properties, both exhibit hysteresis. First, we used superconducting quantum interference device (SQuID) magnetometry to look at the hysteretic magnetization-magnetic field (MH) loops in unfilled porous cobalt ferrite [Fig. S7(a)]. Unfilled cobalt ferrite thin films exhibit a saturation magnetization of about 340 emu/cc and coercivity of approximately 800 Oe, which is close to the literature values in thin films.[16,24,28,80,92] The piezoelectric properties of the ALD BFO were also investigated using polarization – electric field (PE) curves [Fig. S7(b)]. Since the BFO layers in this work are very thin, analogous thickness, planar films of the same thickness would easily short. We thus looked at the piezoelectric properties of ALD deposited BFO in thicker films of approximately 100 nm thickness. It is important to note that while the coercivity of the thick BFO was found to be approximately 70 kV/cm, that piezoelectric coercivity is dependent on material thickness, and so the coercivity of the thicker ALD film is not

representative of the coercivity of the thin BFO coatings in the nanocomposites studied in this work.[93–97]

With confirmation of the magnetic and piezoelectric hysteretic behaviors of CFO and BFO separately, we set out to study the magnetoelectric coupling in the porous nanocomposites. We electrically poled samples *ex situ* out-of-plane from the sample and collected hysteresis loops with the films both in the plane of the magnetic field and out of the plane of the magnetic field (more details on electrical poling of the porous composites, including a schematic of electrical poling and magnetic measurements, can be found in the supporting information, Fig. S8). In the plane of the applied magnetic field, we saw no change in magnetization (Fig. S9). This observation is in agreement with previous results on porous CFO-PZT nanocomposites, and is likely due to substrate clamping.[16,79,80]

Although the nanocomposites are clamped in-plane because they are covalently bound to the substrate, the films are free to strain out-of-plane, which correlates to the large out-of-plane magnetization changes observed (Fig. 4). Since BFO tenses in the along the direction of the electric field, upon out-of-plane electric poling, BFO is under out-of-plane tension. This strain is expected to be transferred to the CFO, since it is covalently bound to BFO. Therefore, CFO should also be in out-of-plane tension. CFO is a negative magnetostrictive material, meaning that its magnetization will decrease in the direction of tension.[49,81] Another way to think about this is in terms of the magnetic anisotropy in the system. CFO has high magnetocrystalline anisotropy and high magnetostriction. The high magnetocrystalline anisotropy means that at saturation, spins are generally aligned with the easy axis that is closest to the magnetic field direction, but generally do not align fully with the magnetic field in a sample made of randomly oriented grains. The observed magnetization in the out-of-plane direction is the out-of-plane component of the magnetization for

each domain. When the sample is electrically poled out-of-plane, the magnetostriction term adds to the magnetocrystalline anisotropy. Because the magnetostriction is negative, the strain term will favor in-plane spin alignment, and it will pull the easy axes away from the out-of-plane direction. Thus, after electric poling, at magnetic saturation in the out-of-plane direction, spins will still lie in the easy direction closest to out-of-plane. This means that the out-of-plane component of the magnetization will be reduced, and thus the saturation magnetization will be reduced. Thus, as the

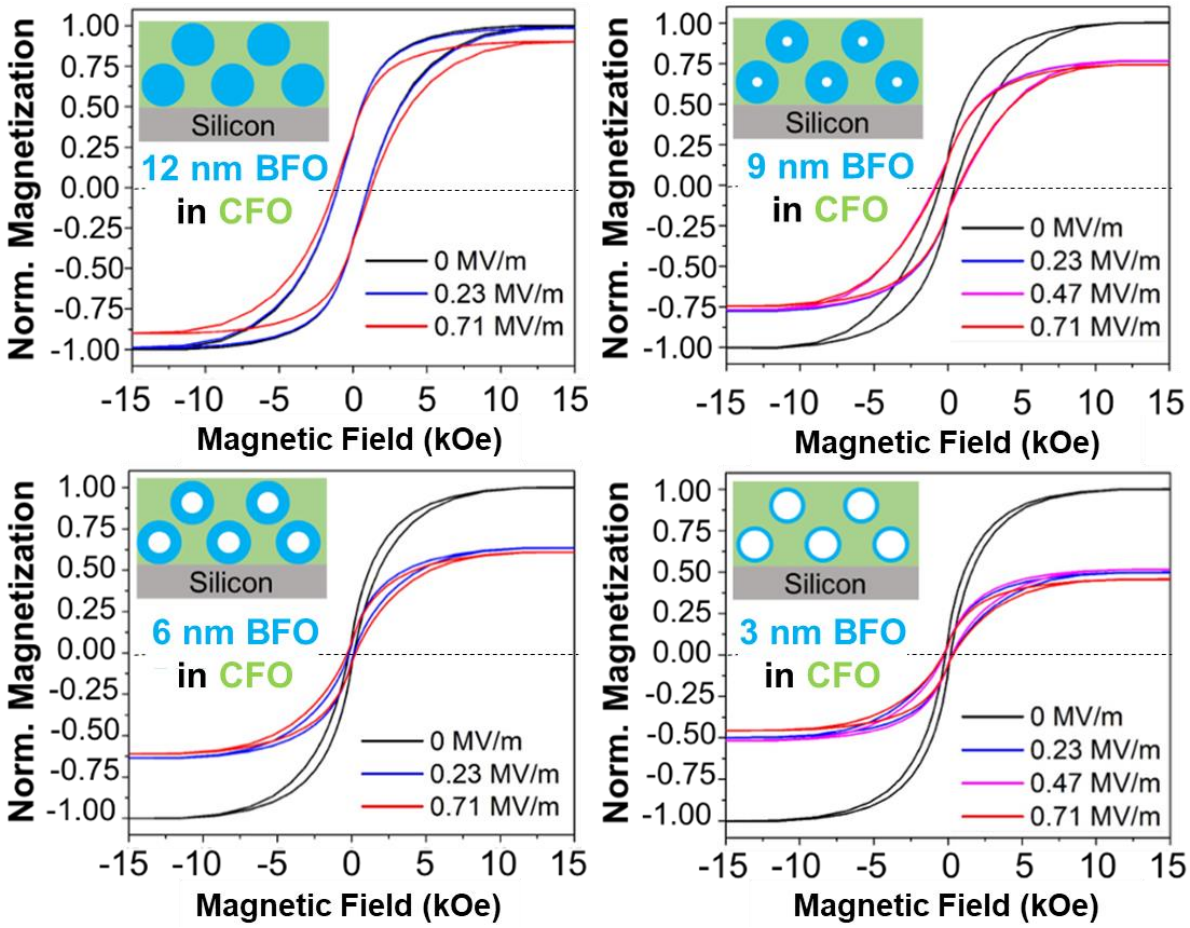

Figure 3-4. Residual porosity dependence in MH loops collected out of the plane of the magnetic field. As the BFO layers get thinner (and the residual porosity gets larger), the saturation magnetization changes get larger, reaching a large 60% decrease in magnetization in the composite with 3 nm of BFO.

multiferroic samples are electrically poled, their magnetization is expected to decrease in the out-of-plane direction, which is exactly what we observe in the samples studied in this work (Fig. 4).

In contrast to using strain to change magnetism, it has been shown that the saturation magnetization of CFO can change due to magneto-ionic effects.[98,99] This can either be due to redox at the magnetic ion (for example, Fe^{3+} has a magnetization of 5 μ_B, while Fe^{2+} has a magnetization of 4 μ_B) or due to the migration of O^{2-} anions.[100,101] As a control experiment, we poled bare, unfilled CFO at the same electric fields used in this work (Fig. S10). We observed no significant changes in the magnetization, ruling out ionic contributions to the magnetization change.

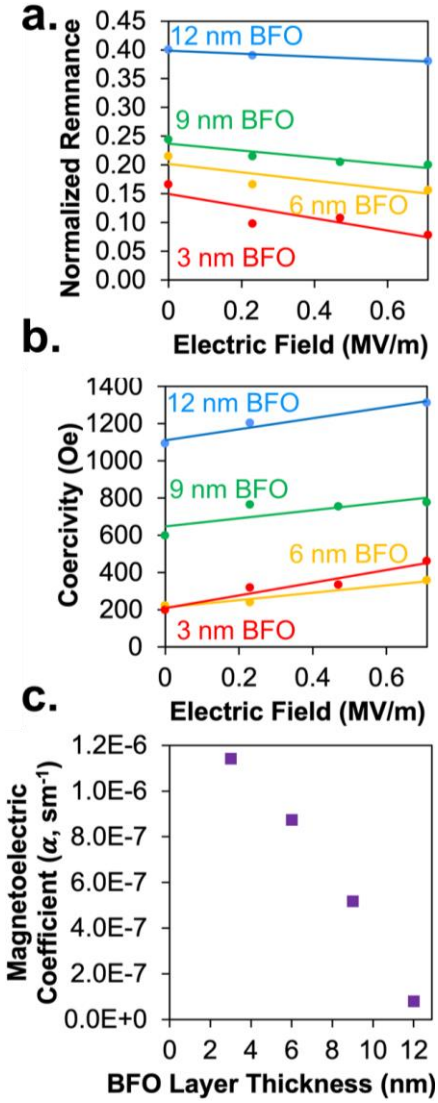

Figure 3-5. Out-of-plane trends in (a) coercivity, (b) remnant magnetization, and (c) ME coefficient as a function of BFO layer thickness.

We calculated the magnetoelectric coupling in a range of samples with varying BFO layer thicknesses (3 nm, 6 nm, 9 nm, 12 nm) and thus, residual porosities (Fig. 5). Interestingly, the residual porosity of the sample was found to play a major role in the electric field induced changes. The fully-filled samples (12 nm thick BFO) were found to have around a 10% decrease in magnetization after poling to the highest fields used in this work, but as the amount of residual porosity increased, the magnetization change increased up to a 60% drop in magnetization in the samples with 3 nm BFO.

In addition to the large change in saturation magnetization, modest changes in coercivity and remnant magnetization were found upon electrical poling [Fig. 5(a-b)]. We had hypothesized that upon out-of-plane electrical poling, that the BFO would strain so that it is under out-of-plane tension and in-plane compression, and since CFO is strain-coupled to BFO, that the CFO would also be under out-of-plane tension and in-plane compression. Since CFO is a negative magnetostrictive material, its easy axis should rotate to align more with the direction of compression. If this is true, then it should result in the out-of-plane coercivity getting larger, and the in-plane coercivity getting smaller. As mentioned previously, since the composite is substrate-clamped in-plane, we do not see significant changes in in-plane coercivity or saturation magnetization. However, we do see the coercivity getting larger in the out-of-plane direction, as expected [Fig. 5(a)]. Since the hard axis should rotate toward the out-of-plane direction upon electrical poling, we also expect the MH loop to be less square in the out-of-plane direction, which is observed in the plots of remnant magnetization [Fig. 5(b)].

We can use the change in saturation magnetization to calculate the converse magnetoelectric coefficient, defined as $\alpha = \mu_0 \mathrm{d}M/\mathrm{d}E$, where α is the magnetoelectric coefficient, μ_0 is the permeability of free space, $\mathrm{d}M$ is the change in saturation magnetization between the unpoled and poled states, and $\mathrm{d}E$ is the applied electric field used to get the largest magnetization change [Fig. 5(c)]. The magnetoelectric coefficients were calculated from the lowest electric field at which samples exhibited a saturated magnetization change (0.23 MV/m in all samples except the fully-filled sample, which required a higher field of 0.71 MV/m to saturate). The magnetoelectric coefficient of the fully-filled sample seemed to be on par with other reported BFO-CFO nanocomposites, which tend to be on the order of 10^{-7} s·m^{-1}.[102–104] However, for the sample with the most residual porosity, we calculate a large, out-of-plane magnetoelectric coefficient of 1.14

$\times 10^{-6}$ s·m^{-1}, an order of magnitude larger than dense multiferroic nanocomposites (both previously reported in the literature[79,80,89,102–104] and seen in the fully-filled sample described in this work). The magnetoelectric coefficients described here are likely an underestimate, since samples were poled *ex situ*, and so the saturation magnetization changes were observed at the remnant (not saturation) polarization state of the piezoelectric. Thus, the actual magnetoelectric coefficient is expected to be even larger with *in situ* electrical poling, where BFO is at its saturation strain state. We note that, since we observe minimal magnetization changes in-plane due to substrate clamping, the in-plane magnetoelectric coefficients is near zero (Fig. S11). This anisotropy, with a large out-of-plane and small in-plane magnetoelectric coefficient, could be very useful in spintronic and microwave devices.[47,105]

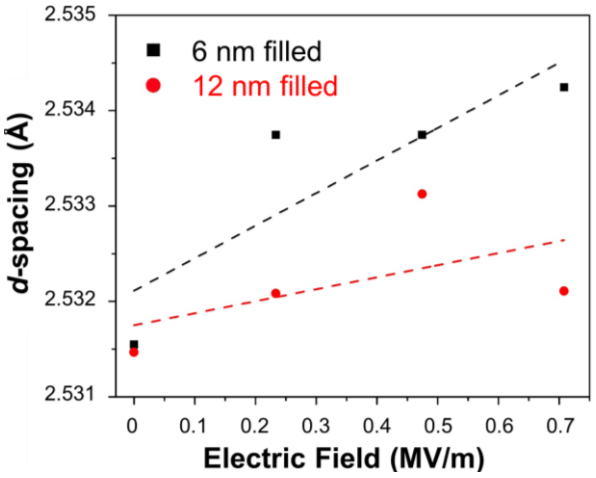

Figure 3-6. High angular resolution X-ray diffraction collected out of plane from the sample, showing *d*-spacing for the CFO (311) as a function of electric field, showing nanocomposites are in out-of-plane tension.

We used high-resolution diffraction to corroborate that these large magnetoelectric changes indeed stem from strain changes. Changes in crystal structure, such as those measured by X-ray diffraction, can be mapped onto the macroscopic strains in the material. Samples were again poled *ex situ* in the out-of-plane direction at increasing electric fields, and the *d*-spacing was measured at each electric field (Fig. 6). If the magnetization change described above is truly induced by a strain-mediated mechanism, we expect that upon out-of-plane electrical poling, BFO should be in out-of-plane tension and in-plane compression. Since CFO is covalently bound to BFO, we also expect CFO to

also be in increased out-of-plane tension. Given the thinness of the BFO ALD layer, it was difficult to resolve changes in *d*-spacing in any of the BFO peaks, so strain changes in the piezoelectric could not be directly measured. However, since CFO is covalently bound to BFO, and thus strain-coupled, we can use the far more intense CFO(311) peaks to track strain changes in the composite. Thus, the measured lattice spacing changes in CFO was used to calculate a proxy (d'_{33}) for the d_{33}, or the longitudinal strain change expected for BFO as a function of the effective applied voltage. The calculated d'_{33} was found to be 2×10^{-9} m/V, which is just under the reported literature values for BFO of the same thicknesses.[87,106] It should be noted that this d'_{33} value is expected to be lower than actuality for two reasons. First, it was calculated assuming 100% strain transfer from the BFO to the CFO, which is not likely to be the case. Second, the value calculated in this work made use of samples that were poled *ex situ,* and thus have relaxed to their remnant polarization, rather than the saturation polarization. Nevertheless, the approximated d'_{33} from high-resolution diffraction demonstrates that strain transfer between the BFO and CFO is likely the origin of the magnetic changes observed here.

Importantly, the out-of-plane *d*-spacing for the sample with more residual porosity (6 nm filled, black in Fig. 6) was found to increase more than in the fully-filled sample (12 nm filled, red in Fig. 6). The d'_{33} was found to be 2×10^{-9} m/V in the 6 nm sample, whereas the d'_{33} in the 12 nm sample was found to be only 7×10^{-10} m/V. This large difference in d'_{33} is thought to be the result of the increased mechanical flexibility in the more porous nanocomposite, making the overall material easier for the material to strain.".[43]

4. CONCLUSIONS.

Overall, porous nanocomposites with residual porosity can have extremely large magnetization changes in comparison to their dense counterparts. This was realized in multiferroic

nanocomposites with tunable residual porosity formed by ALD filling into a mesoporous framework. The crystal structure of the piezoelectric and magnetostrictive phases of BFO and CFO were confirmed with GIWAXS, and their piezoelectricity and ferrimagnetism was confirmed with PE and MH loops, respectively. Since the resulting composite is more mechanically flexible and alleviates substrate clamping by providing room for CFO and BFO to flex, the magnetization changes are much larger than in dense composites. SQuID magnetometry measurements show large electric-field induced magnetization changes from a 12% change in magnetization in the fully-filled samples to an almost 60% change in the samples with the most residual porosity. The residual porosity was further found to increase the magnetoelectric coupling by more than an order of magnitude, with the converse magnetoelectric coupling coefficient found to be 8.1×10^{-8} s·m^{-1} in the fully-filled samples, increasing to 1.2×10^{-6} s·m^{-1} in the samples with the most residual porosity. Systems that can drive large magnetic changes, like the ones in this work, could have enormous potential for switchable magnetic systems, such as in the microwave and spintronic space.

ACKNOWLEDGMENT

The authors would like to acknowledge Bálint Fodor, Peter Basa, and John Byrnes for their assistance with ellipsometric porosimetry measurements. The authors would also like to acknowledge Adrian Acosta for helpful discussions. This work was supported by the NSF NanoSystems Engineering Research Center for Translational Applications of Nanoscale Multiferroic Systems (TANMS) under Cooperative Agreement Award EEC-1160504. Additionally, authors S.K.P and D.D.R. acknowledge support from the National Science Foundation Graduate Research Fellowship under Grant No. DGE-1650604 and DGE-2034835.

This work made use of the UCLA Molecular Instrumentation Center (MIC). This manuscript contains data collected at the Stanford Synchrotron Radiation Lightsource (SSRL), experimental stations 11-3 and 7-2. SSRL and the SLAC National Accelerator Laboratory are supported by the U.S. Department of Energy, Office of Science, Office of Basic Energy Sciences under Contract No. DE-AC02-76SF00515.

CHAPTER 4.

In-situ Measurement of Magnetoelectric Coupling and Strain Transfer in Multiferroic Nanocomposites of $CoFe_2O_4$ and $Hf_{0.5}Zr_{0.5}O_2$ with Residual Porosity

Chapter 4 describes *in-situ* magnetometry and diffraction experiments on porous multiferroic composites of cobalt ferrite and hafnium zirconium oxide, which allows the full saturation magnetoelectric coupling to be observed in such composites.

This chapter was reprinted with permission from **Patel, S.K.**; Robertson, D.D.; Cheema, S.S.; Salahuddin; S., Tolbert, S.H. "*In situ* measurement of magnetoelectric coupling in multiferroic nanocomposites with residual porosity" *accepted, Nano Letters.* Copyright 2023, American Chemical Society.

A reprint of the supporting information is given in Appendix B.

In-situ Measurement of Magnetoelectric Coupling and Strain Transfer in Multiferroic Nanocomposites of $CoFe_2O_4$ and $Hf_{0.5}Zr_{0.5}O_2$ with Residual Porosity

Shreya K. Patel,[1] Daniel D. Robertson,[1] Suraj S. Cheema,[2] Sayeef Salahuddin,[2,3] Sarah H. Tolbert[1,4,5,*]

ABSTRACT. With increasing applications for voltage-controlled magnetism, the need to more fully understand magnetoelectric coupling and strain transfer in nanostructured multiferroic composites has also increased. Here, multiferroic nanocomposites were synthesized using block-copolymer templating to create mesoporous cobalt ferrite (CFO), followed by partly filling the pores with ferroelectric zirconium-substituted hafnia (HZO) using atomic layer deposition (ALD) to produce a porous multiferroic composite with enhanced mechanical flexibility. Upon electrical poling of the nanocomposite, we observed large changes in the magnetization. These changes partly relaxed upon removing the electric field, suggesting a strain-mediated mechanism. Both the anisotropic strain transfer from HZO to CFO and the strain relaxation after the field was removed were confirmed using high-resolution X-ray diffraction measurements collected during *in-situ* poling. The *in-situ* observation of both anisotropic strain transfer and large magnetization changes allow us to directly characterize the strong multiferroic coupling that can occur in flexible, nanostructured composites.

Conventional electromagnetic devices, such as memory and antenna devices, use current to control magnetism, but suffer from Ohmic losses that reduce their efficiency.[47] Voltage control of magnetism has thus become desirable to mitigate such losses, allowing electromagnetic device components to be made much smaller and more efficient. Multiferroic materials, which exhibit multiple forms of ferroic coupling (such as ferromagnetism, ferroelectricity, and ferroelasticity)

have arisen as a promising solution.[1,4] In particular, strain-mediated magnetoelectric composites utilize a popular coupling mechanism, since they allow for fast and reversible control of magnetism.[2,107–109] These strain-mediated composites couple a ferroelectric material, which strains in response to an applied voltage, to a magnetostrictive material, which changes magnetic domain orientation in response to the strain from the ferroelectric. This coupling thus allows magnetization to be controlled with a voltage. These composite materials have been incredibly successful, and have been integrated in a wide range of devices in both the memory and microwave spaces.[54–56,81,104,110] In such composites, the amount of strain-mediated multiferroic coupling is limited by the interfacial surface area between the magnetostrictive and ferroelectric materials. Accordingly, nanostructured multiferroic composites can achieve greatly enhanced magnetoelectric coupling.[6,7] Thus, a wide variety of architectures have been designed, including multilayer thin films[61,63,75,111], co-sputtered phase-separated systems[17,21,59,60], nanoparticles in a matrix[64–66], and core-shell nanoparticles[13,23,70].

Recently, we found that the magnetoelectric coupling coefficient could be dramatically increased in nanoporous multiferroic composite thin films with residual porosity.[16,79,80] These composites were fabricated coating the inside of a nanoporous magnetic material with atomic layer deposition (ALD). Importantly, the thickness of the ferroelectric coating deposited during ALD can be tuned to leave residual porosity that allows the network to flex. In these composites, cobalt ferrite ($CoFe_2O_4$, or CFO) was chosen as the magnetic material, as it has a very high magnetostriction coefficient of 200-300 ppm.[112,113] Nanoporous CFO can be readily fabricated using block co-polymer templating of sol-gel precursors.[28] Once the magnetostrictive nanoporous CFO films had been synthesized, ALD was used to deposit the ferroelectric. In ALD, reactive metal precursors are volatilized and allowed to react with all available surface sites inside the pore

structure.[114–116] Since the number of surface sites is finite, the reaction is self-limiting. Once the reaction is complete, the surface is reactivated with an oxidant, followed by another metal precursor cycle. Each ALD cycle deposits less than a monolayer, allowing for precise control of the thickness of the ALD layer through the number of cycles. Thus, the ALD layer thickness can be tuned to allow for residual porosity in the composites. After deposition, the filled composites can be annealed at high temperature to crystallize the as-deposited film.

In previous work, we first grew lead zirconate titanate ($PbZr0_{0.48}Ti_{0.52}O_3$, or PZT) onto a porous CFO template with varying thicknesses of PZT, and thus, varying amounts of residual porosity.[16] Interestingly, upon *ex situ* poling of these composites, we found that the samples with the most residual porosity had the highest magnetoelectric response, despite having the least ferroelectric material in the composite. Using *ex situ* poling and residual polarization, we were able to correlate the magnetic changes to strain changes measured using high-resolution diffraction, and found that the strain changes were indeed highest in samples with the most residual porosity.[80] The strain data suggest that the residual porosity allows for flexibility in the composite, and thus allow for larger strain and strain transfer to the magnetic material. This phenomenon was also generalized to another ferroelectric material, bismuth ferrite ($BiFeO_3$, or BFO), which showed an exceptionally large magnetoelectric coupling constant of 1.2×10^{-6} s·m^{-1}, an order of magnitude higher than that reported in most dense, nanostructured multiferroic composites made of the same materials.[117]

To better understand the effect of porosity, we turned to finite element modeling to simulate the deformation response in these composites.[79] We found that the effect of increasing mechanical flexibility outcompetes the effect of having a larger mass fraction of ferroelectric material in the composite, so that thinner ferroelectric layers are indeed expected to produce a larger response. Modeling also indicated that effective strain transfer only occurs in the vertical struts of the porous

network, where elongation of the ferroelectric unit cell can locally stretch the CFO. We note that in the experiments described below, X-ray diffraction is used to measure strain transfer, but only an average value of the local strain is measured.

While our previous work demonstrated that residual porosity has profound implications for multiferroic composites, the primary challenge in these composites is that the best ferroelectric behavior was observed in materials with only a few nanometers-thick ferroelectric layers, and most ferroelectrics show very poor behavior in this extremely thin film form. As a result, here, we investigate composites made from porous CFO with ALD-grown zirconium-substituted hafnia ($Hf_{0.5}Zr_{0.5}O_2$, or HZO). In its polar orthorhombic phase ($Pca2_1$), HZO is a unique ferroelectric that has recently garnered significant attention due to its potential as a fully CMOS-compatible material for transistor applications.[118–120] Hafnia-based ferroelectrics like HZO have also begun to be integrated into a range of dense, strain-mediated magnetoelectric composites.[121–126] The mechanism of ferroelectricity in HZO is different than most ferroelectrics, such as PZT and BFO, in that instead of the electric dipole arising from the displacement of a non-centrosymmetric anion, its polarity arises from the displacement of the oxygen in its crystal structure.[127,128] Importantly, the displacement of a non-centrosymmetric ion becomes increasingly less stable with decreasing film thickness, and so the ferroelectricity in conventional ferroelectrics, such as PZT and BFO, is reduced in ultrathin films (< 5 nm).[84,85,106,129] Hafnia-based ferroelectrics like HZO, however, are stabilized in their polar crystal structure (corresponding to the ferroelectric phase) due to surface energy effects. Thus, HZO presents a promising ferroelectric in thinner film format.[130–132] Since our previous work found that more residual porosity (and thus, thinner ferroelectric layers) resulted in the largest magnetoelectric coupling, here, we utilize HZO since its ferroelectricity is stabilized in the ultrathin regime.

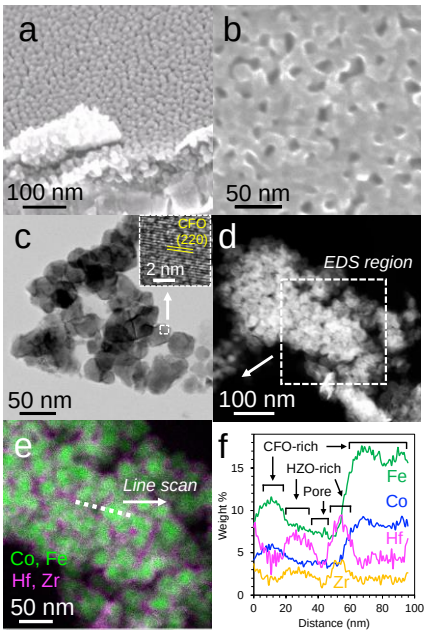

Figure 4-1. Morphology visualized through SEM (**a** + **b**), high-resolution TEM (**c**), and STEM-EDS (**d**, **e**, **f**). **a**) Image taken at 45° along a scratched film edge, showing the internal pore structure of unfilled CFO. **b**) Morphology of the composite after HZO deposition. **c)** Low magnification image showing porosity. Inset: High magnification image showing the crystalline CFO lattice. **d)** High-angle annular dark-field STEM image of the composite. **e)** STEM-EDS mapping showing a uniform coating of HZO throughout the porous composite. **f)** A quantitative STEM-EDS line scan across the pore highlighted in e) demonstrating clear regions of HZO at the pore interfaces.

In addition to choosing a ferroelectric optimized for ultra-thin film composites, in this work, we also set out to carry out a more mechanistic study of the *in-situ* poled magnetic and strain response of the CFO-HZO nanocomposites. While multiferroics have undergone a renaissance in the past few decades, there is still much to learn about the mechanism behind magnetoelectric coupling in these systems. Thus, in strain-mediated composites, it is important to observe both magnetoelectric and strain coupling as a function of applied bias. With this in mind, here, we utilize *in-situ* electrical poling, rather than *ex situ*, in order to observe the saturation magnetoelectric and strain coupling. *Ex situ* poling only samples the remnant strain state, which is usually much less that that saturated state due to relaxation. Thus, *in-situ*

poling allows for the investigation of the fully strained composites and more directly probes the magnetoelectric coupling.

The composites were synthesized in two steps; first, the porous CFO composite was synthesized, then the ALD HZO layer was deposited. The specific experimental details can be found in the supplemental information. Briefly, nanoporous CFO films were made with a polymer-templated sol-gel process, in which cobalt and iron precursors were dissolved and mixed with a micelle-forming block co-polymer template.[28] The resulting solution was dip-coated onto a substrate. Upon annealing the resulting films, the polymer template was removed by pyrolysis, and inorganic precursors crystallized into a spinel structure, leaving pores in a crystalline CFO matrix. With the porous CFO template in hand, we then turn to ALD for the HZO deposition using a previously reported procedure.[131] As mentioned previously, we found in both the CFO-PZT and CFO-BFO composites that more residual porosity, and thus thinner ferroelectric layers, resulted in the largest magnetization and strain changes.[16,80] Therefore, in this work, we specifically investigated 3 nm thick ALD HZO films, since this thickness has shown to exhibit relatively good ferroelectricity in dense films on silicon, and because we have observed the best coupling at this thickness in previously reported composites with residual porosity.

We investigated the morphology of the resulting composite using both scanning and scanning/transmission electron microscopy (SEM and S/TEM). Figure 1a shows the pore structure of an unfilled CFO thin film. The CFO has an interconnected pore network, which allows the volatilized ALD precursors to uniformly coat the inside of the porous architecture. We also examined the films' morphology in the composite structure after the ALD deposition (figures 1b, 1C, and 1D). We found that the structure was maintained after the HZO deposition. Since the HZO is difficult to resolve with imaging, we characterized the composite using STEM with energy

dispersive spectroscopy elemental mapping (STEM-EDS). Figure 1e shows STEM-EDS of the porous composite highlighting the CFO and HZO components in green and pink, respectively. The HZO uniformly coats the CFO network throughout the film. The composite structure was further confirmed using a quantitative EDS line scan across a selected pore, which showed clear regions of HZO-rich material at the interfaces with the pore (figure 1f).

In addition to observing the morphology of the composite, crystal structure and elemental analysis of the composite were characterized to confirm the presence of the CFO and HZO layers. Grazing-incidence wide-angle X-ray scattering (GIWAXS) of the unfilled CFO template and final, filled composite is shown in figures S1 and S2. From GIWAXS, it can be seen that CFO has the correct phase both before and after ALD filling and subsequent RTA treatment. Due to the ultrathin nature of the HZO layer, we were not able to be resolve any

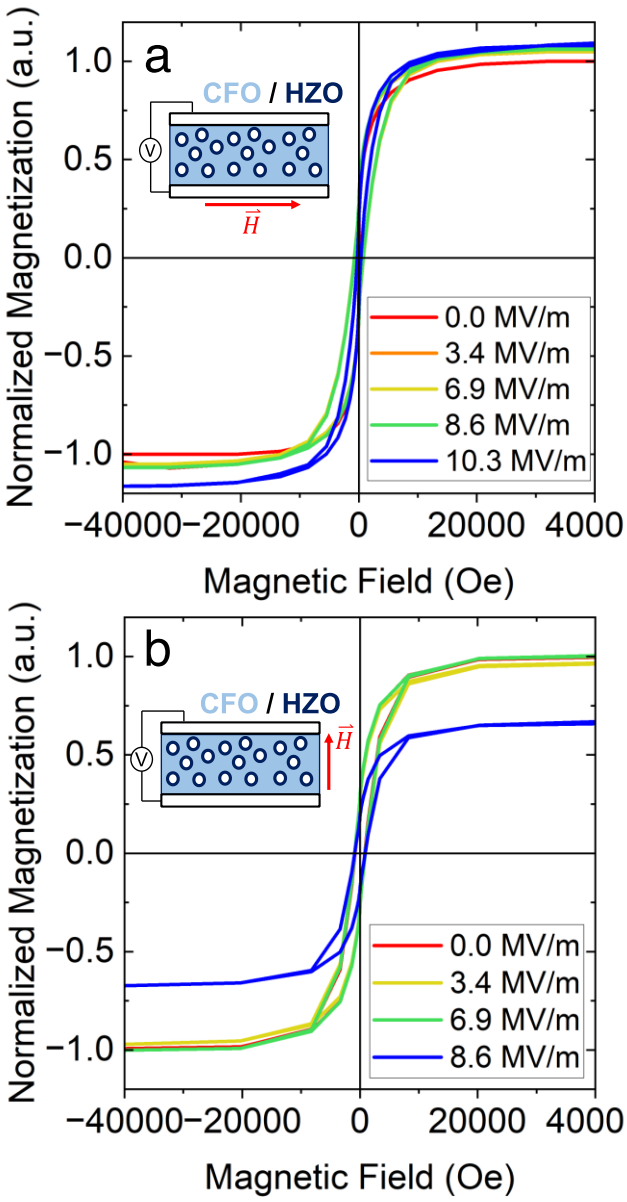

Figure 4-2. **a**) In-plane and **b**) out-of-plane magnetic hysteresis loops of *in-situ* poled composite showing magnetoelectric coupling. Magnetization was found to increase slightly in-plane and decrease out-of-plane as a function of electric field.

of the HZO peaks using X-ray diffraction, and so we turned to SEM-electron dispersive spectroscopy (SEM-EDS) to characterize the average composition of the over larger length scales (figure S3). As expected, the elemental ratio of Co:Fe was found to be 1:2 (figure S4), and the elemental ratio of Hf:Zr was found to be 1:1 (figure S5).

Additionally, the magnetic and ferroelectric properties of the CFO and HZO components, respectfully, were confirmed (figure S6). Since ferrimagnetism and ferroelectricity are ferroic ordering parameters, we expect both to exhibit hysteretic behavior. Superconducting quantum interference device (SQuID) magnetometry was used to observed magnetic hysteresis in the CFO. Its coercive field was found to be approximately 800 Oe, and its saturation magnetization was found to be 340 emu/cc, both of which are comparable to thin film literature values.[133–135] Polarization – Electric Field (PE) loops were collected to observe hysteresis in HZO. Here, the porous nature of the composites and the low thickness of the HZO resulted in too much leakage current for clean PE measurements, and so we performed PE loops that were collected on 5 nm thick dense films (figure S6). The HZO films were found to be hysteretic and have similar polarization to what has been observed in literature.[131]

With the CFO-HZO composite fully characterized, we moved onto observing their magnetoelectric coupling. Samples were electrically poled *in-situ* out-of-plane, and magnetic hysteresis loops were collected both in the plane and out of the plane of the applied magnetic field. An in-depth description of *in-situ* poling during magnetic measurements can be found in the supplemental information (figure S7). HZO should tense in the direction of the electric field (out-of-plane) and, due to the Poisson effect, compress in-plane. Since HZO is covalently bound to CFO, the strain should be transferred to CFO. As HZO and CFO are strained, the easy axis of CFO should rotate to be more in-plane. Thus, we expect to see the coercivity of the material decrease in

the in-plane direction and increase in the out-of-plane direction, which is indeed observed (figure S8). We note that the decrease in in-plane coercivity at 1.5 V of almost 50% is especially impressive considering that the composite is substrate clamped in the in-plane direction.

In addition to the large changes in coercivity, we also observe large changes in saturation magnetization (figure 2). Since CFO is a negative magnetostrictive material, magnetization should increase in the direction of compression and decrease in the direction of tension. In agreement with this hypothesis, magnetization was found to increase in the in-plane direction and decrease in the out-of-plane direction upon electric biasing, as shown in figure 2. Overall, *in-situ* poling was able to produce an 8% increase in magnetization in the plane of the magnetic field, and a 35% decrease in magnetization the out-of-plane direction. The in-plane magnetization change is likely smaller in magnitude than the out-of-plane change because the composite is substrate-clamped in-plane. Out-of-plane, however, the CFO is free to strain, so the change is larger out-of-plane than in-plane. We note that, in ferrites, it is quite common to see saturation magnetization changes in response to deformation.[136–142] It

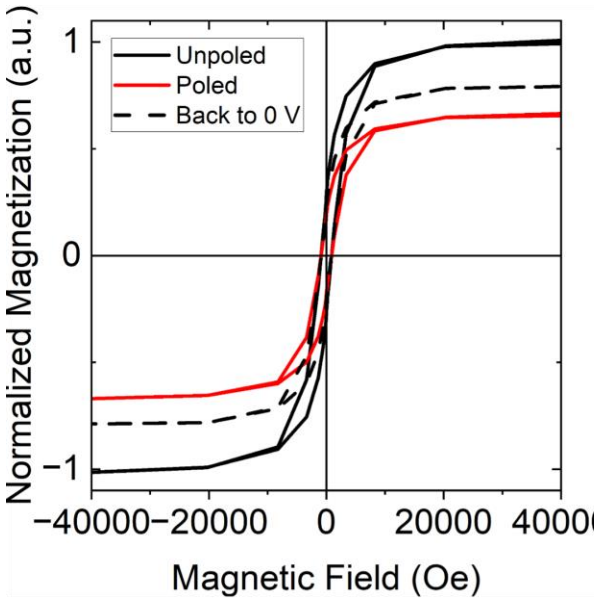

Figure 4-3. Change in out-of-plane magnetization at saturation and remanence. Upon *in-situ* poling, HZO is at the saturation strain state, and therefore CFO exhibits the largest magnetization change. After removing the electric field, however, HZO relaxes back to its remnant state, and so the magnetization of CFO relaxes back to in-between the unpoled and saturation states.

has been shown through DFT calculations that strain can change the cation distribution, changing the relative number of spins for each sublattice, which changes the saturation magnetization.[143] Thus, strain is expected to change the magnetization in ferrites, like the CFO used in this work.

We can further correlate the magnetization changes to the HZO PE field loop. At approximately 1.5 V, HZO should be at its saturation strain state, and should have the largest magnetization change. However, upon removing the applied electric field, the HZO will relax back to its remnant strain state. This means that the magnetization should also relax to a value between its poled and unpoled states. After removing the electric field from the composite, we see that the out-of-plane saturation magnetization fall to a level in between the unpoled and *in-situ* poled states (figure 3). Furthermore, we see a large difference in magnitude of the magnetization changes in samples poled

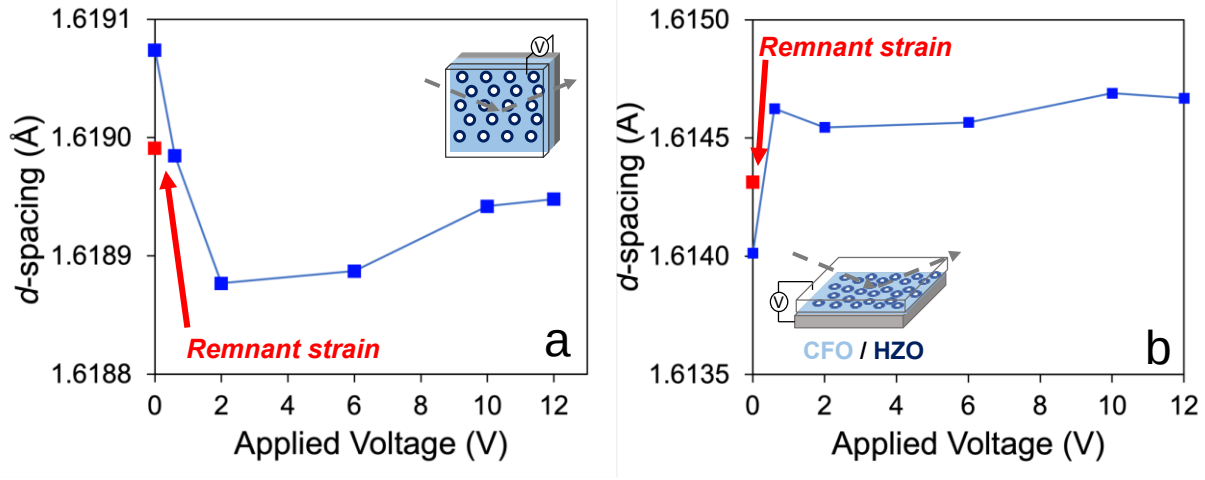

Figure 4-4. **a**) In-plane and **b**) out-of-plane peak positions of the CFO(511) reflection, as determined by X-ray diffraction for *in-situ* poled composites. The lattice spacing was found to decrease slightly in the in-plane direction and increase significantly in the out-of-plane direction as a function of electric field. Upon removing the field, the remnant strain (red marker) relaxes back to a vale between the unpoled and saturation states, echoing the magnetization data shown in figure 3.

ex situ (figure S9). The maximum magnetization change at saturation with *in-situ* poling was a 35% decrease in the out-of-plane saturation magnetization, but with *ex situ* poling, the maximum magnetization change in a remanent state was found to be approximately 20%.

We can map these changes between saturation and remanent states onto the magnetoelectric coefficient (α), which is the slope of the plot of magnetization ($\mu_0 M$) as a function of electric field (E) (figure S10). In this system, the magnetoelectric coefficient in samples poled *in-situ* was found to be 7.4×10^{-8} s·m^{-1}. This value exceeds those calculated from previously reported magnetoelectric composites utilizing HZO, where the calculated magnetoelectric coefficient was found to be 1.0×10^{-8} s·m^{-1} and 3.7×10^{-9} s·m^{-1}, respectively.[125,144] However, using the *ex situ* poling data, the magnetoelectric coefficient was found to drop by a factor of 3, down to 2.5×10^{-8} s·m^{-1}. This further illustrates the difference between the saturation magnetization changes and the remnant values.

Finally, the observed magnetization changes were mapped onto structural change in the composite films, as observed using *in-situ* poling during X-ray diffraction measurements. Details on the *in-situ* electrical poling set-up can be found in the supplemental information (figure S11). Here, we specifically monitored the CFO(511) diffraction peak position as a function of applied voltage (figure 4). It should be noted that the voltages used here slightly exceed those used for polarization-electric field characterization in figure 2, due to the lower conductivity of the carbon tape top electrode used for *in-situ* poling, which caused a small IR drop (more discussion of this point can be found in the supporting information). In-plane diffraction measurements show that the CFO(511) peak position shifts slightly to lower *d*-spacing as a function of applied bias, which indicates compressive strain. The strain state remains at saturation as the electric field us further increased beyond saturation. In the out-of-plane direction, the same CFO(511) peak was found to

shift to higher *d*-spacing, confirming tension in the out-of-plane direction. The strain state remains at approximately the same position with increasing electric field, and then returns to a remnant state upon removing the electric field. Similar to the magnetization data, the absolute value of the in-plane strain is lower in magnitude than the out-of-plane strain, likely due to substrate clamping. Thus, this data corroborates the magnetization data in figure 3, illustrating the strain-mediated mechanism of the magnetization change in the multiferroic composite.

Though the diffraction peaks of HZO were too weak to be resolved due to the very thin films employed here, since the HZO is strain-coupled to CFO, the strain change measured in the CFO(511) peak can be used to calculate a proxy for the d_{33} for HZO, which we will refer to as d'_{33}. The d'_{33} was calculated by taking the *d* spacing change from the diffraction data and dividing it by the critical voltage needed to observe the change in magnetization. Since we expected the in-plane strain to be clamped from the magnetization data, we utilized the out-of-plane peak shift of the CFO(511) to calculate the d'_{33}. The d'_{33} was found to be 1.1 pm/V, which is the order of magnitude expected for HZO. From previously reported measurements of strain in HZO, the d_{33} of 3 nm thick HZO can be extrapolated to be 1.4 pm/V.[131] The close agreement between the calculated d'_{33} and extrapolated d_{33} values again confirms the strain-mediated coupling mechanism in the composites.

In conclusion, *in-situ* measurements have allowed us to directly observe strain-mediated magnetoelectric coupling in these multiferroic composite thin films. The porous composites were synthesized by filling the pores of mesoporous, magnetostrictive CFO with ALD-grown, ferroelectric HZO. Since the polar structure of HZO is stabilized in the ultrathin regime, the HZO layer can be made thin enough to allow for residual porosity, which has been shown to improve magnetoelectric coupling, while maintaining good ferroelectric behavior. Under *in-situ* electrical

poling, the composites exhibit a large, 35% decrease in magnetization in the out-of-plane direction, and a moderate 10% increase in magnetization in the in-plane direction. The lower magnitude of magnetization change in-plane compared to out-of-plane is likely due to substrate clamping. Upon removing the electric field, the magnetization was found to relax to a remnant state consistent with the remnant polarization of HZO. The magnetization change observed when poling the composites was correlated with direct measurements of strain using *in-situ* poling with high resolution X-ray diffraction. This work thus confirms the strain-mediated coupling mechanism of these mesoporous, magnetoelectric CFO-HZO composites with residual porosity and shows that magnetization changes directly correlate with the details of strain changes. Because of substrate clamping, only minimal in-plane strain is possible, but the porosity allows for significant out-of-plane strain and out-of-plane magnetization change.

ACKNOWLEDGMENT.

The authors would like to thank Dr. Christopher Tassone, Dr. Kevin Stone, and Dr. Vivek Thampy for their assistance with *in-situ* strain measurements. The authors would also like to thank Dr. Adrian Acosta, Dr. Michael Guevara, and Alex Will-Cole for helpful discussion in this work. This work was supported by the NSF Nanosystems Engineering Research Center for Translational Applications of Nanoscale Multiferroic Systems (TANMS) under Cooperative Agreement Award EEC-1160504. Authors S.K.P. and D.D.R. also acknowledge support from a National Science Foundation Graduate Research Fellowship under Grant No. DGE-1650604 and DGE-2034835. This work made use of the UCLA Molecular Instrumentation Center (MIC). S/TEM data were acquired at the Electron Imaging Center for Nanomachines (EICN) at the University of California, Los Angeles's California NanoSystems Institute (CNSI). This manuscript contains data collected

at the Stanford Synchrotron Radiation Lightsource (SSRL), experimental station 11-3 and 17-2. Use of the Stanford Synchrotron Radiation Lightsource, SLAC National Accelerator Laboratory, is supported by the U.S. Department of Energy, Office of Science, Office of Basic Energy Sciences under Contract No. DE-AC02-76SF00515.

CHAPTER 5.

Delineating Magnetization Dynamics in Solution-Processed Doped Yttrium Iron Garnet Thin Films

Chapter 5 describes the synthesis and magnetic loss in doped yttrium iron garnet films prepared by sol-gel chemistry.

This chapter was reproduced from **Patel, S.K**.; Karaba, C.T.; Tolbert, S.H. "Delineating Magnetization Dynamics in Solution-Processed Doped Yttrium Iron Garnet Thin Films" *J. Appl. Phys.* **2023**, *133*, 014102, with the permission of AIP Publishing.

A reprint of the supporting information is given in Appendix C.

Delineating Magnetization Dynamics in Solution-Processed Doped Yttrium Iron Garnet Thin Films

Shreya K. Patel, C. Ty Karaba, Sarah H. Tolbert

ABSTRACT. In this work, thin films of ruthenium-doped and cerium-doped yttrium iron garnet were deposited on silicon using sol-gel chemistry. Doped YIG could be produced in phase pure form up to a precursor stoichiometry of $Y_3Ru_{0.1}Fe_{4.9}O_{12}$ and $Ce_{0.7}Y_{2.3}Fe_5O_{12}$. Both dopants significantly increase the coercivity and anisotropy field of the materials, either due to domain wall pinning or increased spin orbit coupling from the dopant. To delineate these two effects, the dynamic magnetic properties were studied using stripline ferromagnetic resonance (FMR). The FMR linewidth was separated into intrinsic loss and inhomogeneous line broadening. Inhomogeneous line broadening was found to dominate the magnetic losses in all the films, likely due to magnon scattering off grain boundaries, but the Gilbert damping remained fairly low. Comparing the two dopants, it was found that the Gilbert damping increased more in Ce:YIG films than in the Ru:YIG films. This finding was corroborated by changes in the anisotropy field of the films, indicating a larger contribution from spin orbit coupling from cerium than from ruthenium. Surprisingly, while magnetic loss globally increased with higher substitution, adding a small amount of dopant actually reduced the inhomogeneous line broadening in both sets of films. This was corroborated by crystallite size. The damping in Ru:YIG also decreased with a small amount of dopant, which has been predicted by Kittel for doped garnets. Thus, it follows that there is an ideal doping regime where sol-gel YIG can be doped at low levels without increasing magnetic loss.

I. INTRODUCTION.

Yttrium iron garnet (YIG) is a widely used ferrimagnetic material. Since its discovery, it has become extremely popular in spintronic devices, such as in filters [50,145] and antenna devices [56,57,146], due to its ultralow damping and magnetic softness.[147,148] YIG has also been integrated in many telecommunication devices, such as isolators [149–151] and phase shifters [152–154], since it has the unique combination of low optical loss (little absorption in the visible and IR) and a high Faraday effect.

It has been shown that YIG can be doped with many different transition metal and rare earth metals, which can dramatically change its magnetic properties, such as magnetostriction and Faraday effect.[155–160] In spintronic devices, it is desirable to have materials that exhibit high magnetostriction and low magnetic damping. While YIG exhibits extremely low damping, it has not been considered for such spintronic applications because it has little magnetostriction. Doping YIG with heavier elements, however, has been shown to increase its magnetostriction, and so doped YIG has the potential to enable new spintronic devices.[157,158,161] In addition, doped YIG, particularly with bismuth and cerium, has become extremely popular in telecommunication devices, since doping can increase the Faraday effect of the material, increasing its magneto optical figure of merit (the Faraday effect of the material divided by its optical loss).[155,159,162–164] An increased magneto optical figure of merit allows for the miniaturization of telecommunication devices. Thus, studies of doped YIG systems are crucial to enable future devices.

While these results are promising, it has also been shown that doping YIG can increase its magnetic loss, which is detrimental to spintronic and telecommunication applications respectively.[159,165] Thus, device optimization relies on the ability to study and understand the magnetic loss over a wide range of doping parameters, including dopant ion, where the dopant

substitutes, and dopant concentration. Magnetic losses can be characterized by looking at the linewidth of ferromagnetic resonance (FMR). For device design, it is particularly helpful to investigate the FMR linewidth across a range of frequencies. This can be accomplished using stripline FMR, which allows the FMR linewidth to be studied over a broad range of frequencies.[166,167]

In this work, we study the effect of doping on FMR at different sites in its crystal structure. The structure of YIG is well known.[168–170] Within the cubic crystal structure of YIG, there are three sublattice sites – dodecahedral ("*c*" sites), octahedral ("*a*" sites), and tetrahedral ("*d*" sites). Yttrium preferentially occupies the dodecahedral site. The five Fe^{3+} ions in a given formula unit of YIG are then split between two other antiferromagnetically coupled sites – two Fe^{3+} ions sit on octahedral *a* sites and the remaining three sit at tetrahedral *d* sites. As a result, YIG is a ferrimagnet with a net magnetization of one Fe^{3+} ion ($5\ \mu_B$) per formula unit. In addition to the antiferromagnetic coupling between the octahedral and tetrahedral sites, there is a weaker magnetic coupling between the dodecahedral moment (if present) and the octahedral sites, such that the tetrahedral moments couple antiferromagnetically to both the dodecahedral and tetrahedral moments.

In this work, we first investigate doping a heavier transition metal in the *octahedral and tetrahedral* iron sites of the YIG crystal structure. We chose ruthenium for this, as it has been shown to substitute at both the Fe^{3+} *a* and *d* sites in bulk crystals.[157,171] Additionally, while it has been shown that the FMR linewidth of ruthenium-doped YIG (Ru:YIG) does increase with doping, it remains at relatively low levels compared to other magnetic materials in the bulk single crystal form.[171] However, Ru:YIG has not been investigated in the thin-film form, which is far more practical for device integration.

In addition to studying the effects of doping a transition metal at the *octahedral* site, we also chose to study the effects of doping at the *dodecahedral* site to investigate the impact its coupling can have on the total magnetic properties of the doped film. We chose cerium-doped YIG (Ce:YIG), for this purpose. Ce:YIG is a well-known material for its large magneto-optical figure of merit and increased magnetostriction.[158,159,172] The choice of Ru:YIG and Ce:YIG help us isolate different effects on the magnetic properties. Ru^{3+} has the same number of valence electrons as Fe^{3+} (both d^5) but greater spin-orbit coupling, while Ce^{3+} has one valence electron in its 4*f* orbital, in contrast to Y^{3+}, which has a full 4*p* orbital. This extra electron in Ce^{3+}, as compared to Y^{3+}, has been shown to have interesting effects on the magnetic properties of YIG, such as changes in saturation magnetization, but its effect on magnetic loss across a range of dopant stoichiometries are not well understood.[159,163,164,173,174]

While YIG films are often deposited by high energy methods such as sputtering, PLD, or LPE, here, we synthesize films using sol-gel chemistry, since it is much more scalable and easier to use to study a wide range of dopants. In sol-gel chemistry, metal salts are dissolved in solution to for a 'sol', and then undergo condensation reactions to form metal-oxygen bonds, resulting in a metal oxide polymer known as a 'gel'. This technique is inexpensive, easily scalable, and allows for exploration of a wide range of dopant stoichiometries by simply changing precursor stoichiometry. There have been many successful studies that use both wet chemical synthesis and solid state chemistry to make YIG powders and nanoparticles.[173,175–181] Some of these investigations even study magnetic loss using FMR.[182,183] While the work on nanoparticles of YIG is interesting, thin films are more easily integrated into devices. It has been shown that thin films of YIG can be easily deposited on a range of substrates, including silicon, quartz, glass, and lattice matched substrates (for example, gadolinium gallium garnet, or GGG) using sol-gel methods.[184–

[189] Some studies have also investigated the dynamic magnetic properties of YIG films using ferromagnetic resonance and electron spin resonance.[184,190] There has also been previously published work on doping sol-gel YIG films, with elements such as erbium, bismuth, and cerium.[155,157,161,172,174,176,191,192] While each of these works characterized the static magnetic properties in depth, many magnetic properties, including high-frequency magnetic behavior, have not been previously investigated. Furthermore, sol-gel derived ruthenium-doped films have not been previously studied.

II. MATERIALS AND METHODS.

$Y(NO_3)_3 \cdot 6H_2O$, (99.9%, ACROS Organics), $Fe(NO_3)_3 \cdot 9H_2O$ (99+%, ACROS Organics), $RuCl_3 \cdot xH_2O$, (35%-40% Ru, ACROS Organics), $Ce(NO_3)_3 \cdot 6H_2O$ (99.5%, Alfa Aesar), and ethanolamine (98+%, Alfa Aesar) were used for the synthesis with no further purification.

For undoped sol-gel YIG, a modified procedure from the literature was used.[184] A 3:5 mole ratio of $Y(NO_3)_3 \cdot 6H_2O$ to $Fe(NO_3)_3 \cdot 9H_2O$ was used. In a typical synthesis, $Fe(NO_3)_3 \cdot 9H_2O$ (1.01 g) and $Y(NO_3)_3 \cdot 6H_2O$, (0.58 g) were dissolved in 1.5 mL of methoxyethanol with 40 μL of ethanolamine. The solution was allowed to magnetically stir for several hours, or overnight. For doped YIG, the dopant stoichiometry was varied. For Ru:YIG, the dopant ratio ranged from 0.025-0.1:1 mol (5 – 21 mg of $RuCl_3 \cdot xH_2O$) of Ru:Fe, and for Ce:YIG the dopant mole ratio of Ce:Y ranged from 0.2-0.8:1 mol [43.4-174 mg of $Ce(NO_3)_3 \cdot 6H_2O$].

Solutions were filtered with a PTFE syringe filter (Cole-Parmer, 0.2 μm) before spin coating onto 2 x 2 cm^2 (100) Si substrates. Silicon substrates were washed with ethanol and plasma etched before deposition. Films were spincoated at 3000 rpm for 30 seconds. Immediately after spincoating, films were calcined on a 400 °C hot plate in air for about a minute, then immediately

cooled down to room temperature. Though not discussed in this work, this method was also able to be used for other substrates like platinized silicon, (Pt (100 nm) -Ti (5 nm) - SiO_2 (thermally oxidized, thickness about 1 μm) -Si (100)), thermally oxidized SiO_2 (thickness about 1 μm) on Si(100)), and GGG, with the exception of not plasma etching the GGG before deposition. Rapid thermal annealing (RTA) (MPTC RTP 600xp Rapid Thermal Annealer) was used to crystallize the films under oxygen at 900 °C with a 30 second ramp and a 5 minute hold.

For stripline FMR measurements, it was found that the signal-to-noise ratio was poor for films deposited in the way described above. Therefore, thicker, multilayered films (approximately 200 nm) were made specifically for the stripline FMR measurements. This was done by spin coating the sol on silicon, calcining on a 400 °C hot plate, then repeating this process two more times for three total layers. The film was then crystallized by the same RTA process with the RTP as described above. Characterization of these thicker films can be found in the supporting information (figure S1 in the supplementary material).

X-ray diffraction patterns were collected either through grazing incidence wide angle X-ray scattering experiments (GIWAXS) with a 2D detector at an X-ray wavelength of λ =0.98 Å (thinner films) or using conventional $\theta - \theta$ powder diffraction performed on a PANalytical X'Pert Pro diffractometer at Cu Kα (λ =1.54 Å) radiation (thick films). The 2D diffraction patterns were reduced to 1D patterns using the WAXtools macro[193] in the Nika 2D package[194] for IgorPro 6.37 (WaveMetrics, Lake Oswego, OR, USA). Diffraction patterns were compared to JCPDS reference cards #00-043-0507 (for YIG) and #00-001-0800 (for ceria) using X'Pert Highscore Plus 2.0.1. Static magnetic properties were measured at room temperature using a Quantum Design MPMS3 superconducting quantum interference device (SQuID) magnetometer.

Dynamic magnetic properties were measured using a stripline ferromagnetic resonance (FMR) set up as described elsewhere.[166,195] Briefly, a short-circuited stripline is connected to a vector network analyzer (VNA). The sample is directly placed under the stripline as the VNA is used to tune frequency and a conventional electromagnet is used to tune the magnetic field applied parallel to the sample. The reflection coefficient (S_{11}) was measured as a function of both the biasing magnetic field and the frequency. As mentioned above, thicker films were needed to obtain reasonable absorption in the stripline measurement. While not discussed in this work, the authors have also used electron spin resonance (ESR) with an X-band cavity to study dynamic magnetic properties. While ESR is tuned to a cavity resonance and thus cannot provide data across a range of frequencies as the stripline set up used in this work, the cavity in ESR would allow for the detection of small absorbances in thinner films.

III. RESULTS AND DISCUSSION.

Grazing-incidence wide angle X-ray scattering (GIWAXS) was used to ensure the desired crystal structure of YIG was formed using the sol-gel method for both Ru:YIG and Ce:YIG [Fig. 1(a)]. Across the range of dopant stoichiometries investigated, Ru:YIG maintained the YIG crystal structure up to a dopant concentration of $Y_3Ru_{0.1}Fe_{4.9}O_{12}$ (figure 1(a)). For Ce:YIG, the doped films were able to maintain their crystal structure with similar phase purity until a precursor stoichiometry of $Ce_{0.75}Y_{2.25}Fe_5O_{12}$ [Fig. 1(b)]. Further cerium substitution resulted in the formation of ceria (CeO_2).

While it could not be seen at the resolution of the GIWAXS, the thin films in this study are likely under slight tensile stress due to the annealing process. Silicon has a much lower thermal expansion coefficient than YIG, and so will contract less than the YIG layer upon cooling the after RTA treatment. Since the YIG layer is clamped in the in-plane direction, the films are thus expected to show in-plane tensile stresses.

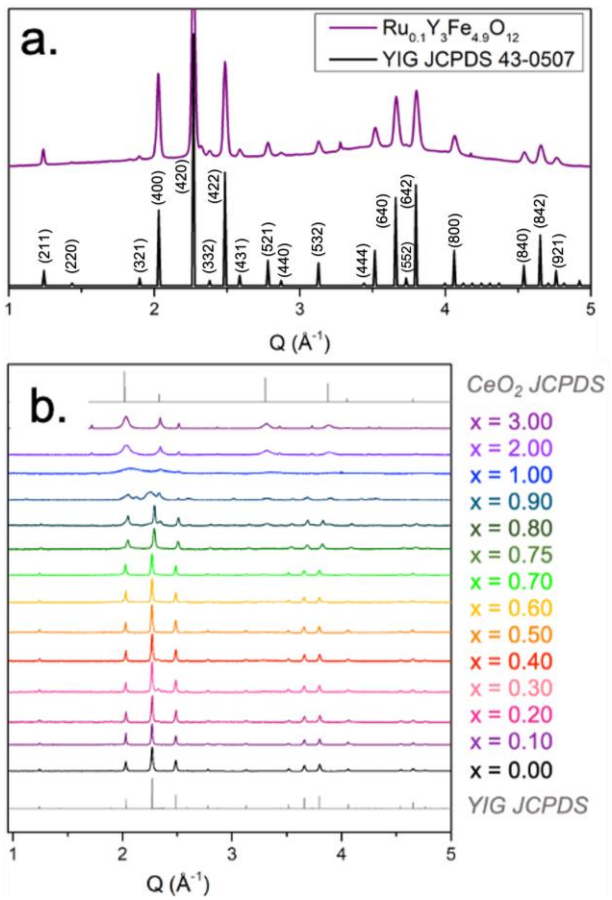

Figure 5-1. GIWAXS patterns of (a) the most doped Ru: YIG film investigated in this work ($Y_3Ru_{0.1}Fe_{4.9}O_{12}$) and (b) Ce:YIG films across a range of dopant stoichiometries, where '*x*' represents the stoichiometric addition of precursor.

The static magnetic properties of the doped YIG films were investigated using superconducting quantum interference device (SQuID) magnetometry (Fig. 2). The saturation magnetization of all the sol-gel films studied in this work are relatively close to the literature values for those of YIG.[157–159,171] However, the saturation magnetization of the cerium doped films was found to be slightly higher, between 140 and 150 emu/cc. As mentioned previously, the Ce^{3+} cation has one valence electron in its 4*f* orbital compared to Y^{3+}, which has a full 4*p* orbital. This extra electron at the *c* site couples to YIG's ferrimagnetic sublattices, increasing its overall saturation

magnetization. This increase in saturation magnetization is documented in the literature, and has been observed experimentally in Ce:YIG films deposited by PLD as well.[159,163,173]

Here, we paid special attention to the coercivity, which can be indicative of general anisotropy trends [Figs. 3(a) and 3(b)]. The coercivity of the undoped films was found to be between 20-30 Oe, which is in good agreement with literature values for sol-gel YIG films.[173,175,178] While the coercivities in this work were found to be consistent with other *sol-gel films*, it is important to distinguish that the coercivities of *single-crystal films* are often reported to be significantly lower, around 1-5 Oe.[147,196] As will be discussed in detail below, the spin coating deposition process results in more defects (such as grain boundaries and pores) than many high-energy methods of YIG fabrication, including LPE, PLD, and sputtering. Grain boundaries, cracks, and pores can cause domain wall pinning, increasing the overall coercivity of the film. Additionally, as mentioned previously, the sol-gel films described in this work have residual

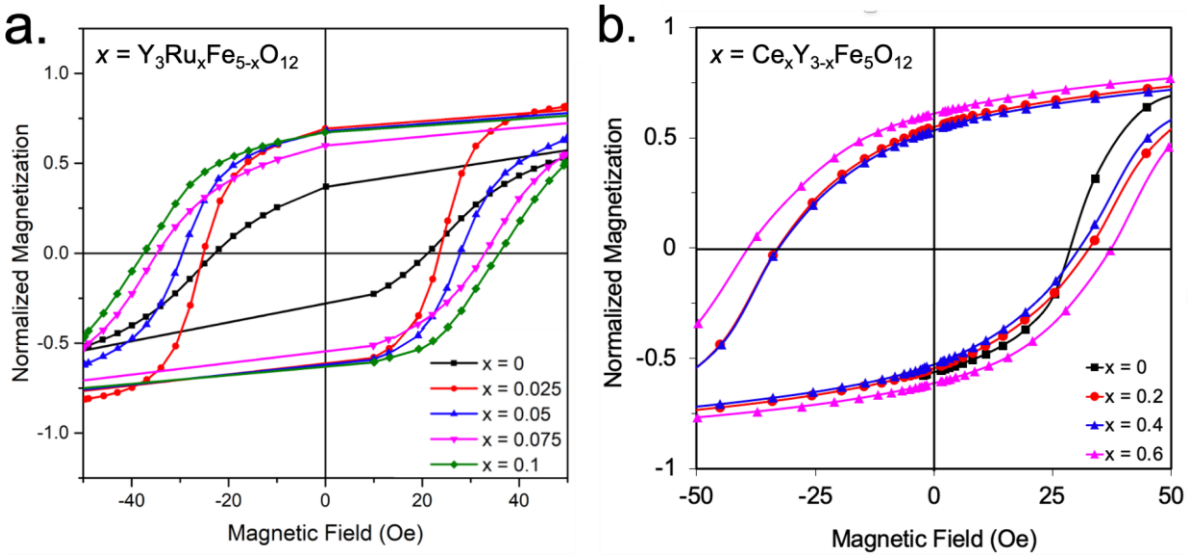

Figure 5-2. MH loops for Ru:YIG (a) and for Ce:YIG (b). In all plots, '*x*' represents stoichiometric concentration of dopant in the chemical formula of YIG, so for Ru:YIG, $x = Y_3Ru_xFe_{5-x}O_{12}$ and for Ce:YIG, $x = Ce_xY_{3-x}Fe_5O_{12}$.

tensile stresses from the difference in thermal expansion between YIG and silicon during the annealing process. These stresses add to the films' overall magnetoelastic anisotropy, which contributes to the overall coercivity of the undoped films. Though the coercivities of sol-gel films are a bit higher than epitaxial films, the films are still very magnetically soft.

Having confirmed that the undoped films had comparable coercivities to those reported in literature, the coercivities of the doped films were also investigated through SQuID magnetometry (Figs. 2 and 3). The coercivity in the Ru:YIG films were found to increase significantly upon doping, corresponding to a 39% increase [Fig. 3(a)]. Similarly, the coercivity of the Ce:YIG films increased as a function of dopant concentration but showed only a 33% increase across a much broader range of doping concentrations [Fig. 3(b)]. Note that there is some variation in the coercivity of the undoped YIG due to variations in the sol-gel process, and this likely accounts for slightly higher values obtained for Ce:YIG compared to those of Ru:YIG. There are two potential causes for the general trend of increasing coercivity as a function of dopant concentration. First, the substitution of an atomically heavier element (such as ruthenium for iron and cerium for yttrium) has greater spin-orbit coupling, which adds to the doped film's total magnetocrystalline anisotropy. This increase in magnetocrystalline anisotropy should result in increased coercivity in the doped film compared to the undoped film.[165] Second, as mentioned previously, point defects and magnetic inhomogeneities can contribute to the films' coercivity due to domain wall pinning. While the GIWAXS shows that the crystal structure is maintained as being phase pure within the detection limit, it is possible that a small amount of the dopant can also sit at grain boundaries, and act as pinning sites.

In order to delineate whether the coercivity was increasing due to increased magnetic anisotropy or from defects caused by the introduction of dopants, the anisotropy field of both sets of films were investigated using the commonly-used approach-to-saturation method [Figs. 3(c) and 3(d)].[197] Globally, for both Ru:YIG and Ce:YIG films, the anisotropy fields followed the same trend seen in the coercivity, showing an increasing anisotropy field with increasing dopant concentration. This confirms that the increase in coercivity is most likely a result of increased magnetocrystalline anisotropy due to spin orbit coupling introduced by the atomically heavier dopant, rather than the increase in coercivity being caused by domain wall pinning at defects introduced by the dopant. Interestingly, the anisotropy fields for the Ce:YIG were slightly higher than Ru:YIG (Fig. 3), which is to be expected since the Ce:YIG films also showed larger values for coercivity.

To understand why magnetic anisotropy would be higher in the Ce:YIG films than in the Ru:YIG films, the dynamic magnetic properties of the doped YIG films were investigated using stripline FMR.[166,167,198] In this experiment, the sample is placed directly under the stripline passing the applied frequency, and a conventional electromagnet is used to tune the magnetic field applied parallel to the sample. The normalized reflection coefficient (S_{11}, shown by the intensity

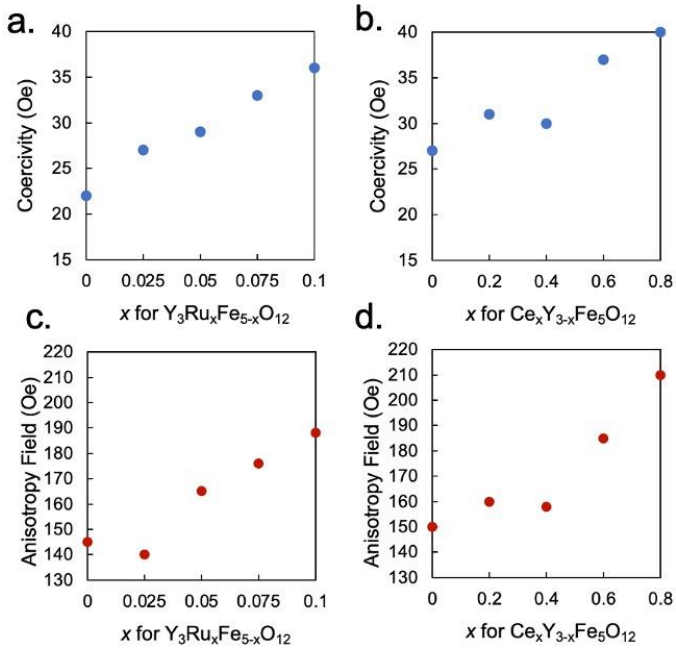

Figure 5-3. Trends in coercivity (figure 3a and 3b) and anisotropy field (figure c and d) for Ru:YIG (figures 3a and 3c) and Ce:YIG (figures 3b and 3d).

of the color bar below each FMR figure) was measured as a function of both the applied frequency and magnetic field. It is important to note that thicker films were used for this experiment in order to obtain stronger absorption in the measurement (see experimental for details). Characterization for the thicker films can be found in the supporting information. Thicker films in this study were needed to obtain reasonable absorption for stripline FMR measurements, and as seen from the 2D plots for Ru:YIG (Fig. 4) and Ce:YIG (Fig. 5), the films studied in this way showed strong S_{11} absorption, with a liner shift in the resonance frequency as a function of the applied magnetic field, as expected.

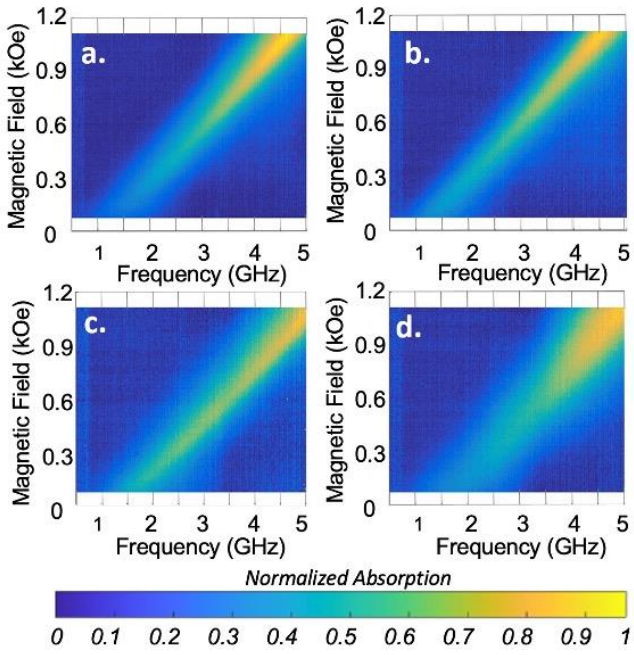

Figure 5-4. 2D plots of S_{11} absorption for Ru:YIG films collected from 500 MHz to 5 GHz and from a magnetic field of 0 Oe up to 1200 Oe for varying dopant concentrations: (a) undoped YIG, (b) x = 0.025, (c) x = 0.05, (d) x = 0.1 for $x = Y_3Ru_xFe_{5-x}O_{12}$. The color bar shows normalized absorption.

The width of S_{11} absorption correlates with magnetic loss, and thus this is the key parameter to quantify. We first looked at the total magnetic loss of undoped films. The linewidth was obtained by plotting S_{11} absorption as a function of the applied magnetic field, and then fitting this peak to find the full width at half maximum, giving us the linewidth in units of magnetic field (Oe). The experimentally obtained linewidth for the average between two sets of undoped films at 4 GHz was found to be about 260 Oe. This is much higher than what has been observed for epitaxial films of YIG on

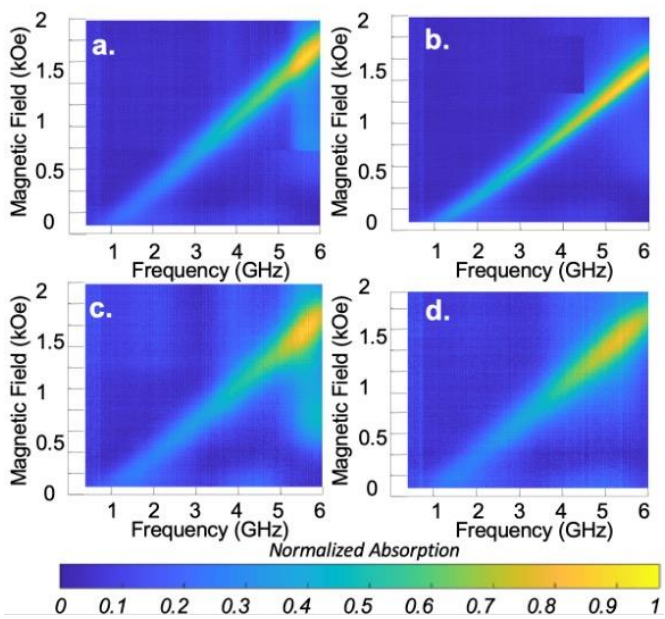

Figure 5-5. 2D plots of S_{11} absorption for Ce:YIG films collected from 100 MHz to 6 GHz and from a magnetic field of 0 Oe up to 2000 for varying dopant concentrations: (a) undoped YIG, (b) x = 0.2, (c) x = 0.4 (d) x = 0.6 for $Ce_xY_{3-x}Fe_5O_{12}$. The color bar shows normalized absorption.

lattice matched substrate (GGG) made from LPE or PLD (from 2-10 Oe at the same frequency).[147,159,199] In order to understand the sources of magnetic losses in the sol-gel films utilized in this work, we examined the linewidth as a function of frequency for both Ce:YIG and Ru:YIG [Figs. 6(a) and 6(b)]. According to Eq. (1), the linewidth can be separated into a frequency-dependent component (i.e. Gilbert damping, which is generally dominated by eddy current losses in metals) and a frequency independent inhomogeneous line broadening, [200]

$$\Delta H_{FWHM} = \Delta H_0 + \alpha\left(4\pi/\sqrt{3}\gamma\right)f \qquad (1)$$

Here, ΔH_{FWHM} is the total FMR linewidth, found by taking the full width half maximum of the absorption peak, ΔH_0 is the inhomogeneous line broadening, α is the Gilbert damping of the material, γ is the gyromagnetic ratio, and f is the resonant frequency. The frequency dependent losses come from the materials' intrinsic loss, represented by the materials' Gilbert damping. Inhomogeneous line broadening, ΔH_0, is the extrinsic line broadening, caused by magnon

scattering off of defect sites, such as pores, cracks, and impurities.[201–203] From Eq. (1), the losses from inhomogeneous line broadening and the frequency dependent losses can therefore be separated by plotting the full width half maximum linewidth (ΔH_{FWHM}) and as a function of the applied frequency, where the slope of the line is proportional to the frequency-dependent losses and the *y*-intercept is the inhomogeneous line broadening.

Such linewidth vs. frequency plots for undoped films (black symbols) are shown in Fig. 6(a) (for Ru:YIG) and Fig. 6(b) (for Ce:YIG). Single crystal YIG is known to have very little intrinsic loss, having one of the lowest Gilbert damping factors known, so it can be expected that the intrinsic, frequency dependent losses should be quite low [164,204]. Based on the relatively small slope (and thus, damping) of frequency-dependent FMR linewidths in the undoped films, we can conclude that the films studied here indeed have low intrinsic losses. We can calculate the Gilbert damping (α) by first using the Kittel equation [Eq. (2)] to solve for the gyromagnetic ratio (γ) of the undoped YIG films,

$$f = (\gamma/2\pi)\sqrt{H_r(H_r + 4\pi M_s)} \quad (2)$$

Where f is again the frequency, H_r is the resonant magnetic field, and M_s is the saturation magnetization of the film, obtained from the SQuID data discussed above.[205] Once the gyromagnetic ratio has been determined from the Kittel equation (equation 2), equation (1) can be used to solve for Gilbert damping. Since experimentally obtained values for resonant magnetic field were used to calculate the gyromagnetic ratio, the original Kittel equation does not need to be modified to include frequency shifts due to additional magnetocrystalline anisotropy. Values for Gilbert damping and inhomogeneous line broadening can all be found in Table I and plots of

Gilbert damping as a function of dopant concentration can be found in Fig. 6(c) (for Ru:YIG) and Fig. 6(d) (for Ce:YIG). For undoped films, about 90% of the total FMR linewidth was found to be the result of inhomogeneous line broadening, confirming that the inhomogeneous line broadening is the main source of losses in the films in this work. The films discussed in this work are polycrystalline, and so they contain many grain boundaries. Additionally, as mentioned previously, the films discussed in this work are expected to have defects such as micropores and cracks due to the sol-gel deposition process. It should also be noted that the films used for stripline measurements were multilayered films (see experimental and Fig. S1 in the supplementary material for more details and characterization), which can contribute to cracks and defects that broaden the linewidth further. These grain boundaries, micropores, and cracks can be seen in the cross-sectional SEM image in Fig. S1(c) in the supplementary material, and all should result in magnon scattering off these sites, damping the magnetic excitation and causing increased inhomogeneous line broadening.[200,201,206]

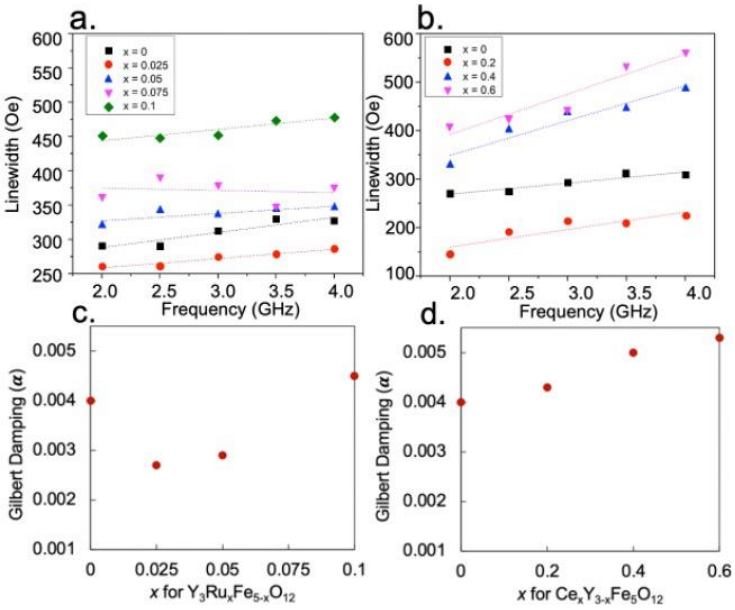

Figure 5-6. Plot of FMR linewidth as a function of frequency for (a) Ru:YIG and (b) Ce:YIG and calculated Gilbert damping for (c) Ru:YIG and (d) Ce:YIG.

Though solution processing was utilized here because it is scalable and allows us to easily tune the dopant concentration, the high inhomogeneous line broadening seen here is a significant

disadvantage. This broadening can be reduced with methods that allow for the growth of single crystal, epitaxial films, such as those formed by sputtering on GGG, PLD, LPE, and polymer assisted deposition (PAD).[147,189,199] Despite the high inhomogeneous line broadening caused by the sol-gel process, the Gilbert damping of undoped YIG was found to be quite low (3.0×10^{-3}) and the films provide an ideal way to examine changes in Gilbert damping as a function of doping level.

Dopant	***Inhomogeneous line broadening (ΔH_0)***	***Gilbert damping (α)***
Undoped*	262 Oe	3.5×10^{-3}
$Y_3Ru_{0.025}Fe_{4.975}O_{12}$	256 Oe	2.2×10^{-3}
$Y_3Ru_{0.05}Fe_{4.95}O_{12}$	325 Oe	2.4×10^{-3}
$Y_3Ru_{0.1}Fe_{4.9}O_{12}$	445 Oe	4.0×10^{-3}
$Ce_{0.2}Y_{2.8}Fe_5O_{12}$	164 Oe	3.9×10^{-3}
$Ce_{0.4}Y_{2.6}Fe_5O_{12}$	321 Oe	4.3×10^{-3}
$Ce_{0.6}Y_{2.4}Fe_5O_{12}$	354 Oe	4.8×10^{-3}

Table 5-1. Values for inhomogeneous line broadening and Gilbert damping for films studied in this work. (*averaged over data from multiple undoped films).

We now shift to looking at the losses in both sets of doped films. Similar to the undoped films, the doped films were found to also have relatively high inhomogeneous line broadening, as can be seen by looking at the *y*-intercepts of the frequency vs linewidth plots for Ru:YIG [Fig. 6(a)] or Ce:YIG [Fig. 6(b)]; the values are also quantified in Table I. In both sets of doped films, as dopant concentration increased, the inhomogeneous line broadening generally increased as well. This is likely because the addition of dopants resulted in an increased number of point defects, which increased magnon scattering, as discussed earlier. However, since GIWAXS data show no signs of impurity phases, we expect impurity domains to make up a relatively small contribution of total inhomogeneous line broadening. Diffraction peak widths also do not change significantly,

suggesting that point defects are also not the major cause of magnetic loss. Thus, we expect that the increasing inhomogeneous line broadening as a function of increasing dopant stoichiometry is largely a result of the increased magnetic disorder in the sublattice. Since the films studied in this work are not fully substituted films, the spins are placed in different electronic environments, creating disorder that can inhomogenously broaden the absorption. This has been shown to broaden zero field linewidth in other sets of doped YIG films as well.[159] Surprisingly, inhomogeneous line broadening (and the total linewidth) was found to *decrease* upon addition of only small amounts of dopant [represented by the red data presented in Figs. 6(a) and 6(b)], and then to increase again with large dopant addition. This phenomenon will be discussed later in the text.

While inhomogeneous line broadening is the predominant source of losses in both Ru:YIG and Ce:YIG, the frequency dependent losses (i.e. the Gilbert damping) were also found to increase as a function of dopant concentration. Gilbert damping values are included in Table I and plotted as a function of dopant concentration in Fig. 6(c) (Ru:YIG) and Fig. 6(d) (Ce:YIG). This global increasing trend is to be expected, as Ce^{3+} and Ru^{3+} are atomically heavier than Y^{3+} and Fe^{3+} respectively. Heavier ion substitution increases the spin orbit coupling of the overall material, which adds additional magnetocrystalline anisotropy. This is confirmed by our earlier findings on the anisotropy field of the doped films. This increase in spin orbit coupling causes fast spin relaxation, which increases the frequency dependent losses.[165] Moreover, in comparing the two sets of dopants, it was found that the intrinsic losses in Ru:YIG films [Fig. 7(c)] seemed to increase less with subsequent dopant concentration than in Ce:YIG films (figure 7(d)). This is echoed by our findings that the anisotropy fields of Ru:YIG [Fig. 3(c)] are smaller than Ce:YIG [Fig. 3(d)]. The smaller increase with Ru-doping can be explained by two things. First, the relative

concentration of ruthenium in the films studied here is significantly less than the amount of cerium dopant in the Ce:YIG films. Second, the relative amounts spin-orbit coupling introduced by ruthenium is expected to be less than cerium, as cerium is much heavier than yttrium, while ruthenium is only slightly heavier than iron.

Interestingly, while the global trends for magnetic loss are increasing, it was found in both Ru:YIG and in Ce:YIG that adding in a small amount of dopant (for Ru:YIG, up to $Y_3Ru_{0.05}Fe_{4.95}O_{12}$ and for Ce:YIG, $Ce_{0.2}Y_{2.8}Fe_5O_{12}$) actually *decreases* the total FMR linewidth [Figs. 4(a) and 5(a)], but with higher dopant concentration [Figs. 4(b)-4(d) and 5(b)-(d)], the linewidth broadens again. This was surprising, as the magnetic loss was expected to *increase* according to Vegard's law with additional dopant ion concentration. The decrease in inhomogeneous loss can be explained by using the Scherrer width of the (420) peak from the diffraction patterns presented in Fig. 1 to calculate a crystalline domain size. As shown in Fig. 7, in both Ru:YIG and Ce:YIG, adding a small amount of dopant produces an increased domain size, which is then followed by a decrease in domain size with further doping. The increase likely results from improved nucleation. Past this

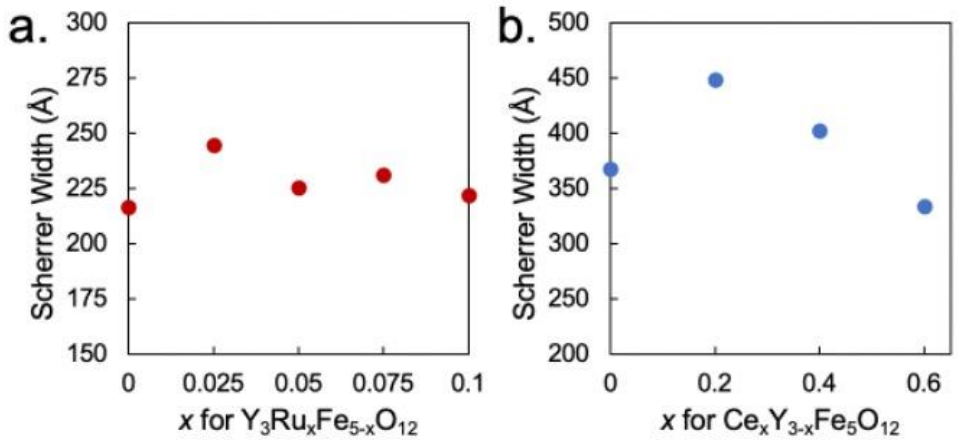

Figure 5-7. Crystallite size calculated from the (420) X-ray diffraction peaks using the standard physical Scherrer model for a) Ru:YIG and b) Ce:YIG.

initial dopant concentration, however, crystallite size is found to decrease, likely due to increased lattice distortion with higher heteroatom content. The increase in crystallite size upon addition of a small amount of dopant in both Ru:YIG and Ce:YIG is likely the cause of reduced inhomogeneous line broadening due to reduced magnon scattering off of grain boundaries.[201,202] This is followed by increased inhomogeneous line broadening as the grain size decreases at higher dopant concentration again due to magnon scattering off of the now increased number of grain boundaries.

Interestingly, the Ru:YIG samples also showed a decrease in *intrinsic* broadening at small dopant concentrations. It has been proposed by Kittel that if the damping on one sublattice (i.e. the dopant sublattice) is much larger than on the other, undoped sublattice, that the Landau Lifshitz model can be manipulated to describe the homogeneous linewidth of doped garnets as being:

$$\Delta H/H \cong \gamma_A/\alpha_B M_A \,, \tag{3}$$

where $\Delta H/H$ is the homogenous linewidth, γ_A is the gyromagnetic ratio of the undoped magnetic sublattice, α_B is the damping of the dopant sublattice, and M_A is the saturation magnetization of the iron sublattice.[207,208] This means that based on the Kittel model, if magnetic damping at the dopant site greatly outweighs the damping of the other sublattice, magnetic loss is actually expected to *decrease* at low dopant concentration. Therefore, it can be assumed that at low dopant concentrations in Ru:YIG, the magnetic damping on the dopant site is high enough relative to the undoped sublattice to follow Kittel's model for substituted garnets. At higher dopant concentrations, such as the range investigated for Ce:YIG, the effective damping at both sites to be comparable enough to deviate from the Kittel model. This would result in magnetic loss

increasing as a function of dopant concentration as would be expected for substitution of heavier elements with high spin orbit coupling.

This work thus demonstrates that there is an ideal doping regime in YIG films deposited with sol-gel methods, where dopant concentration can be maximized while not contributing to the intrinsic magnetic loss of the material. At low enough dopant concentrations, the crystallite size can be slightly enlarged, reducing inhomogeneous line broadening from magnon scattering off of grain boundaries. Additionally, as modeled by Kittel, YIG can be doped in a way where damping also decreases. Thus, YIG can be doped such that the magnetic loss *decreases* while increasing spin-orbit coupling, a crucial parameter to macroscopic material properties such as magnetostriction. It can therefore be extrapolated that an optimal doping regime can be reached, where dopant concentration is maximized while not adding additional magnetic loss. Therefore, it is important to carefully evaluate losses over a broad range of dopant concentration in designing new low loss magnetic materials for spintronic applications.

IV. CONCLUSIONS.

In conclusion, we have successfully used sol-gel methods to synthesize YIG films doped with both cerium and ruthenium. We have found that the films retain the YIG crystal structure up to a dopant stoichiometry of $Y_3Ru_{0.1}Fe_{4.9}O_{12}$ and $Ce_{0.75}Y_{2.25}Fe_5O_{12}$. Static magnetic properties are in good agreement with the literature for both Ru:YIG and Ce:YIG. Stripline FMR was then used to look at magnetic loss as dopant concentration increased. It was found that while the total magnetic loss was high compared to epitaxial and single crystal YIG, the losses were mostly attributed to inhomogeneous line broadening, and not Gilbert damping. This shows that these dopants may be useful for tuning other magnetic properties like magnetostriction and Faraday rotation if the

inhomogeneous losses are lowered. Moreover, it was found at low enough dopant concentrations, magnetic loss actually *decreases* with the addition of dopant (as predicted by Kittel). Thus, there exists a critical dopant concentration where YIG can be doped with sol gel methods, without increasing intrinsic magnetic losses.

ACKNOWLEDGEMENTS.

The authors of this work would like to thank Dr. Sophia King, Dr. Katharine Winchell, and Yutong Wu for their assistance with GIWAXS measurements. The authors would also like to thank Dr. Devin Schneider and Professor Gregory Carman for helpful discussion and assistance with FMR measurements. This work was supported by the NSF Nanosystems Engineering Research Center for Translational Applications of Nanoscale Multiferroic Systems (TANMS) under Cooperative Agreement Award No. EEC-1160504. Additionally, author S.K.P acknowledges support from the National Science Foundation Graduate Research Fellowship under Grant No. DGE-1650604 and DGE-2034835. This work utilized the California NanoSystems Institute (CNSI), the UCLA Nanoelectronics Research Facility (NRF), and the UCLA Molecular Instrumentation Center (MIC). This work also contains data collected at the Stanford Synchrotron Radiation Lightsource (SSRL), experimental station 11-3. Use of the Stanford Synchrotron Radiation Lightsource, SLAC National Accelerator Laboratory, is supported by the U.S. Department of Energy, Office of Science, Office of Basic Energy Sciences under Contract No. DE-AC02-76SF00515.

CHAPTER 6.

Perpendicular Magnetic Anisotropy in Solution-Processed Epitaxial Ru-doped Yttrium Iron Garnet Thin Films

Chapter 6 describes the synthesis of epitaxial, doped yttrium iron garnet films prepared by polymer-assisted deposition as applied spintronic materials.

This chapter is a version of Patel, S.K.; Liao, M.E.; Luccioni, D.; Robertson, D.D.; Salamat, C.Z.; Savage, E.J.; Will-Cole, A.; Sun, N.X.; Goorsky, M.S.; Tolbert, S.H. "Perpendicular Magnetic Anisotropy in Solution-Processed Epitaxial Ru-doped Yttrium Iron Garnet Thin Films" which is to be submitted to *Advanced Electronic Materials.*

Perpendicular Magnetic Anisotropy in Solution-Processed Epitaxial Ru-doped Yttrium Iron Garnet Thin Films

Shreya K. Patel[1], Michael E. Liao[2], Dorian Luccioni[2,3], Daniel D. Robertson[‡,1], Charlene Z. Salamat[‡,1], Ethan J. Savage[‡,1], Alexandria Will-Cole[4,5], Nian X. Sun[4], Mark S. Goorsky[2], Sarah H. Tolbert

[‡]Authors contributed equally to this work.

Abstract

Spintronics have emerged as the next generation of low-power devices, but their efficiency is limited by their materials properties. Low-magnetic loss and high magnetostriction are desirable for spintronics, but spin-orbit coupling prevents both from intrinsically occurring in the same material. Here, we study yttrium iron garnet (YIG), a low-magnetic loss material, and investigate two approaches to increase its magnetostriction: changing the crystalline orientation of the substrate, which strains the film, and ruthenium-doping, which strains the film and induces magnetostriction through additional spin-orbit coupling. We synthesize YIG epitaxial films using polymer-assisted deposition, a solution-based method that is inexpensive and scalable. We find that both substrate and ruthenium-doping induce enough magnetostriction to overcome shape anisotropy, resulting in perpendicular magnetic anisotropy. We fit magnetization-temperature data to a superexchange-dilution model, and the results indicate that the high magnetostriction could be due to nonstoichiometric defects, such as cation-mixing and oxygen vacancies. EPR reveals that ferromagnetic resonance fields corroborate trends in magnetostriction and nonstoichiometric defects. Moreover, magnetic loss was actually *lower* in the higher magnetostriction sample, which echoes previous modeling by Kittel. Thus, this work suggests that nonstoichiometric defects could result in low-magnetic loss, high magnetostriction materials if they are fit to the Kittel model.

1. Introduction

In the age of Moore's Law, reducing power consumption has risen to the forefront of challenges that need to be addressed in downsizing future microelectronics. The field of spintronics, which use spin waves to drive devices rather than the flow of electrons, has emerged as a low-power alternative to electronic devices.[1] For example, in the memory space, spin-transfer torque (STT)[2,3] and spin-orbit torque (SOT)[4] devices have been introduced as an alternative to conventionally-used static and dynamic random-access memory (SRAM and DRAM, respectively). STT and SOT magnetic tunnel junction (MTJ) devices are advantageous over SRAM and DRAM because they are nonvolatile, meaning they do not require current to maintain the memory state. In fact, STT-MTJs have begun to be introduced commercially due to ease of integration with CMOS technology, low power consumption, and fast switching.[5] STT and SOT is just the beginning, there is a vast amount of ongoing work in spintronics to continue to push the bounds for higher density, faster, and more efficient devices, including 'racetrack' logic devices based on the control of spin textures[6–8], magnetic field sensors[9,10], and radio-frequency and microwave devices for wireless communication[11–15]. While research toward these device applications is exciting, the practical integration of spintronic materials into devices remains challenging due to limitations in intrinsic properties.[16–18]

In this work, we study materials based on yttrium iron garnet ($Y_3Fe_5O_{12}$, or YIG), a magnetic insulator, as a potential spintronic material. Much of the preliminary work in spintronics utilized metallic magnetic materials.[17,19] Here, however, we focus on magnetic insulators, as their low electrical conductivity allows for easier propagation of spin waves due to the absence of eddy

currents.[20–23] Of the magnetic insulators, YIG has one of the lowest magnetic damping (low magnetic loss) of any material, which would be ideal for a spintronic material.[24–28]

While this is promising, it is also desirable to tune the properties of YIG to make it suitable for a given spintronic application. In particular, it would be desirable to have perpendicular magnetic anisotropy (PMA), which would allow for integration into conventionally used top-down read/write heads, smaller device sizes, and increased thermal stability for the spintronic devices.[29–32] Magnetic anisotropy in insulators is a summation of its magnetocrystalline, shape, and magnetoelastic energies.[33] Since YIG has near-zero magnetocrystalline anisotropy and intrinsically has very little magnetostriction (and thus magnetoelastic energy), shape anisotropy dominates in YIG thin films, so they often exhibit in-plane anisotropy.[34,35] However, PMA in YIG thin films can be achieved by intentional modifications to material properties resulting in increased magnetoelastic energy.

One way the magnetoelastic energy of YIG can be tuned is by substitution and manipulation of its crystal structure. YIG is a ferrimagnet with a well-known structure.[36–38] The cubic crystal structure has three sublattice sites – a dodecahedral ('*c*') site, two octahedral ('*a*') sites, and three tetrahedral ('*d*') sites. Yttrium (Y^{3+}) preferentially occupies the *c* site, and then iron (Fe^{3+}) is split between the other two sublattices. In an ideal formula unit, two Fe^{3+} cations sit at the *a* sites and three Fe^{3+} cations sit at the *d* sites. The *a* sites and *c* sites are antiferromagnetically coupled through superexchange, resulting in a net magnetization of a single Fe^{3+} cation per formula unit (5 μ_B).

In this work, we investigate doping YIG at the iron sites to increase its magnetoelastic energy. YIG can either be substituted at the yttrium site or the iron site. In both cases, yttrium and iron are typically substituted with a heavier atom, which influences the magnetic anisotropy energy

in two different ways. First, doping with a cation with a larger radius ion can strain the film. Second, doping with a heavier element can increase spin orbit coupling, which increases its magnetocrystalline anisotropy and magnetoelastic energy.[39] Thus, many doped YIG systems have been reported.[35,40–42] Doping at the yttrium site is much more thoroughly studied than at the iron sites, partly because cerium and bismuth substitution has been found to greatly increase Faraday rotation for magneto-optical applications.[43–50] Additionally, many efficient rare earth-substituted epitaxial garnet films have been reported to exhibit PMA, which are promising for the aforementioned spintronic devices.[21,48,51–55] While the doped YIG systems are exciting, it is important to note that substitution often comes at the cost of increasing the magnetic loss of a material.[56] Here, doping is expected to mostly increase the intrinsic magnetic loss due to the additional magnetocrystalline anisotropy.[39,57]

While much existing work focuses on doping at the yttrium site, here, we study the effect of doping at the iron sites, which is much less understood. In the few works that substitute at the iron site, most focus on substituting YIG iron sites with Co^{2+} (often counter-doped for charge neutrality). Substitution of just a small amount of Co^{2+} has been found to drastically change the magnetoelastic and magnetocrystalline energies of YIG, but at the expense of a large accompanying magnetic loss.[34,58–60] Similarly, of Ru-doping has been found to have a dramatic effect on the magnetic properties in both bulk[61] and thin film[39] systems, with just under 1% of substitution of the iron sites (compared to 30 – 100 % of the yttrium sites in rare-earth doped garnets). However, compared to Co-doping, Ru-doping seems to have less of a comparative impact on magnetic loss.[39,62,63] To the best of our knowledge, no epitaxial Ru-doped YIG (Ru:YIG) thin film systems have been reported to date. Thin film morphology is advantageous over bulk single crystals for device applications, and advantageous over previously-reported polycrystalline thin

films because it mitigates magnetic loss at grain boundaries.[39] Thus, Ru:YIG could add enough magnetoelastic energy to achieve PMA, while maintaining low magnetic loss.

In addition to studying the effects of Ru-doping YIG on its magnetoelastic energy, we are also interested in using the substrate to push the preferred direction of magnetic anisotropy in the out-of-plane direction. While epitaxial YIG is usually deposited on gadolinium gallium garnet ($Gd_3Ga_5O_{12}$, or GGG) due to its close lattice match, the lattice constant of the substrate can be slightly manipulated to change the magnetic properties of YIG. Typically, substituted-GGG ($Gd_{2.6}Ca_{0.4}Ga_{4.1}Mg_{0.25}Zr_{0.65}O_{12}$, or SGGG) is used to compressively strain YIG in plane[64–66], while yttrium aluminum garnet ($Y_3Al_5O_{12}$, or YAG) can be used to add tensile strain to YIG[67–70]. Both substrates have been shown to induce PMA in thin films, but similarly to doping, at the cost of magnetic loss. It has been shown that the additional strain from changing the substrate has been shown to increase the magnetic loss.[21,64,67,69] This is likely because changing the relative bond lengths in the crystal structure places the iron cations in a more inhomogeneous electronic environment.

Here, we seek to add a much smaller amount of strain in tandem with Ru-doping by observing magnetic anisotropy on different orientations of GGG, rather than using a different substrate altogether. Specifically, we study the effect of growth on GGG(100) and GGG(111). Growth of doped YIG on GGG(100) is known to induce a tetragonal distortion of the cubic structure, whereas growth of YIG on GGG(111) is known to induce a rhombohedral distortion of the cubic structure.[52–54,71,72] These different distortions can impact both the magnetoelastic energies and the magnetic loss, so it is important to understand the impact the two different orientations of substrates can have on doped garnets. Furthermore, the surface of GGG(111) face is more anisotropic than GGG(100) face, which is known to induce faster growth.[73] These growth

kinetics may add additional growth-related strains that could change the magnetism of Ru:YIG, and so it is important to understand the effect of substrate orientation.

Interestingly, the oxygen content can also dramatically change the strain and therefore magnetism of YIG. For example, just the stoichiometric deficiency of 0.1 can increase the magnitude of the uniaxial magnetic anisotropy by three times compared to the expected oxygen stoichiometry.[74] The oxygen content of a film can be changed by changing the partial pressure of oxygen in deposition[71,75–77], annealing in a reducing environment (such as with pyrolyzed graphite)[78], or Ca^{2+} doping[74,79–82], which leaves oxygen vacancies in the unit cell. Oxygen vacancies add tensile strain in plane, whereas oxygen-rich films add compressive strain.[82,83] Therefore, in this work, we fit magnetization-temperature measurements to a superexchange model to understand the effects Ru-doping and substrate can have on the oxygen content of the film.[84]

While a vast majority of published YIG epitaxial films are made with either gas-phase deposition (such as pulsed-laser deposition, PLD, and sputtering)[25,28,48,65,66,70,85,86] or from molten crystal (such as liquid-phase epitaxy, LPE)[27,58], here, we utilize solution-processing since it is cost-effective and scalable. Sol-gel chemistry is one solution-processing method that has been used to make YIG polycrystalline thin films, and while this method has allowed for a lot of exploration, the magnetic loss in these films is often large due to magnon scattering off grain boundaries.[39,42,87–93] Therefore, in this work, we utilize polymer-assisted deposition to grow epitaxial films.[94–96] In polymer-assisted deposition, metal salts are dissolved in water with a polymer that has charged sites and often a chelating agent, such as EDTA. The metal-EDTA complex can then bond to the changed sites on the polymer. This solution can be spin-coated onto a substrate. The polymer holds the cations far enough apart so that they do not react until the film is heated and the polymer is pyrolyzed, at which point the cations nucleate off the substrate to form an epitaxial thin film. This

strategy is robust and has been shown to make a wide range of high-quality epitaxial metal-oxide films, including undoped YIG.[97–99] Therefore, given the ease, cost-effectiveness, and scalability of polymer-assisted deposition, we have utilized it here for growth of our thin films.

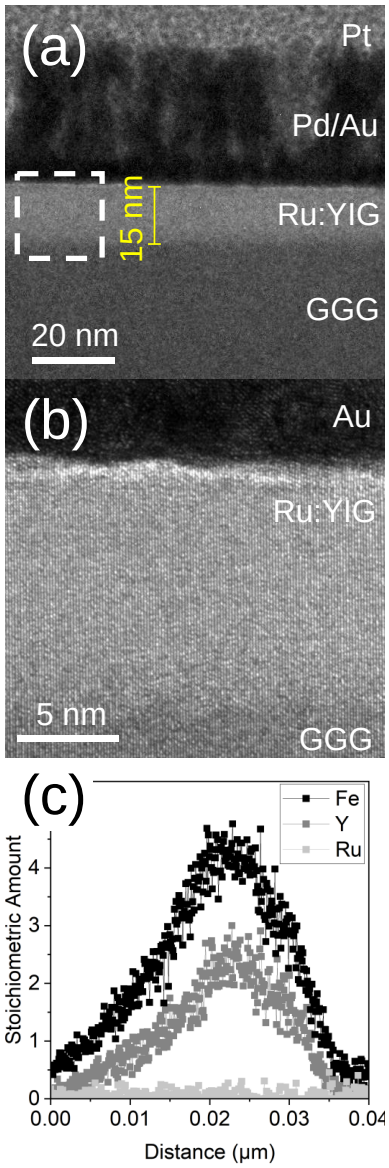

Figure 6-1. Characterization of the Ru:YIG(111) film using (a) + (b) HRTEM imaging and S/TEM EDS (c). Fig 1(a) shows a cross section of TEM lamella with highlighted box shown in (b). Lattice

planes are clearly visible, indicating good epitaxy. Fig. 1(c) Shows a line scan through the film shows an appropriate ratio of yttrium to iron.

2. Results and Discussion

Polymer-assisted deposition was used to deposit undoped YIG on GGG(100) and GGG(111), as well as Ru:YIG (with a solution stoichiometric ratio of $Y_3Fe_{4.955}Ru_{0.045}O_{12}$) on GGG(100) and GGG(111), resulting in four total samples; YIG(100), YIG(111), Ru:YIG(100), and Ru:YIG(111). Details for polymer-assisted deposition of the films can be found in the experimental section. This stoichiometry of Ru:YIG was chosen based on previous work on bulk single crystal Ru-doped YIG, which showed that large magnetostriction (λ_{100} = 48.7 ppm, λ_{111} = 11.1 ppm) could be achieved at a 1/110 stoichiometric ratio of Ru/Fe.[61] As mentioned above, solution-processing typically produces polycrystalline films, but the polymer-assisted deposition method we use here results in epitaxial films. To visualize the epitaxy in the film, we used high resolution transmission electron microscopy (HRTEM) on Ru:YIG(111) as a representative example (Fig. 1(a), 1(b)). At high magnification, lattice plans extend through the substrate and continue throughout the film, indicating epitaxial growth off the substrate. All films were found to be within a narrow film thickness ratio between 15 nm - 20 nm from profilometry, which matches the thickness visualized through S/TEM. This thickness is typical for polymer-assisted deposition, and can be tuned slightly by changing the concentration of the solution and the branching of the polymer.[95] The magnified image of the film (Fig. 1(c)), shows clear lattice planes throughout the substrate and the film, indicating high-quality epitaxy in the film.

Next, in order to confirm the desired elemental ratio of the film, scanning/transmission electron microscropy (S/TEM) was used for EDS (Figure 1(c)). Here, we specifically studied the

Ru:YIG(111) sample, since its synthesis deviates furthest from the previously reported polymer-assisted deposited YIG(100) and YIG(111).[99] A S/TEM-EDS line-scan through the thickness of the film confirms that the ratio of Y/Fe throughout the film is approximately 0.6. Since ruthenium is doped at a much smaller level (with an expected stoichiometric ratio of Ru/Fe being 1/110), it is more difficult to quantify than Y:Fe, but the EDS ratio was found to be within error of the targeted stoichiometric ratio, with $1/145 \pm 55$.

Since the error in stoichiometry in the EDS was so large, we also performed inductively coupled plasma - optical emission spectrometry (ICP-OES) on both the undoped and doped spin-coating solutions used for the films. Details for ICP-OES calibration and measurement can be found in the experimental. The ratio of Y/Fe in both solutions (0.616 in undoped and 0.622 in doped) were found to match the S/TEM EDS line scan, which indicates that the elemental ratio found from ICP-OES can be used as a proxy for the elemental ratio in the film. The stoichiometric ratio of Ru/Fe was found to be 1/108, very close to the targeted ratio.

XPS was also performed for elemental characterization of the film (Fig. S1-S2). As mentioned previously, YIG has three sublattice sites, the *c* site where Y^{3+} sits, the *a* sites where two Fe^{3+} sits, and the *d* sites where three Fe^{3+} sits. From XPS, we see that our spectrum matches others reported for YIG.[22,71,100,101] There is one spin-orbit split peak representing a single electronic environment for yttrium, corresponding to the *c* site. We also see that there are two spin-orbit split peaks for iron, with a satellite peak between them, corresponding to the *a* and *d* sites. There are two oxygen peaks, which has been observed in previous XPS studies of YIG.[100] XPS, being a surface-sensitive technique, also shows that the surface is slightly yttrium-rich, compared to the rest of the film. This can be expected, given the relative surface energies of yttrium oxides and iron oxides, and has been observed in PLD YIG films before.[54]

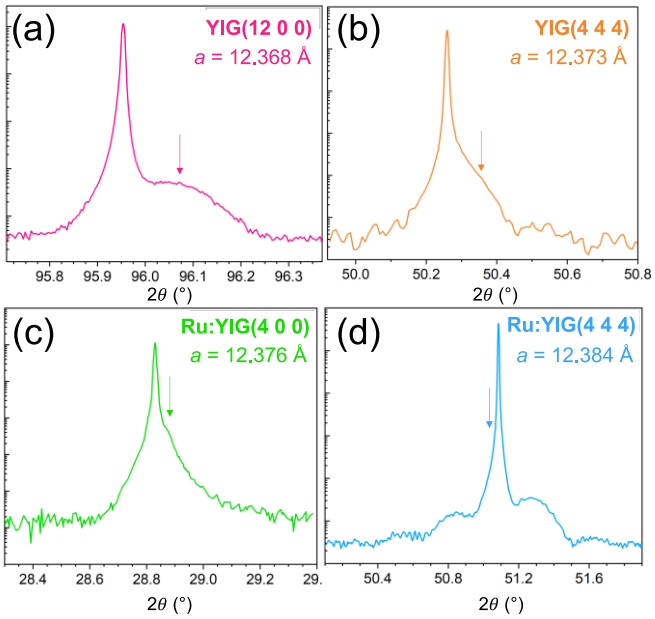

Figure 6-2. Out-of-plane X-ray diffraction patterns of a representative peak for (a) YIG(100), (b) YIG(111), (c) Ru:YIG(100), and (d) Ru:YIG(111), with the specific reflection denoted in the upper-right corner. The lattice parameters were calculated from their relative peak positions from the underlying substrate reflection and are provided for reference.

With the elemental ratio confirmed, we moved onto investigating the crystal structure of the films with high resolution X-ray diffraction (Fig. 2). Across the board, the films were found to have uniform thickness and high crystallinity, as evidenced by the Laue oscillations in the patterns. Fringes are also seen in X-ray reflectivity (XRR), which is further indicative of the films' high uniformity in thickness across the entire film area due to a larger X-ray footprint (Fig. S3). We were able to observe other reflections through X-ray diffraction as well (Fig. S4).

In order to discuss the relative strain states of the films, we first calculated the value of the unstrained lattice constant of the samples, which can be found in the upper-right corner of the

diffraction patterns in Fig. 2. The experimentally observed in-plane lattice constant of the GGG substrate was set to its known, literature value of 12.383 Å.[35,102] Then, the fitted peak shift in the film off the GGG peak was used to calculate the in-plane lattice parameter. Strained epitaxial films experience in-plane biaxial stresses applied by the underlying bulk substrate.[103,104] In-plane biaxial stress in films grown on GGG(100) results in tetragonal distortion where the in-plane lattice parameter strains towards the in-plane lattice parameter of the GGG substrate. Since the Poisson's ratio of YIG is well-known (0.29), the out-of-plane lattice parameter can be calculated according to a previously-recorded procedure.[35,105] The calculation of lattice parameter for films grown on GGG(111) is a bit more complicated, due to the loss of orthogonality of the unit cell axis after strain. Films grown on GGG(111) are expected to undergo a rhombohedral distortion. A rhombohedral-to-hexagonal calculation can be used in order to simplify the calculation of strain.[106] Briefly, the Miller indices of a rhombohedral lattice (*hkl*) can be transformed to a hexagonal lattice (*HKL*) by equation (1):

$$\begin{pmatrix} H \\ K \\ L \end{pmatrix} = \begin{pmatrix} 1 & -1 & 0 \\ 0 & 1 & -1 \\ 1 & 1 & 1 \end{pmatrix} \begin{pmatrix} h \\ k \\ l \end{pmatrix} \quad (1)$$

It can then be assumed that the $(11\bar{2})$ of the film strains to the $(11\bar{2})$ of the in-plane lattice parameter of the hexagonal unit cell. The lattice constant of the hexagonal structure (a_H) can then be calculated with equation (2):

$$a_H = \sqrt{12 d_{11\bar{2}}^2} \quad (2)$$

The *c*-axis parameter can then be calculated from the *d*-spacing obtained from the peak position of the film (where *c* of the hexagonal lattice is equal to 12 times the *d*-spacing). Finally, the rhombohedral lattice constant can be calculated from equation (3):

$$a_R = \frac{1}{3}\sqrt{3a_H^2 + c^2} \tag{3}$$

This calculation has been used for this purpose before in rhombohedral lattice strain both in garnets[48,52,54] and in epitaxial metal-oxide thin films broadly[107].

Interestingly, as can be seen from Fig. 2, the out-of-plane lattice constant values for all samples (with the exception of the Ru:YIG(111) sample) indicate that the films are all under compressive strain compared to the substrate. This is in contrast to many PLD films, which observe the film peak under tensile strain with respect to the substrate.[20,44,48,65,71,108–110] We note that the bulk lattice constant of YIG (12.373 Å)[111] is smaller than the bulk lattice constant of GGG (12.383 Å)[35,102], and even taking thermal strain into account (calculated by multiplying the difference in thermal expansion of YIG[112] and GGG[113] by the annealing temperature), we still expect YIG to be under out-of-plane compressive strain with respect to GGG. There are many factors in the PLD growth process, such as the lasing conditions, condition of the target, and attenuation of the window and mirrors which have been reported to cause additional growth-related strains in PLD films.[52,71] Thus, the difference in synthetic conditions here likely leads to the out-of-plane compressive strain of the film with respect to GGG.[67,69,114]

In comparing the calculated lattice constants, two trends were observed. The first observation is that the films made on GGG(111) have a larger lattice constant than those grown on GGG(100). This is consistent with previous work reporting that PLD YIG films, both undoped

and doped, have observed a similar increase in the lattice parameter by depositing on GGG(111) as opposed to GGG(100).[48,54] The GGG(111) has a more anisotropic surface than the GGG(100), and as a result, it is known that YIG grows faster off the GGG(111) face than the GGG(100) face.[73] Since oxygen vacancies are also known to cause out-of-plane tensile strain in YIG, it is possible that this faster growth kinetically traps oxygen vacancies in the films grown on GGG(111).[74,79,80] The second observation we had was that the Ru-doped films exhibit a larger lattice constant than the undoped films. While bulk, single-crystal Ru:YIG has been reported to have a slightly larger lattice constant of 12.378 Å (compared to 12.376 Å for undoped YIG[111]), the magnitude of strain change observed here with Ru-doping alone was larger than the difference in bulk lattice constants (12.368 Å vs. 12.376 Å for our YIG(100)/Ru:YIG(100), respectively).[115,116] As such, this larger-than-expected increase likely results from structural defects like oxygen vacancies that may incorporate along with the Ru dopant, which we will discuss later along with the magnetization data.

Next, we evaluated the effect of these trends in strain on the films' magnetism. Superconducting quantum interference device (SQuID) magnetometry was first used to collect magnetization - magnetic field (MH) loops (Fig. 3). For each film, we collected an MH loop with the applied magnetic field aligned in the plane of the film (in plane, denoted with solid lines) and out of the plane of the film (out of plane, denoted with dashed lines). The large paramagnetic signal from the GGG was subtracted from the experimentally collected MH loops to obtain signal from the film (see experimental for more information on the background subtraction). Across the films studied in this work, they were all found to have close to expected literature values for saturation magnetization (140 emu cm^{-3}).[24,63,117] While some doped YIG structures (namely rare-earth substituted garnets) can exhibit changes in saturation magnetization as a result of contributing

extra unpaired spins to the structure, Ru:YIG is reported to exhibit near literature values for saturation magnetization, so this observation is to be expected.[39,116] The coercivities were also found to be consistent with literature results, approximately 20-35 Oe.[39,62,117]

The most striking feature of the MH loops is their direction of preferred anisotropy. As mentioned previously, magnetic anisotropy in these systems can be thought of a summation of its magnetocrystalline, shape, and magnetoelastic energies.[33] Undoped YIG has very little magnetocrystalline anisotropy and nearly zero magnetostriction, so typically in thin films, shape anisotropy dominates, resulting in a strong preference for magnetization in the in-plane direction. This was found to be the case in YIG(100), YIG(111), and Ru:YIG(100) (Fig. 3(a-c)). However, we noticed a large change in the magnetic anisotropy in the Ru:YIG(111) sample - instead of being dominated by shape anisotropy, the film exhibited perpendicular magnetic anisotropy (Fig. 3(d)).

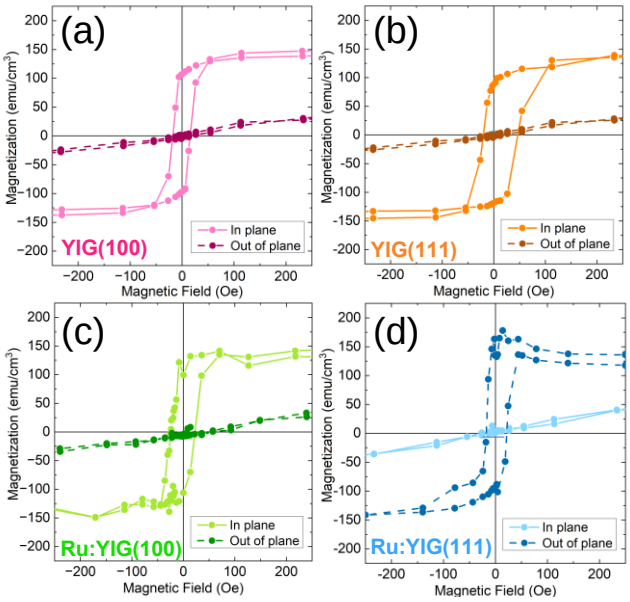

Figure 6-3. Magnetization - Magnetic Field loops for all four samples studied, (a) YIG on GGG(100), (b) YIG on GGG(111), (c) Ru:YIG on GGG(100), and (d) Ru:YIG on GGG(111). MH loops collected in the plane of the applied magnetic field are shown with solid lines and the MH

loops collected out of the plane of the magnetic field are shown in dashed lines. All films exhibit the expected in-plane anisotropy due to large, dominating shape anisotropy, with the exception of Ru:YIG(111), which exhibits perpendicular magnetic anisotropy.

To understand the large difference in magnetic anisotropy in Ru:YIG(111) as opposed to the other films studied here, we calculated magnetic anisotropy energies (Table 1). First, we calculated the total magnetic anisotropy energy from the MH loops according to a standard integration method.[118] The MH loops shown in Figure 3 were fit to a sigmoidal function. The integral of the out of plane (OOP) MH loop was then subtracted from the MH loop collected in the plane of the magnetic field as shown in equation (4), and then the integral was converted from erg cm^{-3} to kJ m^{-3}:

$$E_{\text{Total}} = \left[\int_0^M H\mathrm{d}M \ \frac{\text{erg}}{\text{cm}^3}\right]_{\text{OOP}} - \left[\int_0^M H\mathrm{d}M \ \frac{\text{erg}}{\text{cm}^3}\right]_{\text{IP}} \quad (4)$$

Using this convention of this equation, any negative values of energy should indicate preference for the in plane direction and any positive values of energy should indicate preference for out of plane anisotropy. It should be noted that given the noise level of the MH loops, there was some standard deviation in the fitting, which was accounted for in the reported values for total magnetic anisotropy in Table 1. Magnetocrystalline anisotropy numbers were taken from literature sources for bulk, single-crystal values.[116,119] Ruthenium-doping adds spin-orbit coupling, and therefore adds to the magnetocrystalline anisotropy.[61] However, this change in magnetic anisotropy is very small in comparison to the other sources of anisotropy energy. The energy from

shape anisotropy can be calculated from the difference between the out of plane shape anisotropy energy and the in plane shape anisotropy energy as shown in equation (5):[33]

$$E_{\text{shape}} = \left[N\frac{\mu_0}{2}M_s^2\right]_{\text{OOP}} - \left[N\frac{\mu_0}{2}M_s^2\right]_{\text{IP}} \quad (5)$$

where N is the demagnetization factor (equal to 0 for film geometry out of plane with the magnetic field and equal to 1 for a film geometry in plane with the magnetic field), μ_0 is the permeability of free space, and M_s is the saturation magnetization. Due to the noise in the MH loop, there is a small amount of standard deviation in the saturation magnetization, which is accounted for in Table 1. Besides this, the saturation magnetization is large and prefers in plane anisotropy, for all the films studied.

Assuming that the only contributions of anisotropy are those stemming from magnetocrystalline, shape, and growth, we can subtract magnetocrystalline anisotropy energy and shape anisotropy energy from the total magnetic anisotropy energy to obtain the magnetoelastic energy. We find that the magnetoelastic energy is larger in films grown on GGG(111) than GGG(100) and that the magnetoelastic energy in the Ru-doped YIG is larger than the undoped films. Both these trends echo the trends in tensile strain from the diffraction data discussed earlier.

Table 1. Calculated values for different contributions to the total magnetic anisotropy energy, calculated from magnetometry data. Literature values for magnetocrystalline anisotropy, measured in bulk, single-crystals, were used here.[116,119]

	YIG(100) (kJ/m^3)	YIG(111) (kJ/m^3)	Ru:YIG(100) (kJ/m^3)	Ru:YIG(111) (kJ/m^3)
Total Magnetic Anisotropy Energy	-8.6 ± 0.1	-8.2 ± 0.1	-4.7 ± 0.3	+0.7 ± 0.2
Magnetocrystalline Anisotropy Energy	0.05[a)]	0.05[a)]	-0.55[b)]	-0.55[b)]
Shape Anisotropy Energy	-11.4 ± 0.1	-11.5 ± 0.1	-11.5 ± 0.2	-11.5 ± 0.4
Magnetoelastic Energy	2.8 ± 0.2	3.3 ± 0.2	6.9 ± 0.5	12.3 ± 0.6

[a)] Taken from experimentally-collected data for undoped single-crystal YIG[119]; [b)] Taken from from experimentally-collected data for Ru-doped single-crystal YIG[116].

To begin to understand the relationship between the correlated trends in lattice parameter and magnetoelastic energy, we calculated the magnetostriction of the film according to previously reported methods.[54,107,110] For films grown on GGG(100), the magnetostriction can be calculated from the magnetoelastic energy with equation (6):[53,120]

$$E_{\text{magnetoelastic}} = -\frac{3}{2}\lambda_{100}(c_{11} - c_{12})(\varepsilon_{zz} - \varepsilon_{xx}) \quad (6)$$

where λ_{100} is the magnetostriction, c_{11} and c_{12} are the literature elastic constants for YIG[121], ε_{zz} is the difference between the measured out of plane lattice parameter and the unstrained lattice parameter, ε_{xx} is the difference between the in plane lattice parameter (assumed to be strained to the lattice constant of GGG) and the unstrained lattice parameter. For films grown on GGG(111), the magnetostriction can be calculated from the magnetoelastic energy in equation (7):[52]

$$E_{\text{magnetoelastic}} = -\frac{9}{8}\lambda_{111}c_{44}\left(\frac{\pi}{2} - \beta\right) \tag{7}$$

where λ_{111} is the magnetostriction, c_{44} is the literature shear modulus for YIG[121], and β is the angle of the rhombohedrally distorted corner (α), which can be calculated through equation (8):

$$\sin\frac{\alpha}{2} = \frac{3}{2\sqrt{3+\left(\frac{c}{a_H}\right)^2}} \tag{8}$$

where c and a_H are the c-axis lattice constant and hexagonal lattice constant referred to in equation (3). The calculated magnetostriction constants are shown in Table 2. Here, we find that undoped YIG is a negative-magnetostrictive material, which is consistent with bulk, single-crystal undoped YIG (reported to be λ_{100}= -1.47 ppm and λ_{111}= -2.73 ppm).[35] However, the magnitude of magnetostriction that we calculate is larger than has been reported in bulk, single-crystal YIG. This may be indicative of some additional growth-related anisotropy in growing on GGG(111) vs. GGG(100), which we will address in discussing the magnetization-temperature data. While undoped YIG was found to have negative magnetostriction, Ru:YIG(111) was calculated to be a positive-magnetostrictive material, which is consistent with bulk, single-crystal Ru:YIG literature

values.[61] The magnetostriction for Ru:YIG was found to greatly exceed the magnetostriction for undoped YIG, which has been seen before in bulk, single-crystal Ru:YIG.[61]

Table 2. Calculated values for magnetostriction, calculated from the magnetoelastic energies in Table 1.

	Magnetoelastic energy (kJ/m^3)	**λ_{Total} (ppm)**
YIG(100)	2.8 ± 0.2	-4 ± 0.3
YIG(111)	3.3 ± 0.2	-20 ± 1.5
Ru:YIG(100)	6.9 ± 0.5	-28 ± 2.0
Ru:YIG(111)	12.3 ± 0.6	48 ± 2.5

We then turned to comparing the calculated magnetostriction, the magnetism of the film, and the strain state of the film. The YIG(100), YIG(111), and the Ru:YIG(100) were found to be compressively strained in the out of plane direction with respect to the substrate (from diffraction in Fig. 2) and is assumed to be under tension in the in plane direction to conserve volume. As mentioned previously, undoped YIG is negative magnetostrictive, meaning that the direction of compression is the preferred direction of magnetization. However, this small, magnetoelastic preference for the out of plane direction is outweighed by the large, in plane shape anisotropy, and so the overall preferred direction of magnetic anisotropy is the in plane direction. In contrast, the Ru:YIG(111) film was found to be under tensile strain in the out of plane direction, and assumed to be under in plane compression. Since it is positive magnetostrictive, its magnetization actually

prefers the out of plane direction (the direction of tension). The magnitude of magnetostriction, and the strain, is high enough to outweigh the shape anisotropy, resulting in a net magnetization preference for the out of plane direction.

Since the calculated value for magnetostriction in the undoped sample was larger in magnitude than expected for bulk, single-crystal, we suspected potential growth-induced magnetic anisotropy. Larger-than-expected calculated magnetostriction values have previously been attributed to growth-induced anisotropy in PLD YIG before, and so we hypothesized the observed deviation in magnetostriction in the samples described here could be similar, despite the different synthetic technique.[110] Here, we suspected two possible causes for growth-related anisotropy. The first is cation mixing, where yttrium could potentially substitute in at the iron sites. This has been reported to cause significant growth-related anisotropy in garnet structures before.[71] The second potential cause of growth-related anisotropy is oxygen vacancies. As mentioned previously, oxygen stoichiometry can dramatically increase both the lattice constant[83] and the uniaxial magnetic anisotropy[74]. With this in mind, we set out to characterize the cation mixing and oxygen vacancies in the films.

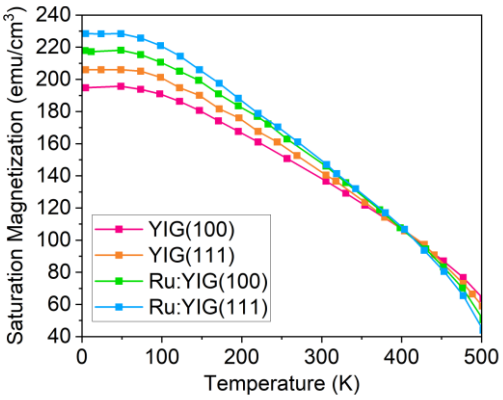

Figure 6-4. Fitted magnetization-temperature data collected using SQuID magnetometry, which was fit to Dionne's superexchange model to understand the calculated magnetostriction values.

Both cation mixing and oxygen vacancies can change the compensation temperature in ferrimagnetic YIG, which can be modelled by fitting magnetization-temperature (MT) data. SQuID magnetometry was used to collect MT data. To obtain the saturation magnetization data shown in Figure 4, MH loops were collected at varying temperatures. The paramagnetic signal from the GGG was subtracted from the MH loop to obtain the saturation magnetization at a given temperature. Since YIG is a ferrimagnet with two magnetic sublattices (the irons at the *a* site and the irons at the *d* site), the magnetization is impacted by substitutions of nonmagnetic species. Such nonmagnetic species includes oxygen vacancies, yttrium atoms (as would be the case for cation mixing), and dopant atoms (such as the ruthenium used here). Substitution of a nonmagnetic species into one magnetic sublattice can induce spin canting in the opposing sublattice, which changes the coupling between sublattices.

The nonmagnetic substitution on the *a* site (k_a) and on the *d* site (k_d) can be quantified by fitting the MT data to a superexchange model for iron garnets. The model is modified from the Néel molecular field theory of ferrimagnetism, which uses three molecular field coefficients to describe the coupling between magnetic sublattices - a ferromagnetic coefficient for each sublattice (N_{aa} for the *d* site and N_{dd} for the *d* site), and then a third antiferromagnetic coefficient to describe the coupling between them ($N_{ad} = N_{da}$). By fitting this theory to several systems of substituted garnets, the following linear equations (equation (9)) were derived for the molecular field coefficients of YIG[84] and then converted into SI units[71]:

$$N_{dd} = -345.3(1-0.87\boldsymbol{k_a})$$

$$N_{aa} = -65.0(1-0.42\boldsymbol{k_d})$$

$$N_{ad} = N_{da} = 1101.7(1\text{-}0.25\boldsymbol{k_a}\text{-}0.38\boldsymbol{k_d}), \quad (9)$$

The magnetization of each of the sublattice ($M_a(T)$ for the *a* sublattice, $M_d(T)$ for the *d* site lattice) can then be described by equation (10):[71,84]

$$M_a(T) = n_a g_a \mu_B J B_J\left(\frac{\mu_0 m}{k_B T} \times (N_{da}M_d + N_{aa}M_a)\right)$$

$$M_d(T) = n_d g_d \mu_B J B_J\left(\frac{\mu_0 m}{k_B T} \times (N_{dd}M_d + N_{ad}M_a)\right), \quad (10)$$

where n_a and n_d is the volume density of Fe^{3+} on the *a* and *d* sublattices, respectively, g_a and g_d are the Landé g-factors, *J* is the total orbital angular momentum quantum number (= 5/2 for high spin iron), B_J is the Brillouin function, μ_0 is the permeability of free space, *m* is the mass of an electron, and k_B is the Boltzmann constant. By fitting these equations to MT data, the values of k_a and k_d can be extracted, resulting in the chemical formula $Y_3[Fe_{2*(1-ka)}(N)_{(2*ka)}][Fe_{3*(1-kd)}(N)_{(3*kd)}]O_{12}$, where N represents nonmagnetic species.

The results of fitting to this superexchange model using a least-squares fitting algorithm are shown in Table 3. The first observation is that the substitution on the *d* site sublattice fit to 0, which is not surprising considering the lower energy of formation for iron on the *d* site compared to on the *a* site.[71,122,123] Turning to substitution on the *a* site, substitution of nonmagnetic species was found to increase in the same observed order of increasing unstrained lattice constant (presented in Fig. 2, then reproduced in Table 3) and therefore the calculated magnetostriction. As mentioned previously, the substitution of nonmagnetic species can be the result of oxygen vacancies, yttrium atoms, or ruthenium dopant atoms. Since the stoichiometric addition of dopant is known here, that can be subtracted from the fitted value of k_a to give the contribution of

nonmagnetic substitution from oxygen vacancies and cation mixing (k_a - [Ru] in Table 3). The Y:Fe ratio can then be calculated assuming no vacancies with equation (11):

$$\text{Y:Fe ratio} = \frac{3+2k_a+3k_d}{5-2k_a-3k_d} \tag{11}$$

where the theoretical ratio of Y:Fe is 0.6 for the YIG's stoichiometry ($Y_3Fe_5O_{12}$). These values are recorded in Table 3 and can be compared to the expected Y:Fe ratio from ICP. Overall, both the ratios assuming no vacancies and the ICP ratios are a bit higher than theoretical, which indicates there is likely some amount of cation mixing.

Table 3. Calculated values for unstrained lattice constant reproduced from Fig. 2 (*a*), substitution of nonmagnetic species at the *d* and *a* site (k_d and k_a, respectively), substitution of nonmagnetic species from cation mixing and oxygen vacancies (k_a - [Ru]), the ratio of Y:Fe assuming no vacancies, and the expected ICP ratio of Y:Fe.

	***a* (Å)**	**k_d**	**k_a**	**k_a - [Ru]**	**Ratio of Y:Fe assuming no vacancies**	**ICP ratio of Y:Fe**
YIG(100)	12.368	0	0.04	0.04	0.63	0.616
YIG(111)	12.373	0	0.06	0.06	0.64	0.616
Ru:YIG(100)	12.376	0	0.11	0.07	0.67	0.622

Ru:YIG(111)	12.384	0	0.23	0.19	0.76	0.622

In addition to cation mixing, the modelled results suggest the films have some oxygen vacancies. The difference between the ratio assuming no vacancies and the ICP ratio is likely due to the presence of oxygen vacancies. The magnitude of this difference was found to increase with increasing out of plane lattice constant, with the highest for Ru:YIG(111).. This is to be expected, since it is known that oxygen vacancies add tensile strain.[82,83] We observe that, similarly to the trends in lattice constant, we see that the relative concentration of oxygen vacancies (and thus tensile strain) increases with both growth on GGG(111) (compared to GGG(100)) and with Ru-doping. It is known that YIG grows faster on GGG(111) than GGG(100) due to its more anisotropic surface.[73] As a result of the faster growth, oxygen vacancies are more likely to be kinetically trapped in the growth of YIG on GGG(111) than on GGG(100), which explains the larger tensile strain in films grown on GGG(111) than GGG(100). In addition to the substrate, Ru-doping was found to increase the relative concentration of oxygen vacancies. We hypothesize that Ru-doping causes more disorder in the structure, which may also kinetically trap more oxygen vacancies. We had expected the Ru:YIG films to have a larger lattice constant due to the larger lattice constant of bulk, single-crystal Ru:YIG (12.378 Å)[62] compared to bulk, single-crystal YIG (12.376 Å)[111], but we found that the magnitude of lattice constants reported in Fig. 2 were higher than this difference in literature values would suggest. The additional oxygen vacancies, which add tensile strain to YIG, are the likely cause for this deviation. Thus, we find that both deposition on the GGG(111), a more anisotropic substrate, and Ru-doping, increase oxygen vacancies, but the resulting tensile strain is only great enough with both together (in Ru:YIG(111)) to induce PMA. These results have broader implications in the design of spintronic materials, suggesting

that the oxygen concentration is of great importance to the magnetostriction and thus the magnetization of YIG materials.

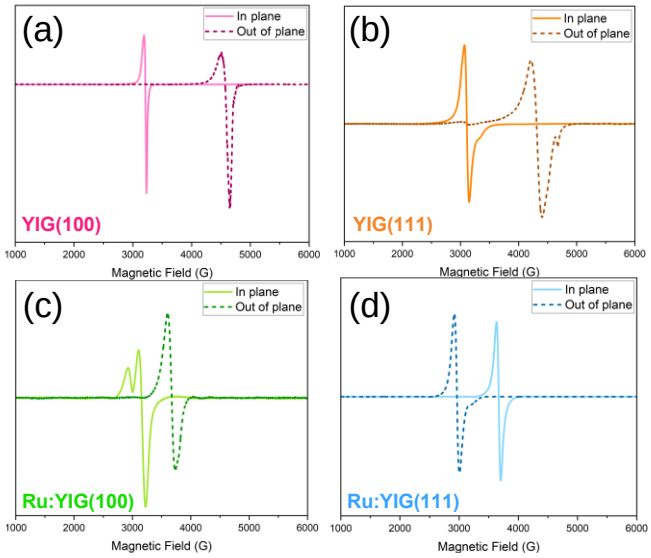

Figure 6-5. EPR collected with the magnetic field aligned in the plane of the film (solid line) and out of plane of the magnetic field (dashed line) for (a) undoped YIG(100), (b) undoped YIG(111), (c) Ru:YIG(100), and (d) Ru:YIG(111).

In addition to magnetostriction, magnetic loss is an important metric to evaluate the viability of these doped YIG films as spintronic materials, so we set out to study their dynamic magnetic properties. Electron paramagnetic spectroscopy (EPR) was used to observe ferromagnetic resonance (FMR). In this experiment, the sample is placed in a cavity tuned to X-band and an electromagnet is used to tune the magnetic field. The spectra for films were collected in the plane (aligned with) of the magnetic field and out of the plane (aligned perpendicularly to) of the magnetic field (Fig. 5). The broad, paramagnetic background from the GGG substrate was subtracted. Here, we were interested in two parameters - the resonance field and the linewidth. The

electromagnetic wave from the cavity causes the unpaired spins in the material to precess at a given magnetic field known as the resonance field. Since the resonance field depends on the magnetic anisotropy field, we can use its magnitude to characterize its magnetization.[124] The lifetime of the precession, which is the linewidth of the absorption peak, is a metric of magnetic loss. The values for both resonance field and linewidth for each spectrum can be found in Table 4.

The magnitudes of the resonance field for the four films follow the same trend observed in the magnetization data presented in Fig. 3. The in plane EPR spectra of YIG(100), YIG(111), and Ru:YIG(100) all resonate at a lower magnetic field than their respective out of plane spectra, indicating that the in plane anisotropy field is lower than the out of plane anisotropy field. In contrast, Ru:YIG(111), which exhibits PMA, has the opposite trend - its out of plane resonance field is lower than it is in plane, which is to be expected since it exhibits preferred magnetization in the out of plane direction. Thus, the trends in resonance field corroborate the trends in magnetization.

Table 4. Values for EPR resonance field and linewidth (both collected in the plane of applied magnetic field and out of the plane of the magnetic field) for the films studied in this work.

	In Plane Resonance Field (Oe)	**In Plane Linewidth (Oe)**	**Out of Plane Resonance Field (Oe)**	**Out of Plane Linewidth (Oe)**
YIG (100)	3230	23	4581	122

YIG (111)	3108	82	4284	156[a)]
Ru:YIG (100)	3176	89[a)]	3676	134
Ru:YIG (111)	3695	95	2946	98

[a)] Fit the additional mode separately and to obtain true linewidth for the main FMR mode, as described in the main text

In addition to the resonance field, we were interested in evaluating the magnetic loss of the films. The magnetic loss was obtained by integrating the absorbance spectrum in Fig. 5, then finding the full-width half-maximum (FWHM) of the resulting absorbance peak. It should be noted that we observed additional modes in addition to the main FMR resonances, which can be seen as less-intense peaks in the out of plane spectrum in YIG(111) and in the in plane spectrum for Ru:YIG(100). One possibility for the additional modes is that they are standing spin wave resonance modes, which are caused due to an inhomogeneous demagnetization field across the film.[22,125] Since the tails of these additional modes artificially broaden the linewidth of the main resonances, when evaluating the FWHM, these additional modes were fit to a separate peak and subtracted to obtain the linewidth of the main FMR resonance. This process was not required for the other spectra.

The films here were found to have quite low magnetic loss across the board, with the YIG(100) sample exhibiting a narrow linewidth of just 23 Oe. As mentioned previously, YIG is known to be a low-linewidth magnetic material, and the low value observed for this film confirms

its high crystal quality.[24,25,85] We will first discuss trends observed in the linewidth of undoped YIG. Overall, the linewidths found for YIG(111) were found to be a bit higher than films grown on YIG(100). To explain and characterize this difference, we deconvoluted the effects of intrinsic and extrinsic factors on the magnetic lifetime. Linewidth has two major contributions - the intrinsic magnetic loss, known as the Gilbert damping ($\boldsymbol{\alpha}$) and any sources of inhomogeneous line broadening (ΔH_0), such as magnon scattering off defects. We can separate these two contributions by collecting frequency-dependent absorption data, shown in Fig. 6. Here, instead of using an EPR tuned to a single cavity resonance, we use a stripline to tune the applied frequency while still sweeping the magnetic field. We first use the resonant magnetic field at each applied frequency to calculate the Gilbert damping by using the Kittel equation (equation (12)) to solve for the gyromagnetic ratio ($\boldsymbol{\gamma}$) of the undoped YIG films:

$$f=(\gamma/2\pi)\sqrt{H_r(H_r+4\pi M_s)} \tag{12}$$

where $\boldsymbol{f}$ is again the frequency, H_r is the resonant magnetic field, and M_s is the saturation magnetization of the film, obtained from the SQuID data discussed above.[126] Using the gyromagnetic ratio, we can then plot the linewidth as a function of applied frequency to separate out contributions to magnetic loss. The resulting plot is a straight line, where the inhomogeneous line broadening is the *y*-intercept and the Gilbert damping can be calculated from the slope using equation (13):[127–129]

$$\Delta H_{FWHM}=\Delta H_0+\alpha(4\pi/\sqrt{3}\gamma)f \tag{13}$$

The values for Gilbert damping and inhomogeneous line broadening are given in the bottom right corner of Fig. 6. Both the damping and the inhomogeneous line broadening for YIG(111) are larger than in films grown on YIG(100). The damping was found to be 1×10^{-3} and 1.9×10^{-3} for YIG(100) in comparison to YIG(111), respectively. Since damping is broadened by additional magnetic anisotropy, the damping is expected to be higher in YIG(111) in comparison to YIG(100) due to the additional magnetoelastic anisotropy. Similarly, the inhomogeneous line broadening was found to be 12 Oe and 50 Oe in YIG(100) in comparison to YIG(111), respectively. The faster growth on the more anisotropic surface likely results in more defects (including oxygen vacancies), which increases the inhomogeneous line broadening. This is corroborated by our previous discussion of more oxygen vacancies being present in films grown on GGG(111) rather than GGG(100).

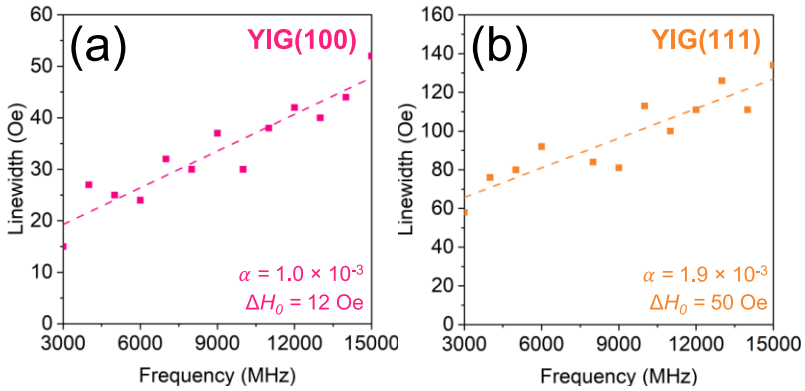

Figure 6-6. Frequency-dependent data for undoped YIG films grown on both (a) GGG(100) and (b) GGG(111). The Gilbert damping ($\boldsymbol{\alpha}$) and the inhomogeneous line broadening (ΔH_0) are recorded in the bottom right corner.

With the magnetic loss of the undoped YIG samples more fully understood, we then characterized the magnetic loss in the Ru-doped samples. In looking at both the in plane and out

of plane values for linewidth, Ru:YIG(100) exhibited a slightly larger linewidth than YIG(100). This is to be expected, as Ru-doping adds additional spin-orbit coupling that increases the Gilbert damping, as we have previously observed in polycrystalline Ru:YIG films. [62][39]

Interestingly, the linewidth of Ru:YIG(111) was found to be only slightly higher than YIG(111) in plane (95 vs. 82 Oe), and significantly *narrower* out of plane (98 vs. 156 Oe). This was surprising, as we had expected the additional oxygen vacancies and magnetoelastic anisotropy to broaden the linewidth of Ru:YIG(111) to be the largest of all the films studied. One potential explanation, proposed by Kittel, is that if the damping on a doped sublattice is much larger than on the other, undoped sublattice, that the Landau-Lifshitz model can be rewritten to describe the homogeneous linewidth of doped garnets as equation (14):

$$\Delta H/H \cong \gamma_A/\alpha_B M_A \tag{14}$$

where $\boldsymbol{\Delta H/H}$ is the homogenous linewidth, $\boldsymbol{\gamma_A}$ *i*s the gyromagnetic ratio of the undoped magnetic sublattice, $\boldsymbol{\alpha_B}$ is the damping of the dopant sublattice, and $\boldsymbol{M_A}$ is the saturation magnetization of the iron sublattice.[52,130] Thus, based on this Kittel model, if the magnetic damping at the dopant site greatly outweighs the damping of the other sublattice, magnetic loss is actually expected to *decrease*. We have previously observed this phenomenon in polycrystalline Ru:YIG films, but the overall linewidths are much lower in these single crystal films, confirming that the effect changes the intrinsic loss behavior.[39] The frequency-dependent data of undoped YIG indicates that the damping gets larger with growth on GGG(111) compared to GGG(100), and so it is possible that the damping from both the Ru-doping and the substrate pushes the total damping of one sublattice to be great enough to put it into the Kittel model regime. However, the additional damping from

the substrate or the additional damping from the doping alone is not large enough to do so; both factors in combination are necessary.

Therefore, this work demonstrates that there is a system where low magnetic loss and higher magnetostriction can be attained. Both Ru-doping and depositing on a more anisotropic substrate increase the magnetoelastic energy and magnetostriction, likely due to the increase in oxygen vacancies. This additional magnetostriction from both Ru-doping and the more anisotropic substrate outweighs the large shape anisotropy in YIG thin films, which allows it to exhibit PMA. Additionally, we have observed that YIG can be doped in a way where the damping also *decreases*. Both Ru-doping and depositing on a more anisotropic substrate likely increase the damping enough to allow it to fit a Kittel model for doped garnets where doping can lower the damping. Thus, YIG can be doped such that magnetic loss *decreases* while increasing magnetostriction in this regime, which is promising in the development of new spintronic materials.

3. Conclusion

In conclusion, we have successfully grown both undoped and Ru-doped epitaxial YIG films on GGG(100) and GGG(111) with a scalable, solution-based polymer-assisted deposition method. The films are of high quality and exhibit clear epitaxy off of the substrate. X-ray diffraction shows that the films were under increasingly large tensile strain moving from YIG(100), YIG(111), Ru:YIG(100), to finally Ru:YIG(111). Interestingly, using SQuID magnetometry, it was found that Ru:YIG(111) exhibited PMA, while YIG(100), YIG(111), and Ru:YIG(100) did not. In order to understand why the Ru:YIG(111) film exhibited PMA, the magnetic anisotropy energies were calculated from the SQuID magnetometry data. This revealed that both depositing on GGG(111) (an orientation with a more anisotropic face) and Ru-doping resulted in enough

magnetoelastic energy to overcome the large, dominating shape anisotropy in the YIG films. In order to understand this further, we fit magnetization-temperature data to Dionne's superexchange model to predict the relative amount of cation mixing and oxygen vacancies there are in the film. Both affected the films, but the predicted concentration of oxygen vacancies was found to increase in the same order as tensile strain. This is to be expected, given that oxygen vacancies induce tensile strain in YIG. The dynamic magnetic properties of YIG were also studied, where the resonance field, was found to track with the calculated values for magnetoelastic energy. Finally, magnetic loss was characterized to test the films' viability as a spintronic material. Depositing undoped YIG on GGG(111) vs GGG(100) was found to increase both the Gilbert damping, likely due to the additional magnetoelastic anisotropy, and the inhomogeneous line broadening, likely due to the additional oxygen vacancies. In doped YIG, Ru(100) had a broader linewidth than YIG(100), likely due to the additional spin-orbit coupling from the dopant. Moreover, the Ru:YIG(111) film actually had *lower* magnetic loss, as predicted by Kittel. We expect that both depositing on the more anisotropic substrate and Ru-doping increase the damping enough to bring it into the bounds of the Kittel model. Thus, a high magnetostriction, low magnetic loss material can be achieved by carefully tuning the dopant and substrate, which has potential for the development of new spintronic materials. Thus, a high magnetostriction, low magnetic loss material can be achieved by carefully tuning the dopant and substrate, which has great potential for the development of new spintronic materials.

4. Methods

A. Polymer-assisted Deposition of the Films

A modified version of a previously-published method was used for the polymer-assisted deposition of films in this work.[99] $Y(NO_3)_3 \cdot 6H_2O$, (99.9%, ACROS Organics), $Fe(NO_3)_3 \cdot 9H_2O$ (99+%, ACROS Organics), $RuCl_3 \cdot xH_2O$, (35-40% Ru, ACROS Organics), ethylenediaminetetraacetic acid (EDTA) (98+%, TCI Chemicals), and polyethlenimine (PEI) (branched, M_w = 25000, M_n = 10000, Sigma Aldrich) were used without further purification. Solutions of Y, Fe, and Ru were prepared separately. Each metal salt solution contained a 1:1 mole ratio of metal salt:EDTA and a 1:1 mass ratio of EDTA:PEI. For example, for a typical iron solution, 10 mmol (4.040 g) of $Fe(NO_3)_3 \cdot 9H_2O$ was mixed with Millipore filtered water, followed by 10 mmol (2.922 g) of EDTA, and then finally 1.42 mL (2.922 g) of PEI. The order of reagent addition is important here - the salt should be added to the water first to dissolve, then the EDTA to form a metal-EDTA complex, then the PEI to allow the metal-EDTA complexes to chelate to the polymer. Each solution was concentrated to approximately 0.3 M by ultrafiltration (Vivaspin 100 Pressure Concentrators) using a 10 kDa filter. The retained portions were kept. The individual solutions were then mixed to achieve the desired stoichiometry and concentrated again to approximately 0.5 M. This solution was then diluted with ethanol to a final concentration of 0.2 M. The same undoped solution was used for YIG on GGG(100) as YIG on GGG(111) and the same doped solution (with a stoichiometric ratio of $Y_3Fe_{4.955}Ru_{0.045}O_{12}$) was used for Ru:YIG on GGG(100) as on Ru:YIG on GGG(111).

Approximately 200 μL of the solution was spincoated onto 1 x 1 cm^2 GGG substrates at 4000 rpm for 30 s with the fastest possible ramp speed. Deposition was performed in a cleanroom to prevent dust contamination. The GGG(100) was purchased from MTI Inc. and the GGG(111) was purchased from Egorov Scientific. Once deposited, films were quickly placed in a tube furnace to be annealed in air. The films were heated to 900 °C with an 8-hour ramp, an 8 hour soak, and

finally an 8 hour cool to room temperature in order to crystallize without the formation of cracks. Films prepared this way were all approximately 20 nm thick (± 5 nm between films) as measured by profilometry.

B. Instrumental Details

Scanning/transmission electron microscopy (S/TEM) imaging and STEM-EDS was performed using a FEI Titan scanning transmission electron microscope operated at an accelerating voltage of 300 kV. This instrument is equipped with Oxford X-MaxTEM 100 N TLE Windowless silicon drift detector (SDD) 100 mm 2 EDS and a Gatan Ultrascan 2 K × 2 K charge-coupled device (CCD) camera. STEM-EDS was performed and analyzed using Aztec software. To prepare S/TEM samples, films were milled into a lamella using a focused ion beam (Nova 600 SEM/FIB System) using a 10 keV beam for a final thinning layer to prevent surface amorphization.

Inductively-coupled plasma optical emission spectroscopy (ICP-OES) was performed on an Agilent 5110 ICP-OES (inductively coupled plasma-optical emission spectrometer). Single-element yttrium (RICCA Chemical Company, 1000 ppm Y in 3% HNO_3), iron (RICCA Chemical Company, 1000 ppm Fe in 3% HNO_3), and ruthenium (CPI international Peak Performance Inorganic Trace Metal Standard, 1000 mg/mL Ru in 10% HCl) standards were used with a lutetium internal standard (RICCA Chemical Company, 1000 ppm Lu in 3% HNO_3). A calibration curve was generated for each standard before the samples were run.

XPS was performed on a Kratos Axis Ultra DLD spectrometer with a monochromatic Al Kα radiation source. A charge neutralizer filament was used to prevent the charging of all YIG and Ru-doped YIG films. All spectra were calibrated using the adventitious Carbon 1s peak. All peak fitting and analysis was performed on CASA XPS Software using the CASA XPS Library. The Y 3d spitting is set to 2.05 eV, while the Fe 2p splitting is set to 13.1 eV.

XRD and XRR were performed on a triple-axis high-resolution diffractometer Bruker-JV D1 equipped with incident beam conditioning including a Maxflux™ focusing graded Göbel mirror[131], a two bounce Si 220 channel-cut collimator crystal, and a dual channel (two or four bounce) Si 220 analyzer crystal, using Cu $K\alpha_1$ radiation (λ =0.15406 nm) from a sealed x-ray tube culminating in an acceptance angle of 10 arcseconds. XRR measurements were taken and fitted to determine layer thickness, density, and roughness using a differential evolution genetic algorithm approach[132], while XRD ω:2θ measurements of the (444) and (888) symmetric reflections were taken to measure the lattice parameter. Diffraction patterns were compared to JCPDS reference cards #00-043-0507 (for YIG) and #00-013-0493 (for GGG) using X'Pert Highscore Plus 2.0.1.

Static magnetic properties were measured at room temperature using a Quantum Design MPMS3 superconducting quantum interference device (SQuID) magnetometer equipped with an oven attachment. In collecting the MH loops, it is important across a field range that is high enough to saturate the YIG films, but low enough to reduce magnetization from the GGG paramagnetic background. We found that 250 Oe - 500 Oe loops were best for the direction of preferred anisotropy (in-plane for both undoped YIG samples and Ru:YIG(100), out-of-plane for Ru:YIG(111)) and that 750 Oe - 2000 Oe loops were best for the orthogonal direction. The GGG paramagnetic signal was then subtracted to obtain an MH loop for the film.

Electron paramagnetic resonance (EPR) with an X-band cavity to study dynamic magnetic properties in all samples studied in this work (Bruker EMXplus). Frequency-dependent dynamic data for undoped YIG on (001)GGG was measured using a previously-described stripline ferromagnetic resonance (FMR) set up.[133,134] Briefly, a short-circuited stripline is connected to a vector network analyzer (VNA). The sample is placed under the stripline (in plane) as the VNA is used to tune frequency and an electromagnet is used to tune the magnetic field applied parallel to

the sample. The reflection coefficient was measured as a function of both the biasing magnetic field and the frequency. This measurement was performed at 300 K. Ferromagnetic resonance (FMR) response on GGG(111) was collected using a broadband coplanar waveguide with a flipped-chip configuration installed in a physical property measurement system with a He cooling capability. Magnetic field sweep FMR measurements yielded a differential absorption spectrum at each frequency (f) and here we focused on the derivative peak corresponding to the main resonance uniform mode. The frequency used in the FMR measurement varied from 3 GHz to 12 GHz, and the measurement was performed at 300 K. All measurements were performed for an in-plane magnetic field configuration.

Acknowledgements

The authors of this work would like to thank Professor Greg Carman and Dr. Emily Burnside for helpful discussion and assistance with FMR measurements. This work was supported by the NSF Nanosystems Engineering Research Center for Translational Applications of Nanoscale Multiferroic Systems (TANMS) under Cooperative Agreement Award No. EEC-1160504. Additionally, authors S.K.P and D.D.R. acknowledge support from the National Science Foundation Graduate Research Fellowship under Grant No. DGE-1650604 and DGE-2034835. This work utilized the California NanoSystems Institute (CNSI) at the University of California, Los Angeles, specifically the Electron Imaging Center for Nanomachines (EICN) and the Nanofabrication Laboratory (Nanolab). This work also utilized the UCLA Nanoelectronics Research Facility (NRF) and the UCLA Molecular Instrumentation Center (MIC). This work made use of a Bruker EMXplus purchased with the support of NSF-MRI award 2117480.

APPENDIX A

Supporting Information for Chapter 3:

Increased Magnetoelectric Coupling in Porous Nanocomposites of $CoFe_2O_4$ and $BiFeO_3$ with Residual Porosity for Switchable Magnetic Devices

Shreya K. Patel,† C. Ty Karaba,† Daniel D. Robertson, Jeffrey Chang, Kevin Fitzell, Charlene Z. Salamat, Jane P. Chang, Sarah H. Tolbert

†These authors contributed equally to this work.

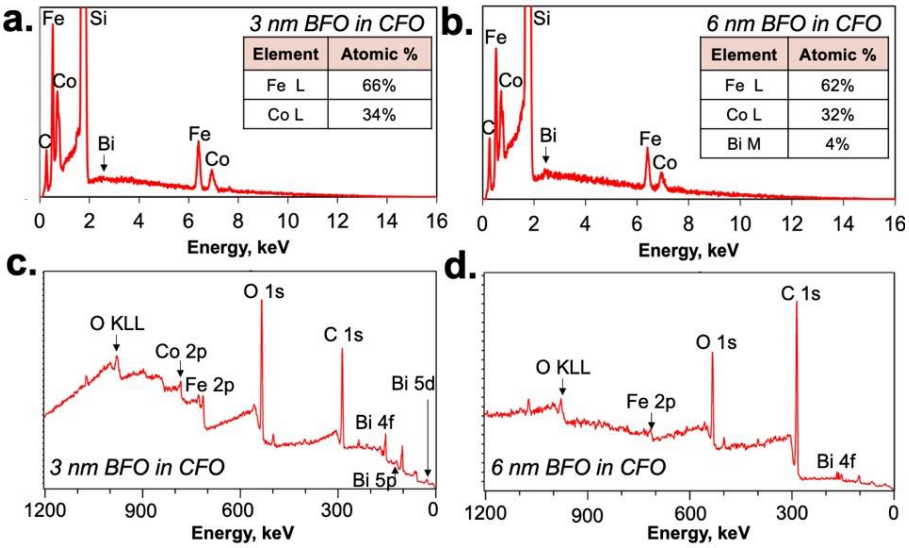

Figure A-S1. SEM-EDS [(a) + (b)] and XPS [(c) + (d)] measurements on the 3 nm-BFO [(a) + (c)] and the 6 nm-thick BFO composites [(b) + (d)]. SEM-EDS shows that cobalt and iron are in the atomic ratios expected for CFO, and that Bi is present in both samples. Given the relatively small volume of Bi and the intrinsic low intensity of the Bi peaks, we were not able to quantify the Bi:Co ratios in the 3 nm sample. XPS data from the composites confirm the presence of bismuth and iron from BFO in both the 3 nm and 6 nm samples. Co is not observed in XPS data collected on samples with a 6 nm BFO layer due to the low penetration depth of XPS.

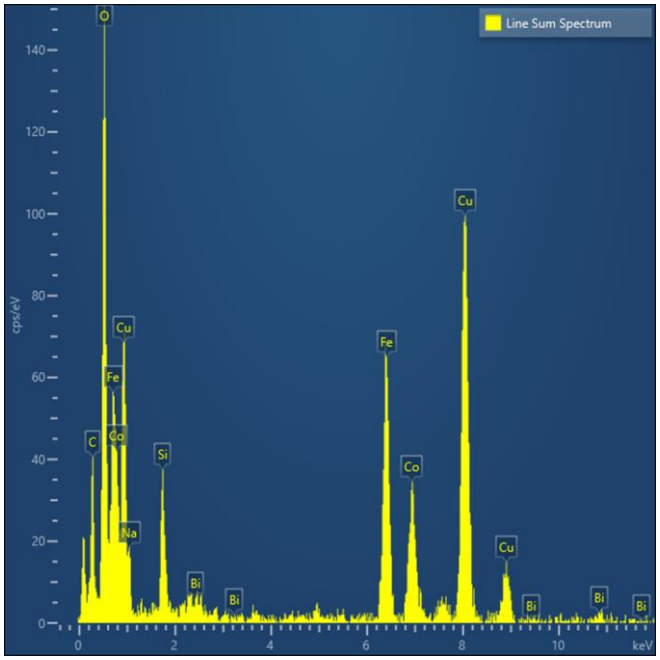

Figure A-S2. Representative STEM-EDS spectrum of the 6 nm BFO in CFO composite.

Discussion of Microstrain in the Nanoporous CFO and in the Composite

We begin with discussion of the initial *macro*strain (from uniform lattice distortion, which result in X-ray diffraction peak shifts) and *micro*strain (from inhomogeneous sources of strain, including dislocations, vacancies, and grain boundaries, which result in X-ray diffraction peak broadening) in the nanoporous CFO alone. We compared the in-plane and out-of-plane diffraction peaks from GIWAXS patterns (collected with rocking scans to obtain true out-of-plane data) with the JCPDS values and found that the films were under tensile strain in-plane, and compressive strain out-of-plane (Fig. S3). This strain state arises from the thermal expansion coefficient mismatch between the substrate (silicon) and the film (CFO). Silicon has a much lower thermal expansion coefficient (3.5×10^{-6} K^{-1}) than CFO (1.0×10^{-5} K^{-1}), and so it contracts less than the CFO film upon cooling the after annealing.[303,304] The CFO film is clamped in the in-plane direction, so the films should be under in-plane tensile stress, and out-of-plane compressive stress.

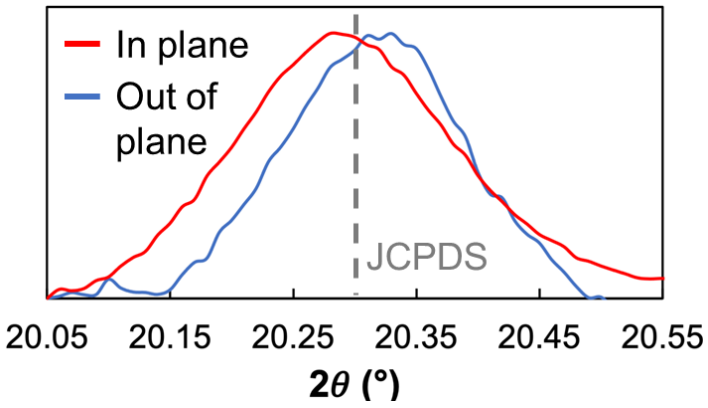

Figure A-S3. The CFO(311) X-ray diffraction peak for porous CFO at an X-ray energy = 0.98 Å, showing in-plane tension and out-of-plane compression from thermal strain.

We next consider both macro- and microstrain in the CFO-BFO composite structures. Globally, the CFO peaks in the composite films were found to all be under similar in-plane tension and out-of-plane compression (Fig. S4), likely due to the thermal strains discussed above.

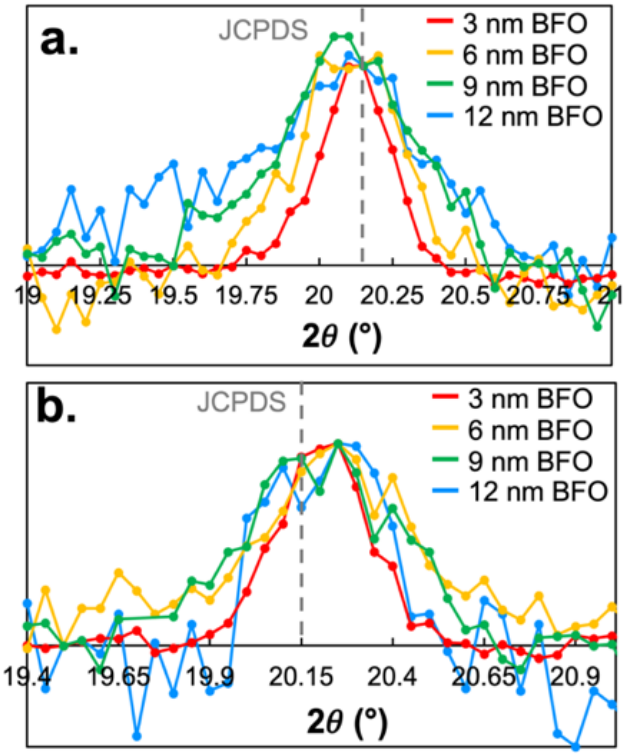

Figure A-S4. The CFO(311) X-ray diffraction (a) in-plane and (b) out-of-plane peak in the composites at an X-ray energy = 0.88 Å.

Interestingly, the CFO peaks were also found to exhibit a large degree of broadening with increased BFO layer thickness. We used Williamson-Hall plots for GIWAXS patterns to investigate if the broadening with increased BFO layer thickness and determine if it was due to a difference in grain size (i.e. differences in Scherrer width), or if it was due to an increase in microstrain (Fig. S5). The slope of the Williamson-Hall plot is proportional to the broadening from strain, while the y-intercept is inversely proportional to the broadening from grain size. All y-intercept values of the Williamson-Hall plots across the sets of samples were approximately the same, indicating that size effects did not dominate. We did, however, observe a monotonic increase in the slope of the Williamson-Hall plots with BFO layer thickness, leading us to believe that increased BFO layer thickness increases the overall microstrain of the nanoporous CFO. While the diffraction intensity of the BFO peaks in the 3 nm, 6 nm, and 9 nm thick samples were too low in intensity to be seen with X-ray diffraction, we expect that since CFO is strain-coupled to BFO through covalent bonding, we believe that BFO is also under increasingly large microstrain as a function of BFO layer thickness. This is interesting, as we would expect the thinner BFO layers to be under the most microstrain since ultrathin films are known to usually be dominated by strain from large surface energy.[130,305–307] The additional strain is therefore believed to be the result of additional, growth-related crystallization strains as the BFO layer gets thicker, which is larger than the interfacial strain.

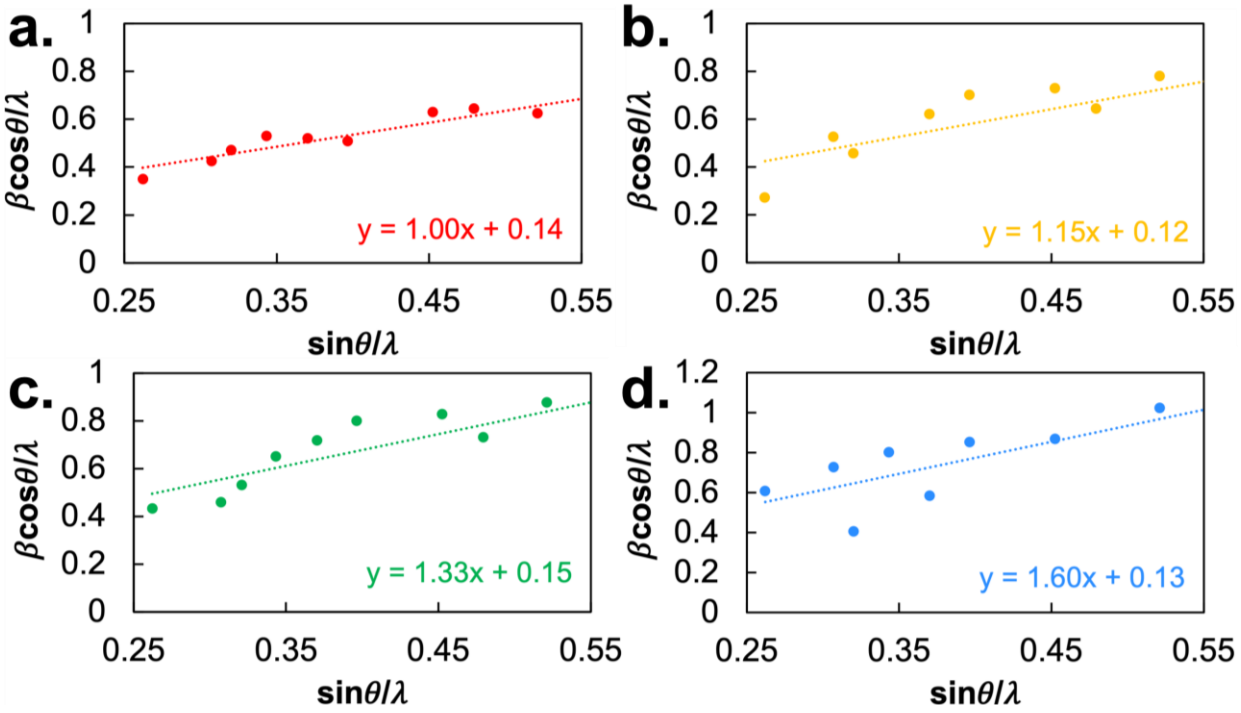

Figure A-S5. Williamson-Hall plots for CFO in the GIWAXS patterns of composites.

We should note that these observations of changes in the initial microstrain state do not contradict the larger conclusions of this manuscript. Both magnetoelectric and strain measurements show out-of-plane tensile strain, which may be facilitated by the initial out-of-plane compressive strain state. The microstrain is inhomogeneous, and so will not contribute to magnetic alignment.

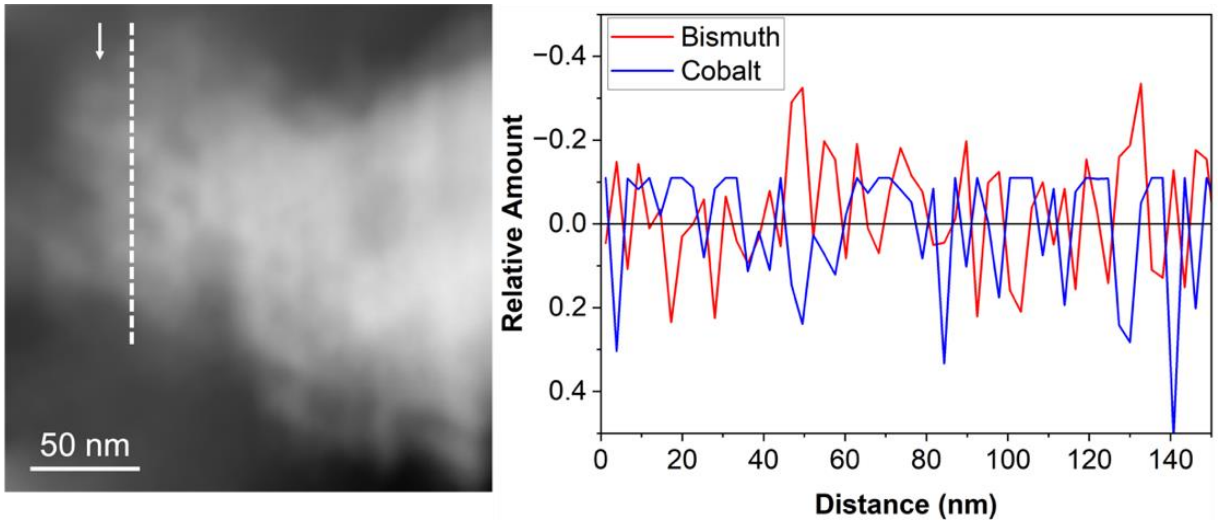

Figure A-S6. Quantitative STEM-EDS line scan mapping of Bi and Co for the 6 nm BFO in CFO composite. The position of the line is shown on the left, with the elemental data presented on the right. Clear anti-correlation of the Bi and Co intensities is observed.

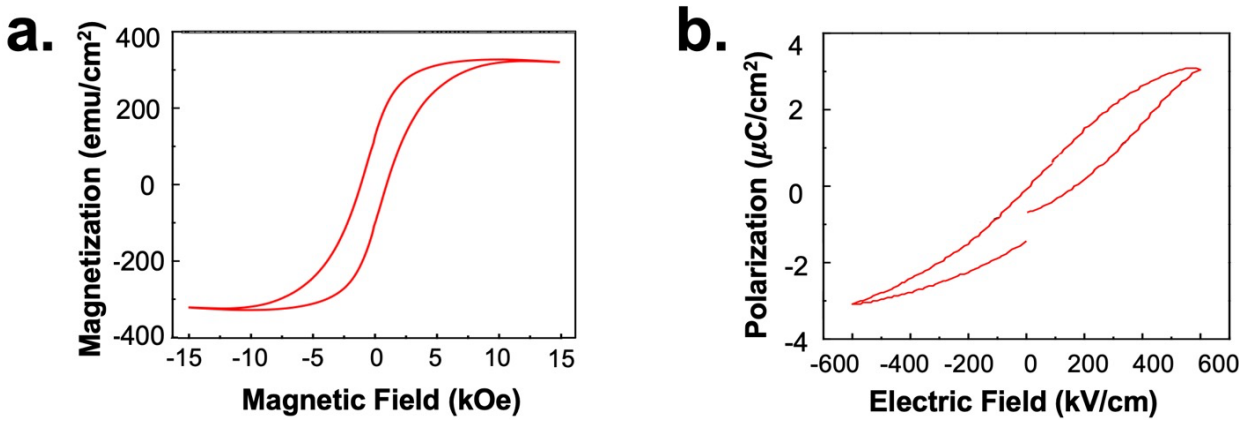

Figure A-S7. Hysteretic loops for CFO and BFO components of the nanocomposites, including (a) MH loop for porous CFO and (b) PE loop for thick film of ALD BFO (b), demonstrating acceptable magnetic and piezoelectric properties.

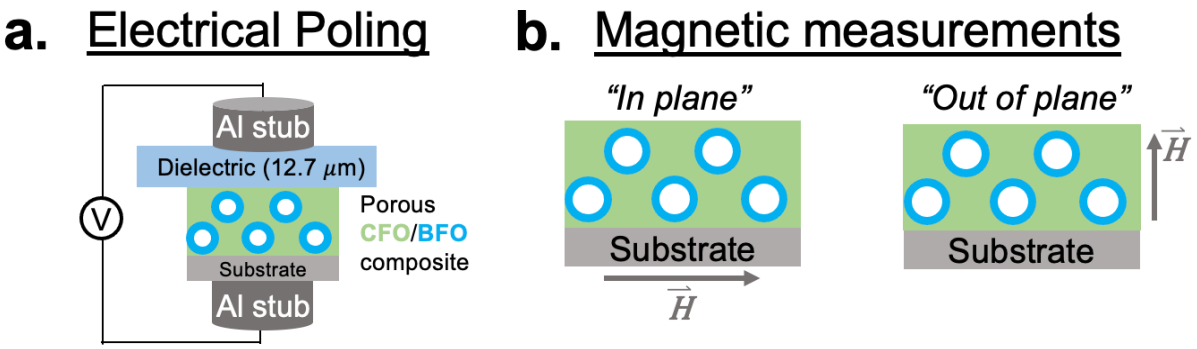

Figure A-S8. Schematic of (a) *ex situ* electrical poling and (b) "in plane" versus "out of plane" magnetic measurements.

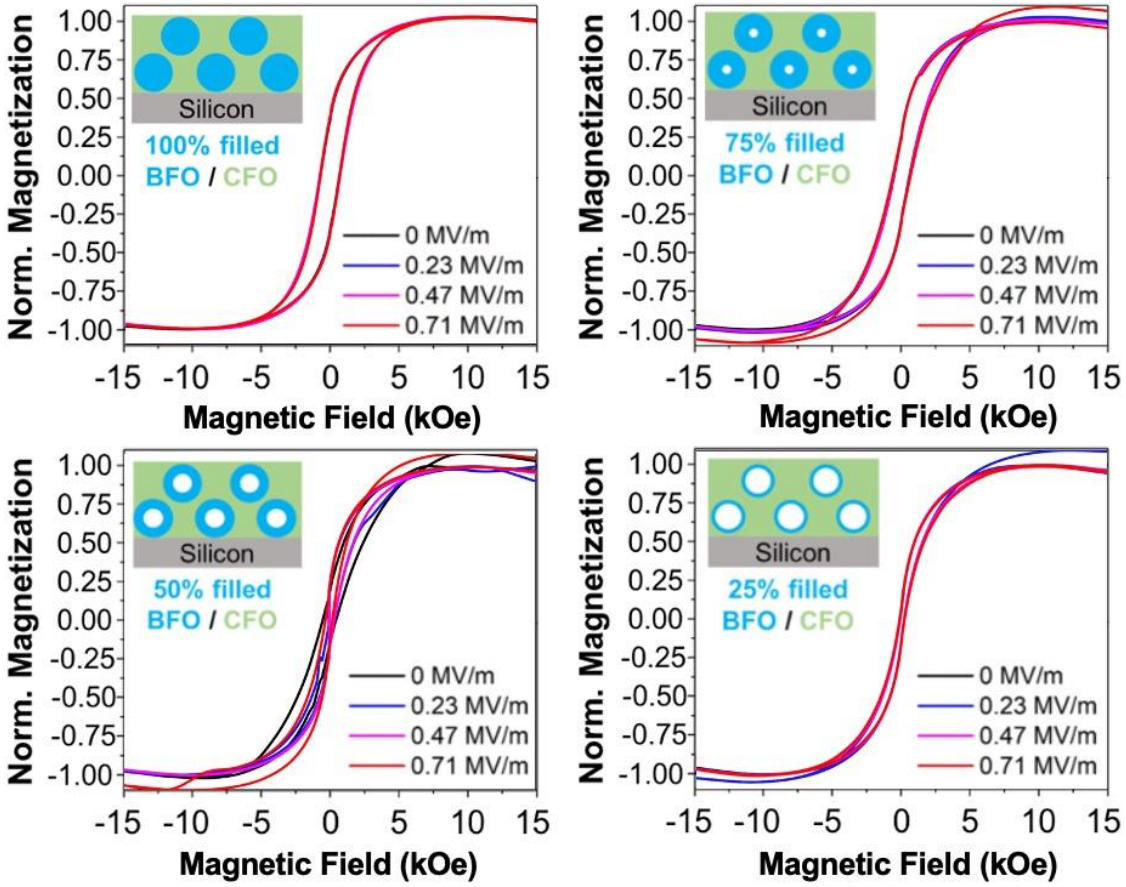

Figure A-S9. In plane SQuID magnetometry measurements for the 25%, 50%, 75%, and 100% filled nanocomposites, electrically poled from 0 to 0.71 MV/m. Magnetization in plane does not change, likely due to substrate clamping.

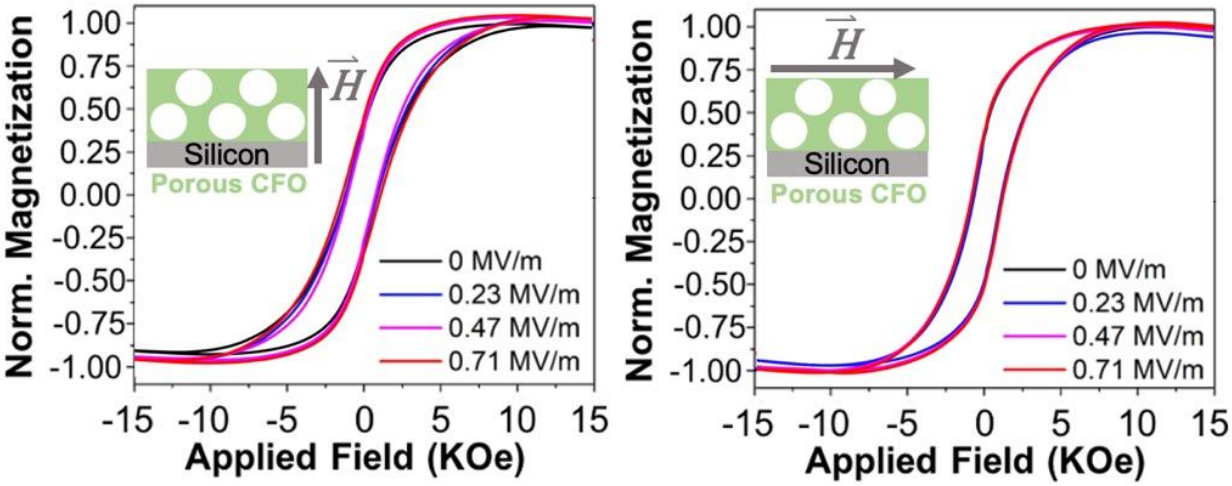

Figure A-S10. SQuID magnetometry on bare, porous CFO poled in situ from 0 to 0.71 MV/m. Measurements were taken out of plane from the magnetic field (left) and in the plane of the magnetic field (right). No large changes in magnetization was observed.

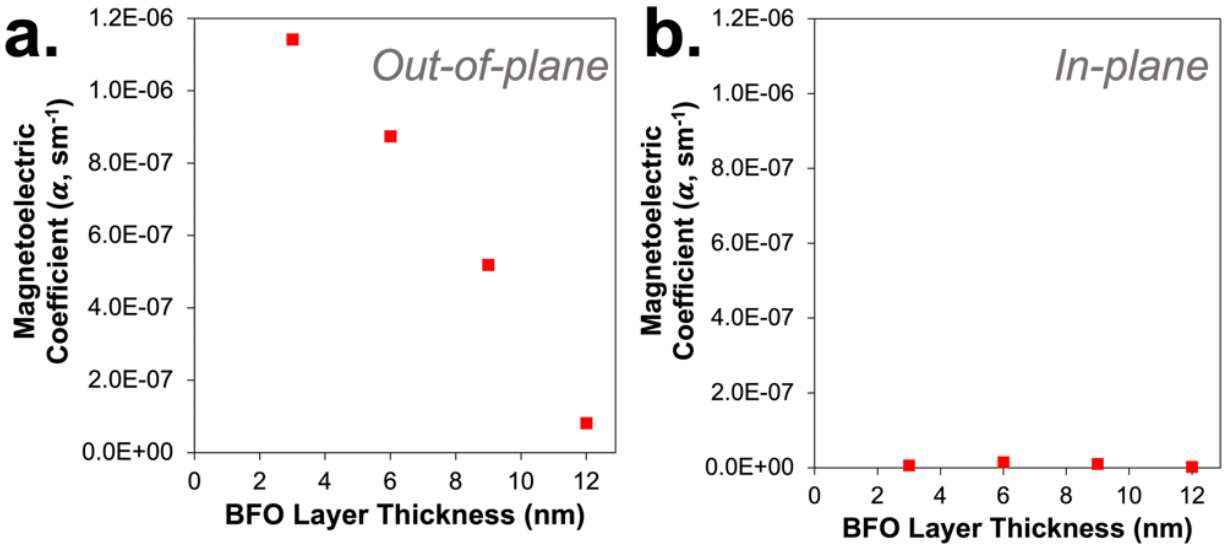

Figure A-S11. Comparison of out-of-plane magnetoelectric coefficient (a) vs. the in-plane magnetoelectric coefficient (b).

APPENDIX B

Supporting Information for Chapter 4: *In-situ* Measurement of Magnetoelectric Coupling and Strain Transfer in Multiferroic Nanocomposites of $CoFe_2O_4$ and $Hz_{0.5}Zr_{0.5}O_2$ with Residual Porosity

Shreya K. Patel,[1] Daniel D. Robertson,[1] Suraj S. Cheema,[2] Sayeef Salahuddin,[2,3] Sarah H. Tolbert[1,4,5,*]

Synthesis of CFO-HZO composite

The synthesis of the porous CFO template[28] and ALD deposition of HZO[131] have both been reported previously. Porous CFO was made using a sol-gel process. To synthesize CFO, stoichiometric amounts of $Fe(NO_3)_3 \cdot 9H_2O$ (0.31 g) and $Co(NO_3)_2$ $6H_2O$ (0.11 g) were dissolved in 1 mL of 2-methoxyethanol, 1 mL of ethanol, and 20 μL of glacial acetic acid. The solution was allowed to stir for several hours (and can be stirred overnight if needed) until homogenous. The CFO solution was then templated to be made porous using a micelle-forming block co-polymer. First, a templating solution containing 40.0 mg of poly((butadiene)(5500)-*block*-poly-(ethylene oxide)(7500)) (Polymer Source Inc, #P2952_BdEO) in 1 mL of ethanol was allowed to dissolve while magnetically stirring on a temperature-controlled hot plate set to 60 °C. Once fully dissolved, the templating solution was added to the CFO sol, which was stirred until it was homogenous. Films were then dip-coated at a withdrawal rate of 30 cm/min onto platinized silicon (Pt (100 nm)/Ti (5 nm)/SiO_2 (about a micron) on high conductivity silicon) at a humidity of 10-30 %. Films were calcined in air at 80 °C for 6 hours, at 130 °C for 8 hours, and at 180 °C for 6 hours. Once calcined, films were crystallized through annealing overnight (14 hours) at 550 °C with a 10 °C/min ramp and then cooled to room temperature at 10 °C/min.

For ALD HZO, metal alkoxide precursors tetrakis(ethylmethylamino)hafnium and tetrakis(ethylmethylamino)zirconium were oxidized with water (Fiji Ultratech/Cambridge Nanotech tool). Thin films were grown at 250 °C.

Details of CFO-HZO composite characterization methods

The pore symmetry and thickness of the nanocomposites was confirmed using a JEOL JSM-6700F field-emission scanning electron microscopy (FE-SEM). EDS was collected using the same FE-SEM as used to characterize the morphology using an accelerating voltage of 3 keV. TEAM software was used for the EDS measurements. Scanning/transmission electron microscopy (S/TEM) imaging and STEM-EDS was performed using a FEI Titan scanning transmission electron microscope operated at an accelerating voltage of 300 kV. This instrument is equipped with Oxford X-MaxTEM 100 N TLE Windowless silicon drift detector (SDD) 100 mm 2 EDS and a Gatan Ultrascan 2 K × 2 K charge-coupled device (CCD) camera. STEM-EDS was performed and analyzed using Aztec software. To prepare S/TEM samples, films were detached from the substrate with a razor blade, suspended in ethanol, and drop-cast onto copper grids for analysis. All magnetometry experiments reported here were performed on a Quantum Design MPMS 3 Superconducting quantum interference device (SQuID) magnetometer. The magnetic moment of the entire composite normalized to the magnetic moment of the unpoled composite, since the same film was used for each of the MH loops shown, and thus the volume of magnetic material is exactly the same for each MH loop. Thus, we are effectively normalizing by the number of spins, so the volume that those spins occupy does not need to be defined. Grazing incidence wide angle scattering (GIWAXS) was collected at Stanford Synchrotron Radiation Laboratory (SSRL) using

beamline 17-2 at wavelengths λ = 0.886 Å and compared to JCPDS reference card #00-001-1121 (for CFO) using X'Pert Highscore Plus 2.0.1.

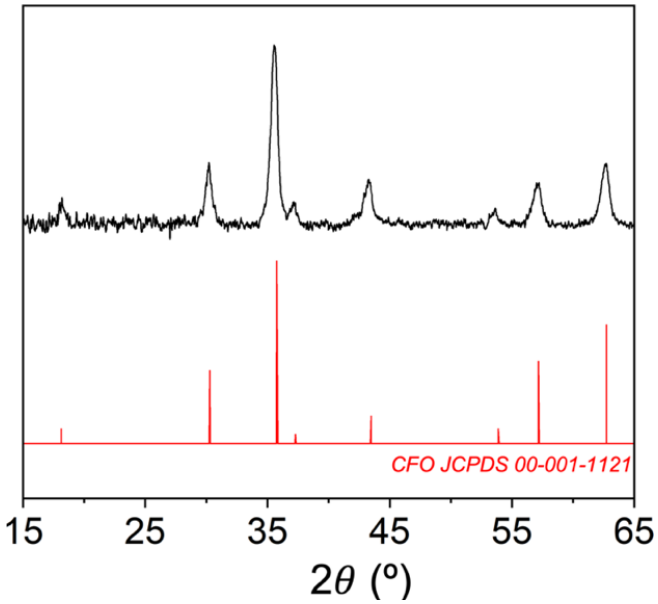

Figure B-S1. GIWAXS of porous CFO on silicon after annealing, demonstrating the expected spinel crystal structure.

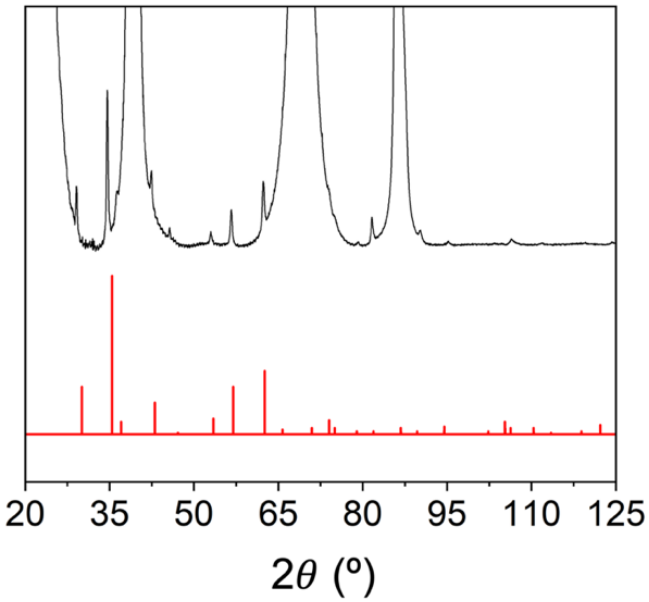

Figure S2. GIWAXS of the total composite after HZO deposition. Peaks marked with asterisks (*) stem from the platinum back electrode. While it is possible that the very broad peak at approximately 54 could be assigned to HZO, the other expected HZO peaks either overlapped with platinum peaks or were too weak in intensity to be seen in diffraction due to the small volume in the material (only 3 nm film thickness).

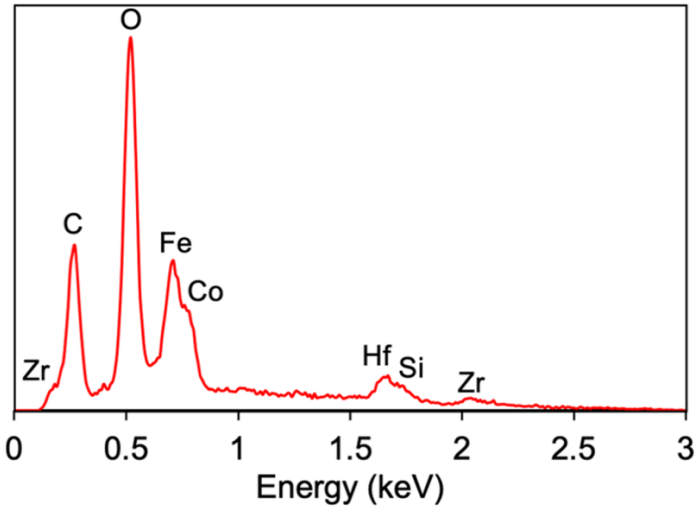

Figure B-S3. EDS of total composite, with element assignments above their corresponding peaks.

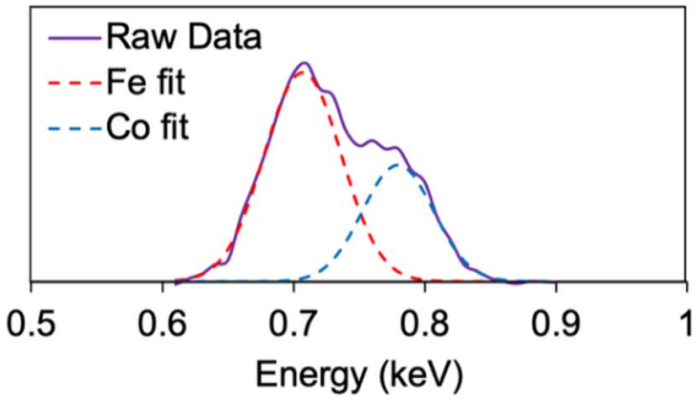

Element	Atomic %	Error %
Fe L	66%	±3%
Co L	34%	±4%

Figure S4. EDS fitting of Fe L edge and Co L edge peaks. Atomic ratio shows that the ratio of Co:Fe is approximately 1:2 with narrow error bars, which is to be expected for CFO ($CoFe_2O_4$).

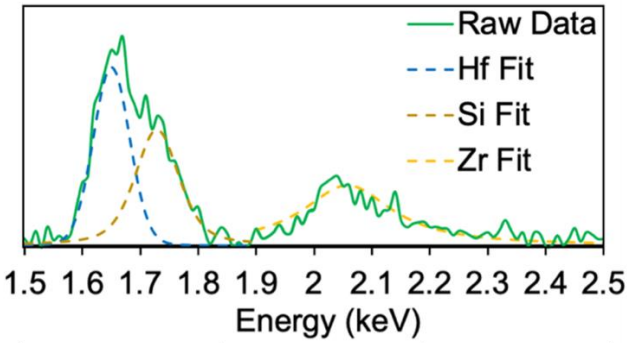

Element	Atomic %	Error %
Hf M	52%	±3%
Zr L	48%	±5%

Figure B-S5. EDS fitting of Hf M edge and Zr L edge peaks. Atomic ratio shows that the ratio of Hf:Zr is approximately 1:1 with relatively narrow error bars, which is to be expected for HZO ($Hf_{0.5}Zr_{0.5}O_2$).

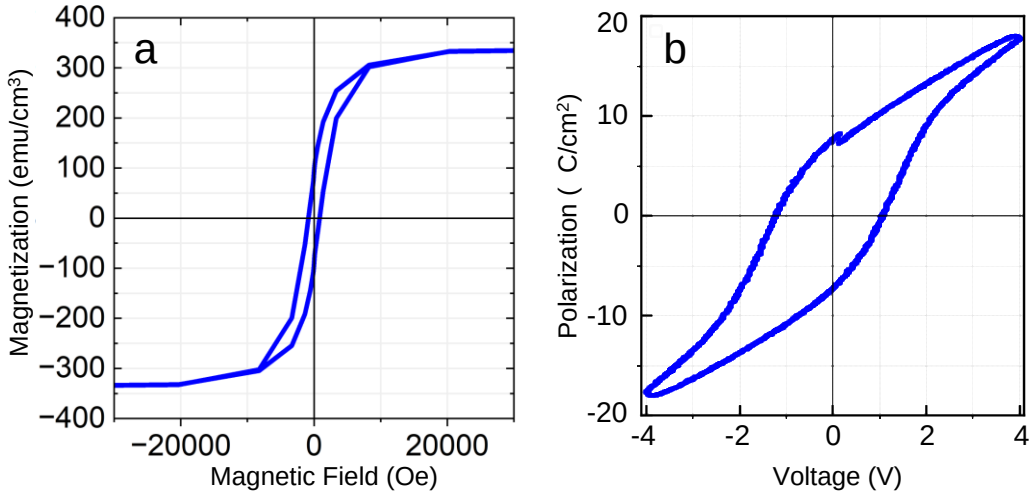

Figure B-S6. a) Out-of-plane M-H loop of porous, unfilled CFO and **b**) P-E loop of 5 nm thick ALD deposited HZO. The CFO is ferromagnetic with a saturation magnetization of 340 emu/cc and a coercivity of approximately 800 Oe. The HZO is ferroelectric with a coercive field of ~1 V.

Details of *in-situ* electrical poling during magnetic measurements

Sample preparation: Composites were first cut down to 6 mm x 6 mm pieces, which fit snugly in the straw sample holders used for the Quantum Design MPMS 3. Since composites were porous, using gas phase deposition methods to deposit a blanket top electrode was not possible, as the metal ions would infiltrate the pore structure and short the composite. Instead, here, a piece of 5 mm x 5 mm high-purity Al foil (99.9995% metal basis, 0.13 mm thick) was placed on top of the SQuID-sized sample and used as the top electrode. It is important to note here that due to the high sensitivity of a SQuID magnetometer, small volumes of metal impurities can add additional ferromagnetic signal. In fact, even carbon tape and copper tape were found to have significant ferromagnetic signal, so it is important to utilize high purity metal components. A small piece of glass was epoxied on to add stack pressure. Alternatively, silver paste with micron-sized particles can be used as a top electrode, however silver paste exhibits a small, ferromagnetic signal, < 5% of the signal seen in CFO composite thin films (depending on the volume used). From here, an approximately 5 cm long silver wire (32 AWG, Alpha Wire, product number 1850 WH005) was soldered onto the top electrode with indium solder (Chip Quik, Inc., product number SMDIN100). A ground wire was soldered onto the back of the sample. Gold pin connectors (28-32 AWG, Amphenol ICC, product number 75967-111LF) were crimped onto both the wires, then the crimps were wrapped with Kapton tape to prevent shorting. Once prepped, the samples can be mounted into a straw as normal.

Integration to MPMS 3: The oven attachment of the MPMS 3 was adapted to allow for *in-situ* electrical poling. A D-sub cable (Phoenix Contact, product number 1656262) was connected to a coaxial cable and into a power supply. The male end of the D-sub cable can be connected into the Quantum Design oven attachment probe, which is made for the wired access port. To connect the

sample to the oven attachment rod, a special circular connector was made. Individual circular connectors that fit into the oven attachment rod can be purchased from Quantum Design (5 pin-male circular connector). Wire was soldered from the 5-pin circular connector, which were soldered into D-sub socket connecters (28-32 AWG). These bottom connectors were epoxied in place. The samples can be plugged directly into this makeshift connector and then to the Quantum Design oven attachment rod. While running MPMS 3 programs, it is best to use DC mode to avoid adding strain to the wires.

Figure B-S7. Image showing *in-situ* electrical poling using the electrical connections for the MPMS 3 oven attachment.

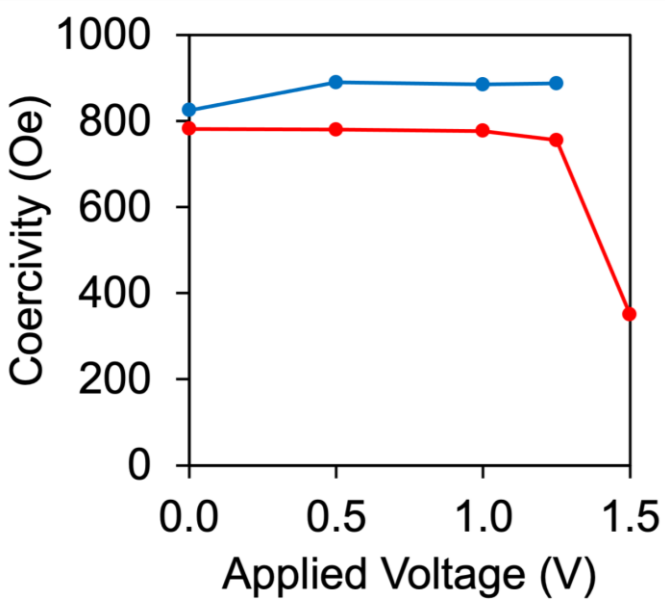

Figure B-S8. In-plane (red) and out-of-plane (blue) changes in coercivity, echoing trends in saturation magnetization observed in Figures 2 and 3.

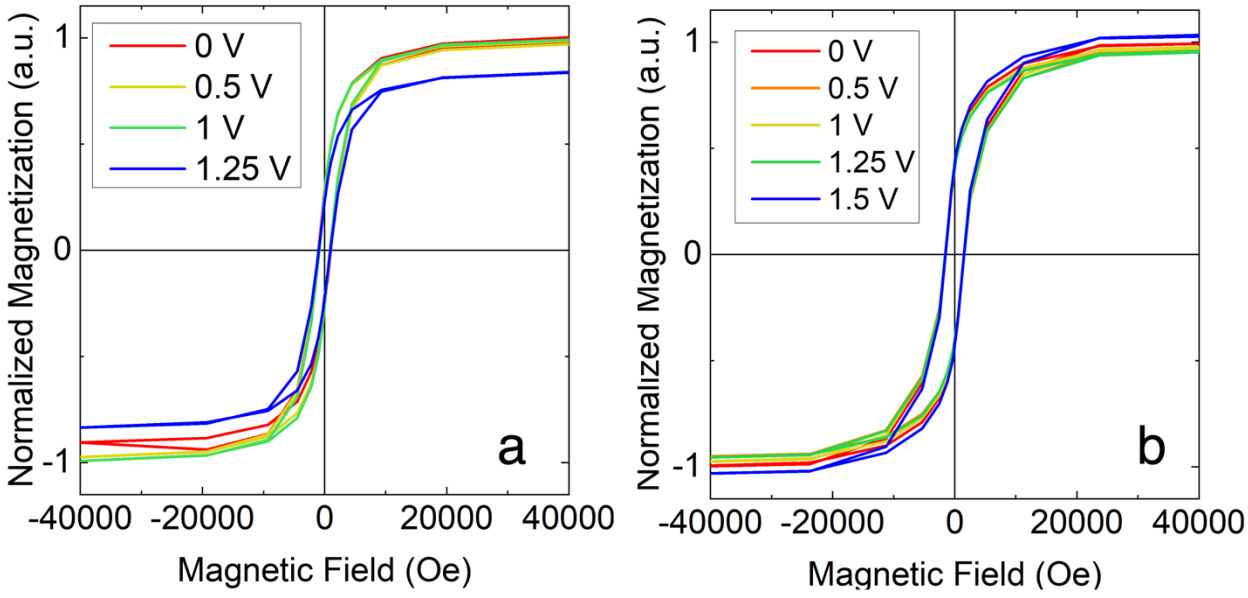

Figure B-S9. *Ex situ* poled composite magnetometry experiments with the magnetic field **a**) out-of-plane with respect to the sample and **b**) in-plane with respect to the sample. The magnetization changes are smaller than observed with *in-situ* poling described in the main text, since *ex situ* poled composites are at remnant strain states, not saturation strain states.

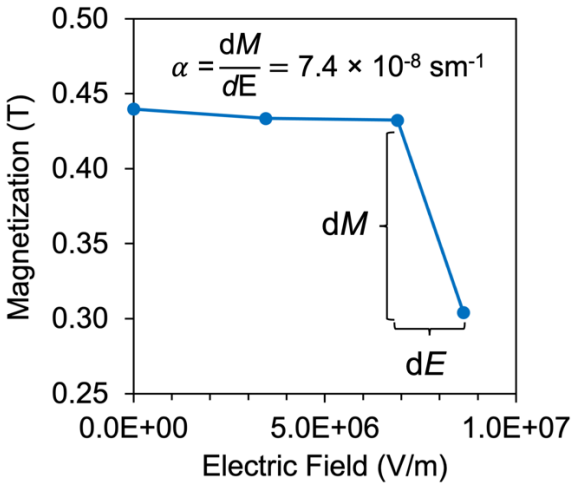

Figure B-S10. Calculation of magnetoelectric coupling coefficient (α). Magnetization change (dM) was divided by the change in electric field (dE) to obtain α.

Details of *in-situ* electrical poling during diffraction measurements

Sample preparation: Samples were mounted onto a glass slide, which were held in place on the diffraction sample mount through vacuum. Carbon tape was used to secure the sample onto the glass slide. The ground was connected to this bottom piece of carbon tape. To prevent the carbon tape from going over the sample edge, thus shorting the device, a thin piece of Kapton was used to cover the edge of the sample. Due to the porous nature of the sample, we are not able to use gas-phase deposition methods to sputter on a top electrode, since that would short our device. Additionally, in X-ray diffraction, we are not able to use any of the classic noble metals for a top electrode since X-rays cannot penetrate through heavy metals. Therefore, for the diffraction data, we used carbon tape as a top electrode to meet both of these needs. However, since carbon tape has polymeric adhesive in it, its resistivity is noticeably higher than the metal top electrodes used for the magnetization measurements. Specifically, the resistivity across the metallic top electrode

is 0.1-0.2 Ω, whereas the resistivity over the carbon tape is 1-2 Ω. That value, further, does not include the extra resistance in the adhesive component of the tape, which could effectively widen the electrode gap. Because of these issues, we have not converted the x-axis for the *in-situ* diffraction experiment to electric field, and have included this discussion to point out why slightly higher voltages were needed to see change in the diffraction experiment compared to the magnetization measurements. It should also be noted that the adhesive in carbon tape can off-gas upon significant resistive heating, and so voltages exceeding 20 V should not be used. Copper tape was used to secure a wire to the carbon tape.

Measurement details: Experiments were performed at beamline 17-2 at the Stanford Synchrotron Radiation Lightsource. An X-ray energy of 14 keV (λ = 0.886 Å) was used. It should be noted that a grazing-incidence geometry was used, so true out-of-plane and in-plane diffraction are not used here. An incidence angle of less than 3 ° was used, so samples are still effectively in-plane and out-of-plane.

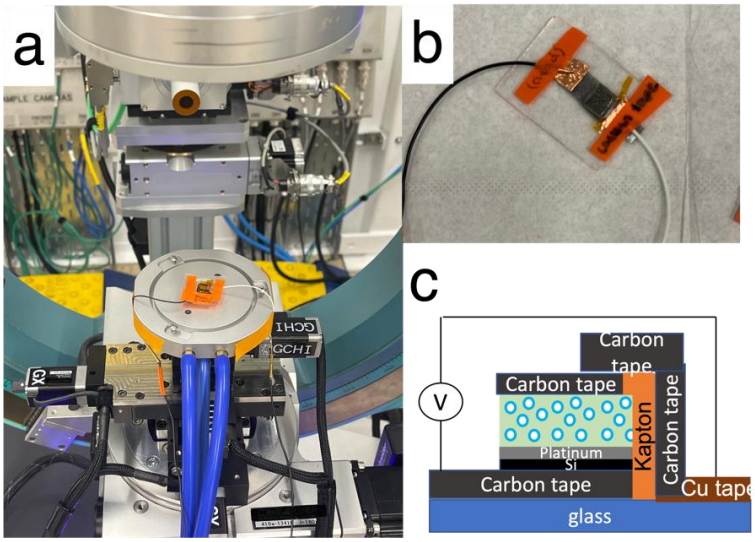

Figure B-S11. *In-situ* poling during high-resolution diffraction experiments. **a)** Sample on beamline 17-2 at SSRL. **b)** Close-up image of samples used for diffraction experiments. **c)** Schematic of sample preparation.

APPENDIX C

Supporting Information for Chapter 5: Delineating Magnetization Dynamics in Solution-Processed Doped Yttrium Iron Garnet Thin Films

Shreya K. Patel, C. Ty Karaba, Sarah H. Tolbert

Thick film characterization: For stripline FMR measurements, thicker films were used in order to obtain reasonable absorption. The synthesis of these films is discussed in the experimental section of the main text.

From diffraction, we see that thicker films still form the correct crystal structure (figure S1(a)). It should be noted, however, that since diffraction patterns for the thick films were collected on a conventional powder diffractometer, rather than using a synchrotron source, the signal-to-noise ratio is lower for the diffraction in figure S1(a) than in figure 1 of the main text, even though the films are thicker. The saturation magnetization of the thick films is similar to the thinner films shown in figure 2 (approximately 140 emu/cc), but the coercivity is slightly larger in the thick films. A value of ~ 50 Oe was obtained for the thick films, as opposed to ~25 Oe obtained in the thinner films (figure S1(b)). This is likely because thicker sol-gel films often exhibit more defects (cracks, pores, etc.) than thinner films. This effect can be seen in cross-sectional SEM images of thick and thin films (figure S1(c)). These defect sites can become domain wall pinning sites, which would increase the coercive field. For the same reason, we expect that magnetic inhomogeneities could also result in higher FMR linewidth in thicker films than thinner films, due to an increase in inhomogeneous line broadening. This topic is already discussed in the main text on manuscript.

To better assess how similar the magnetic losses are in thick and thinner films, we turned to electron spin resonance (ESR) to look at the dynamic magnetic behavior in an undoped thinner film (figure S1(d)). ESR utilizes a cavity tuned to a single frequency (9.8 GHz in this case), and due to the cavity resonance, it can measure the small signal from the thinner films, providing a point of direct comparison between film thicknesses. The linewidth of the thinner film is 238 Oe peak-to-peak, which corresponds to a FWHM value of 280 Oe. This value is lower than the thick films film value of 350 Oe, obtained by extrapolating stripline data to 9.8 GHz using the inhomogeneous line broadening (ΔH_0) and Gilbert damping (α) (main text, table 1), but the values are similar, and the difference is likely due to the defect sites discussed above. Overall, the values between thick and thinner films are similar enough that it appears reasonable to obtain absorption from stripline FMR measurements for thick films across a range of frequencies.

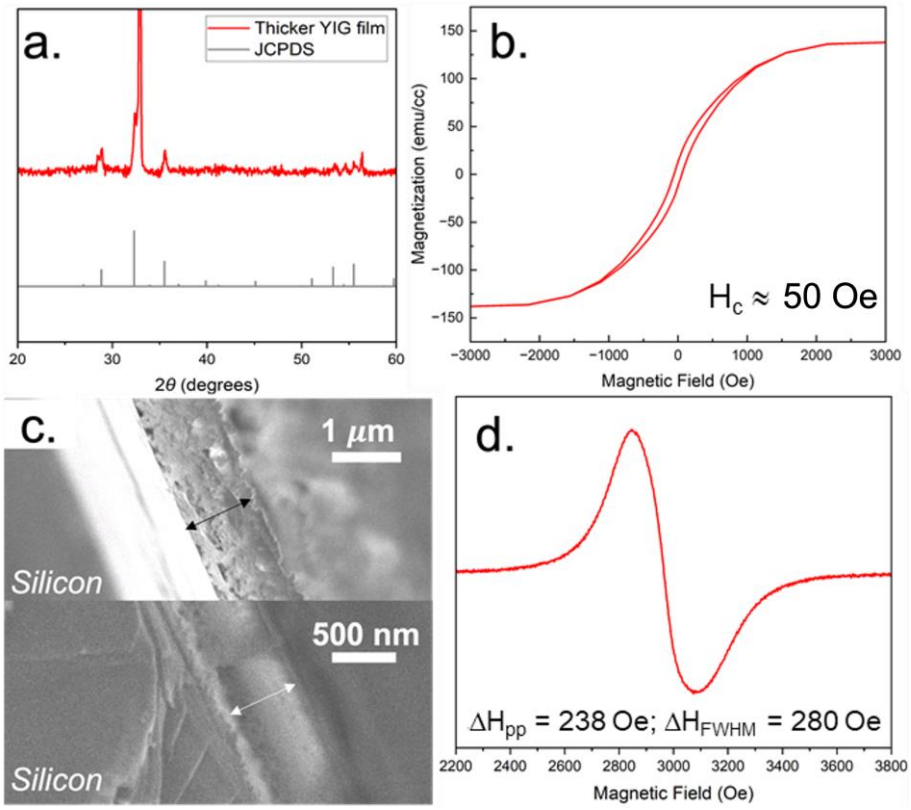

Figure C-S1. Characterization of thicker YIG films to compare to the thinner films discussed in the manuscript, including (a) X-ray diffraction (* indicates Si substrate peak), (b) an MH loop obtained trough SQuID magnetometry, and (c) SEM. An ESR spectrum of the thinner film (d) shows linewidth of the films at 9.8 GHz. Thus, while the coercivity and FMR linewidth of thicker films is slightly higher than those mentioned in the manuscript (likely due to an increase in defects in thicker films), they are overall comparable to the thinner films described in the manuscript.

APPENDIX D

Supporting Information for Chapter 6: Perpendicular Magnetic Anisotropy in Solution-Processed Epitaxial Ru-doped Yttrium Iron Garnet Thin Films

Shreya K. Patel, Michael E. Liao, Dorian Luccioni, Daniel D. Robertson‡, Charlene Z. Salamat‡, Ethan J. Savage‡, Alexandria Will-Cole, Nian X. Sun, Mark S. Goorsky, Sarah H. Tolbert

‡Authors contributed equally to this work.

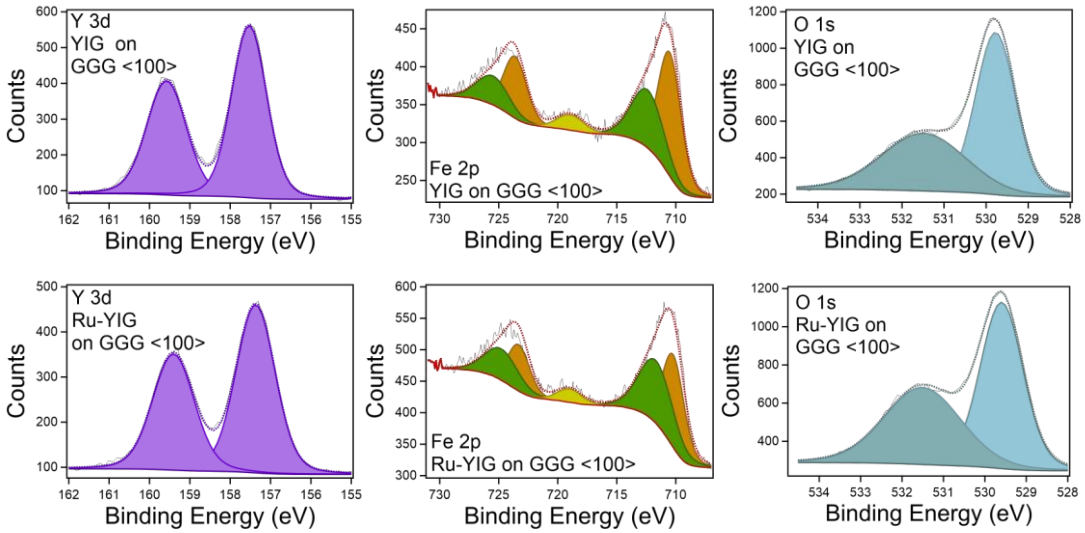

Figure D-S1. XPS spectra and fits collected for undoped and Ru:YIG grown on GGG(100).

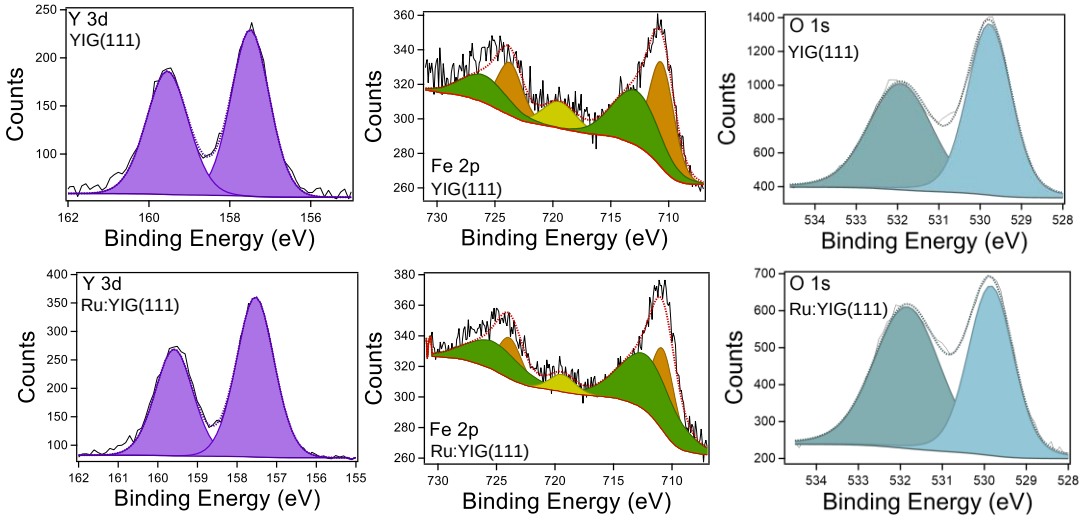

Figure D-S2. XPS spectra and fits collected for undoped and Ru:YIG grown on GGG(111).

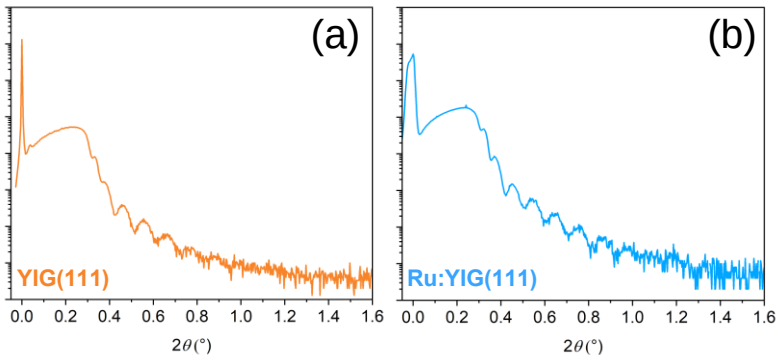

Figure D-S3. XRR patterns for selected films studied, (a) undoped YIG(111) and (b) Ru:YIG(111). Both films high thickness uniformity across the entire sample, as indicated by the fringes in the pattern

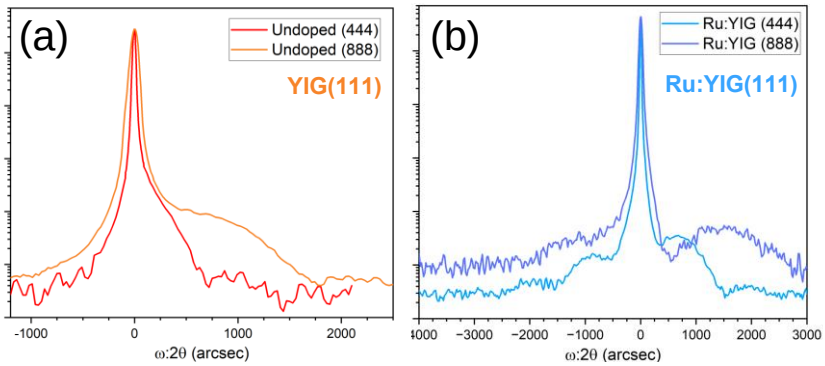

Figure D-S4. Selected higher-order reflections in XRD for (a) undoped YIG(111) and (b) Ru:YIG(111). Laue oscillations can be seen in both patterns, indicating good crystalline quality.

REFERENCES

(1) Spaldin, N. A.; Fiebig, M. The Renaissance of Magnetoelectric Multiferroics. *Science.* **2005**, *309*, 391–392.

(2) Nan, C.-W.; Bichurin, M. I.; Dong, S.; Viehland, D.; Srinivasan, G. Multiferroic Magnetoelectric Composites: Historical Perspective, Status, and Future Directions. *J. Appl. Phys.* **2008**, *103*, 031101.

(3) Vaz, C. A. F.; Hoffman, J.; Ahn, C. H.; Ramesh, R. Magnetoelectric Coupling Effects in Multiferroic Complex Oxide Composite Structures. *Adv. Mater.* **2010**, *22*, 2900–2918.

(4) Spaldin, N. A.; Ramesh, R. Advances in Magnetoelectric Multiferroics. *Nat. Mater.* **2019**, *18*, 203–212.

(5) Sun, N. X.; Srinivasan, G. Voltage Control of Magnetism in Multiferroic Heterostructures and Devices. *SPIN* **2012**, *2*, 1240004.

(6) Wang, Y.; Hu, J.; Lin, Y.; Nan, C. W. Multiferroic Magnetoelectric Composite Nanostructures. *NPG Asia Materials.* 2010.

(7) Viehland, D.; Li, J. F.; Yang, Y.; Costanzo, T.; Yourdkhani, A.; Caruntu, G.; Zhou, P.; Zhang, T.; Li, T.; Gupta, A.; Popov, M.; Srinivasan, G. Tutorial: Product Properties in Multiferroic Nanocomposites. *J. Appl. Phys.* **2018**, *124*, 061101.

(8) Zhou, J. P.; He, H. C.; Shi, Z.; Liu, G.; Nan, C. W. Dielectric, Magnetic, and Magnetoelectric Properties of Laminated $PbZr_{0.52}Ti_{0.48}O_3$-$CoFe_2O_4$ Composite Ceramics. *J. Appl. Phys.* **2006**, *100*, 0–6.

(9) Chen, W.; Zhu, W.; Chen, X.; Wang, Z. Enhanced Ferroelectric and Dielectric Properties of $CoFe_2O_4$-$Pb(Zr_{0.53}Ti_{0.47})O_3$ Multiferroic Composite Thick Films. *J. Am. Ceram. Soc.* **2010**, *93*, 796–799.

(10) Wan, J. G.; Wang, X. W.; Wu, Y. J.; Zeng, M.; Wang, Y.; Jiang, H.; Zhou, W. Q.; Wang, G. H.; Liu, J.-M. Magnetoelectric CoFe[Sub 2]O[Sub 4]–Pb(Zr,Ti)O[Sub 3] Composite Thin Films Derived by a Sol-Gel Process. *Appl. Phys. Lett.* **2005**, *86*, 122501.

(11) Sim, C. H.; Pan, A. Z. Z.; Wang, J. Thickness and Coupling Effects in Bilayered Multiferroic $CoFe_2O_4$/$Pb(Zr_{0.52}Ti_{0.48})O_3$ Thin Films. *J. Appl. Phys.* **2008**, *103*, 124109.

(12) Ding, L.-Y.; Wu, F.-X.; Chen, Y.-B.; Gu, Z.-B.; Zhang, S.-T. Controllable Microstructures and Multiferroic Properties of $Pb(Zr_{0.53}Ti_{0.47})O_3$–$CoFe_2O_4$ Composite Films. *Appl. Surf. Sci.* **2011**, *257*, 3840–3842.

(13) Xie, S.; Ma, F.; Liu, Y.; Li, J. Multiferroic CoFe2O4-Pb(Zr(0.52)Ti(0.48))O3 Core-Shell Nanofibers and Their Magnetoelectric Coupling. *Nanoscale* **2011**, *3*, 3152–3158.

(14) Tahmasebi, K.; Barzegar, A.; Ding, J.; Herng, T. S.; Huang, A.; Shannigrahi, S. Magnetoelectric Effect in $Pb(Zr_{0.95}Ti_{0.05})O_5$ and $CoFe_2O_4$ Heteroepitaxial Thin Film Composite. *Mater. Des.* **2011**, *32*, 2370–2373.

(15) Tahmasebi, K.; Barzegar, A.; Ding, J.; Herng, T. S.; Huang, L.; Huang, A.; Shannigrahi, S. Multiferroic Thin Film Composite of $Pb(Zr_{0.95}Ti_{0.05})O_3$/$CoFe_2O_4$ on Si and $SrTiO_3$ Substrates. *Thin Solid Films* **2013**, *537*, 76–79.

(16) Chien, D.; Buditama, A. N.; Schelhas, L. T.; Kang, H. Y.; Robbennolt, S.; Chang, J. P.; Tolbert, S. H. Tuning Magnetoelectric Coupling Using Porosity in Multiferroic Nanocomposites of ALD-Grown $Pb(Zr,Ti)O_3$ and Templated Mesoporous $CoFe_2O_4$. *Appl. Phys. Lett.* **2016**, *109*, 112904.

(17) Zheng, H.; Wang, J.; Lofland, S. E.; Ma, Z.; Mohaddes-Ardabili, L.; Zhao, T.; Salamanca-Riba, L.; Shinde, S. R.; Ogale, S. B.; Bai, F.; Viehland, D.; Jia, Y.; Schlom, D. G.; Wuttig, M.; Roytburd, A.; Ramesh, R. Multiferroic $BaTiO_3$-CoFe2O4 Nanostructures. *Science.*

2004, *303*, 661–663.

(18) Ortega, N.; Bhattacharya, P.; Katiyar, R. S.; Dutta, P.; Manivannan, A.; Seehra, M. S.; Takeuchi, I.; Majumder, S. B. Multiferroic Properties of Pb(Zr,Ti)O[Sub 3]/CoFe[Sub 2]O[Sub 4] Composite Thin Films. *J. Appl. Phys.* **2006**, *100*, 126105.

(19) Aimon, N. M.; Choi, H. K.; Sun, X. Y.; Kim, D. H.; Ross, C. A. Templated Self-Assembly of Functional Oxide Nanocomposites. *Adv. Mater.* **2014**, *26*, 3063–3067.

(20) Gao, X.; Zhang, D.; Wang, X.; Jian, J.; He, Z.; Dou, H.; Wang, H. Vertically Aligned Nanocomposite (BaTiO 3) 0.8 :(La 0.7 Sr 0.3 MnO 3) 0.2 Thin Films with Anisotropic Multifunctionalities. *Nanoscale Adv.* **2020**, *2*, 3276–3283.

(21) Kim, D. H.; Ning, S.; Ross, C. A. Self-Assembled Multiferroic Perovskite–Spinel Nanocomposite Thin Films: Epitaxial Growth, Templating and Integration on Silicon. *J. Mater. Chem. C* **2019**, *7*, 9128–9148.

(22) Sharma, Y.; Agarwal, R.; Collins, L.; Zheng, Q.; Ievlev, A. V.; Hermann, R. P.; Cooper, V. R.; Santosh, K. C.; Ivanov, I. N.; Katiyar, R. S.; Kalinin, S. V.; Lee, H. N.; Hong, S.; Ward, T. Z. Self-Assembled Room Temperature Multiferroic $BiFeO_3$-$LiFe5O_8$ Nanocomposites. *Adv. Funct. Mater.* **2020**, *30*, 1906849.

(23) Raidongia, K.; Nag, A.; Sundaresan, A.; Rao, C. N. R. Multiferroic and Magnetoelectric Properties of Core-Shell $CoFe_2O_4$@$BaTiO_3$ Nanocomposites. *Appl. Phys. Lett.* **2010**, *97*, 062904.

(24) Ojha, S.; Nunes, W. C.; Aimon, N. M.; Ross, C. A. Magnetostatic Interactions in Self-Assembled $Co_xNi_{1-x}Fe_2O_4$/$BiFeO_3$ Multiferroic Nanocomposites. *ACS Nano* **2016**, *10*, 7657–7664.

(25) Murakami, M.; Chang, K. S.; Aronova, M. A.; Lin, C. L.; Yu, M. H.; Simpers, J. H.;

Wuttig, M.; Takeuchi, I.; Gao, C.; Hu, B.; Lofland, S. E.; Knauss, L. A.; Bendersky, L. A. Tunable Multiferroic Properties in Nanocomposite $PbTiO_3$–$CoFe_2O_4$ Epitaxial Thin Films. *Appl. Phys. Lett.* **2005**, *87*, 112901.

(26) Li, J.; Levin, I.; Slutsker, J.; Provenzano, V.; Schenck, P. K.; Ramesh, R.; Ouyang, J.; Roytburd, A. L. Self-Assembled Multiferroic Nanostructures in the $CoFe_2O_4$-$PbTiO_3$ System. *Appl. Phys. Lett.* **2005**, *87*, 072909.

(27) Xiao, Z.; Lo Conte, R.; Goiriena-Goikoetxea, M.; Chopdekar, R. V.; Lambert, C. H. A.; Li, X.; N'Diaye, A. T.; Shafer, P.; Tiwari, S.; Barra, A.; Chavez, A.; Mohanchandra, K. P.; Carman, G. P.; Wang, K. L.; Salahuddin, S.; Arenholz, E.; Bokor, J.; Candler, R. N. Tunable Magnetoelastic Effects in Voltage-Controlled Exchange-Coupled Composite Multiferroic Microstructures. *ACS Appl. Mater. Interfaces* **2020**, *12*, 6752–6760.

(28) Quickel, T. E.; Le, V. H.; Brezesinski, T.; Tolbert, S. H. On the Correlation between Nanoscale Structure and Magnetic Properties in Ordered Mesoporous Cobalt Ferrite ($CoFe_2O_4$) Thin Films. *Nano Lett.* **2010**, *10*, 2982–2988.

(29) Quickel, T. E.; Schelhas, L. T.; Farrell, R. A.; Petkov, N.; Le, V. H.; Tolbert, S. H. Mesoporous Bismuth Ferrite with Amplified Magnetoelectric Coupling and Electric Field-Induced Ferrimagnetism. *Nat. Commun.* **2015**, *6*, 6562.

(30) Ortel, E.; Reier, T.; Strasser, P.; Kraehnert, R. Mesoporous IrO_2 Films Templated by PEO-PB-PEO Block-Copolymers: Self-Assembly, Crystallization Behavior, and Electrocatalytic Performance. *Chem. Mater.* **2011**, *23*, 3201–3209.

(31) Fang, J.; Kang, C. B.; Huang, Y.; Tolbert, S. H.; Pilon, L. Thermal Conductivity of Ordered Mesoporous Nanocrystalline Silicon Thin Films Made from Magnesium Reduction of Polymer-Templated Silica. *J. Phys. Chem. C* **2012**, *116*, 12926–12933.

(32) Rauda, I. E.; Buonsanti, R.; Saldarriaga-Lopez, L. C.; Benjauthrit, K.; Schelhas, L. T.; Stefik, M.; Augustyn, V.; Ko, J.; Dunn, B.; Wiesner, U.; Milliron, D. J.; Tolbert, S. H. General Method for the Synthesis of Hierarchical Nanocrystal-Based Mesoporous Materials. *ACS Nano* **2012**, *6*, 6386–6399.

(33) Hsueh, H.-Y.; Yao, C.-T.; Ho, R.-M. Well-Ordered Nanohybrids and Nanoporous Materials from Gyroid Block Copolymer Templates. *Chem. Soc. Rev.* **2015**, *44*, 1974–2018.

(34) Brinker, C. J.; Lu, Y.; Sellinger, A.; Fan, H. Evaporation-Induced Self-Assembly: Nanostructures Made Easy. *Adv. Mater.* **1999**, *11*, 579–585.

(35) Brezesinski, T.; Groenewolt, M.; Gibaud, A.; Pinna, N.; Antonietti, M.; Smarsly, B. Evaporation-Induced Self-Assembly (EISA) at Its Limit: Ultrathin, Crystalline Patterns by Templating of Micellar Monolayers. *Adv. Mater.* **2006**, *18*, 2260–2263.

(36) Yang, P. Hierarchically Ordered Oxides. *Science.* **1998**, *282*, 2244–2246.

(37) Fattakhova-Rohlfing, D.; Brezesinski, T.; Rathouský, J.; Feldhoff, A.; Oekermann, T.; Wark, M.; Smarsly, B. M. Transparent Conducting Films of Indium Tin Oxide with 3D Mesopore Architecture. *Adv. Mater.* **2006**, *18*, 2980–2983.

(38) Choi, J. H.; Zhang, F.; Perng, Y.-C.; Chang, J. P. Tailoring the Composition of Lead Zirconate Titanate by Atomic Layer Deposition. *J. Vac. Sci. Technol. B, Nanotechnol. Microelectron. Mater. Process. Meas. Phenom*. **2013**, *31*, 012207.

(39) Benedetto, J. M.; Moore, R. A.; McLean, F. B. Effects of Operating Conditions on the Fast-Decay Component of the Retained Polarization in Lead Zirconate Titanate Thin Films. *J. Appl. Phys.* **1994**, *75*, 460.

(40) Jenkins, I. G.; Song, T. K.; Madhukar, S.; Prakash, A. S.; Aggarwal, S.; Ramesh, R.

Dynamics of Polarization Loss in (Pb, La)(Zr, Ti)O_3 Thin Film Capacitors. *Appl. Phys. Lett.* **1998**, *72*, 3300–3302.

(41) Dunn, S. Determination of Cross Sectional Variation of Ferroelectric Properties for Thin Film (Ca. 500 Nm) PZT (30/70) via PFM. *Integr. Ferroelectr.* **2003**, *59*, 1505–1512.

(42) Choi, T.; Kim, J.-S.; Park, B. H.; Shin, H.; Lee, J. Ferroelectricity in Ultrathin $PbZrO_3$/$PbTiO_3$ Artificial Superlattices by Scanning Probe Microscopy. *Ferroelectrics* **2006**, *336*, 271–277.

(43) Kirsch, B. L.; Chen, X.; Richman, E. K.; Gupta, V.; Tolbert, S. H. Probing the Effects of Nanoscale Architecture on the Mechanical Properties of Hexagonal Silica/Polymer Composite Thin Films. *Adv. Funct. Mater.* **2005**, *15*, 1319–1327.

(44) Jaffe, H.; Berlincourt, D. A. Piezoelectric Transducer Materials. *Proc. IEEE* **1965**, *53*, 1372–1386.

(45) Hooker, M. W. Properties of PZT-Based Piezoelectric Ceramics Between −150 and 250°C. **1998**, No. September.

(46) Guo, R.; Cross, L. E.; Park, S.-E.; Noheda, B.; Cox, D. E.; Shirane, G. Origin of the High Piezoelectric Response in PbZr[1-x]Ti[x]O[3]. *Phys. Rev. Lett.* **2000**, *84*, 5423–5426.

(47) Roy, K. Area-Delay-Energy Tradeoffs of Strain-Mediated Multiferroic Devices. *IEEE Trans. Magn.* **2015**, *51*, 2500808.

(48) Van Den Boomgaard, J.; Van Run, A. M. J. G.; Van Suchtelen, J. Magnetoelectricity in Piezoelectric—Magnetostrictive Composites. *Ferroelectrics* **1976**, *10*, 295–298.

(49) Aubert, A.; Loyau, V.; Mazaleyrat, F.; LoBue, M. Enhancement of the Magnetoelectric Effect in Multiferroic CoFe2O4/PZT Bilayer by Induced Uniaxial Magnetic Anisotropy. *IEEE Trans. Magn.* **2017**, *53*, 8109405.

(50) Zhou, H. M.; Zhu, F. J.; Li, C.; Xiao, Y. Ferrite-Piezoelectric Layered Composite Materials for Magnetoelectric Tunable Dual-Band Bandpass Filter. *Appl. Mech. Mater.* **2013**, *303–306*, 1793–1797.

(51) Murugavel, P.; Padhan, P.; Prellier, W. Enhanced Magnetoresistance in Ferromagnetic $Pr_{0.85}Ca_{0.15}MnO_3$/ferroelectric $Ba_{0.6}Sr_{0.4}TiO_3$ Superlattice Films. *Appl. Phys. Lett.* **2004**, *85*, 4992.

(52) Singh, M. P.; Prellier, W.; Mechin, L.; Simon, C.; Raveau, B. Correlation between Structure and Properties in Multiferroic $La_{0.7}Ca_{0.3}MnO_3$/$BaTiO_3$ Superlattices. *J. Appl. Phys.* **2006**, *99*, 024105.

(53) Ma, Y. G.; Cheng, W. N.; Ning, M.; Ong, C. K. Magnetoelectric Effect in Epitaxial Pb(Zr0.52Ti0.48)O3/La0.7Sr0.3MnO3 Composite Thin Film. *Appl. Phys. Lett.* **2007**, *90*, 152911.

(54) Khojah, R.; Xiao, Z.; Panduranga, M. K.; Bogumil, M.; Wang, Y.; Goiriena-Goikoetxea, M.; Chopdekar, R. V; Bokor, J.; Carman, G. P.; Candler, R. N.; Di Carlo, D.; Khojah, R.; Bogumil, M.; Wang, Y.; Di Carlo, D.; Xiao, Z.; Candler, R. N.; Panduranga, M. K.; Carman, G. P.; Goiriena-Goikoetxea, M.; Bokor, J.; Chopdekar, R. V. Single-Domain Multiferroic Array-Addressable Terfenol-D (SMArT) Micromagnets for Programmable Single-Cell Capture and Release. *Adv. Mater.* **2021**, *33*, 2006651.

(55) Hsiao, Y. C.; Khojah, R.; Li, X.; Kundu, A.; Chen, C.; Gopman, D. B.; Chavez, A. C.; Lee, T.; Xiao, Z.; Sepulveda, A. E.; Candler, R. N.; Carman, G. P.; Di Carlo, D.; Lynch, C. S. Capturing Magnetic Bead-Based Arrays Using Perpendicular Magnetic Anisotropy. *Appl. Phys. Lett.* **2019**, *115*, 082402.

(56) Yao, Z.; Wang, Y. E.; Keller, S.; Carman, G. P. Bulk Acoustic Wave-Mediated

Multiferroic Antennas: Architecture and Performance Bound. *IEEE Trans. Antennas Propag.* **2015**.

(57) Wang, X. G.; Sukhov, A.; Chotorlishvili, L.; Jia, C. L.; Guo, G. H.; Berakdar, J. Electrically Driven Magnetic Antenna Based on Multiferroic Composites. *J. Phys. Condens. Matter* **2017**.

(58) Chu, Z.; Pourhosseiniasl, M.; Dong, S. Review of Multi-Layered Magnetoelectric Composite Materials and Devices Applications. *J. Phys. D. Appl. Phys.* **2018**, *51*, 243001.

(59) Levin, I.; Li, J.; Slutsker, J.; Roytburd, A. L. Design of Self-Assembled Multiferroic Nanostructures in Epitaxial Films. *Adv. Mater.* **2006**, *18*, 2044–2047.

(60) Murakami, M.; Chang, K. S.; Aronova, M. A.; Lin, C. L.; Yu, M. H.; Simpers, J. H.; Wuttig, M.; Takeuchi, I.; Gao, C.; Hu, B.; Lofland, S. E.; Knauss, L. A.; Bendersky, L. A. Tunable Multiferroic Properties in Nanocomposite $PbTiO_3$–$CoFe_2O_4$ Epitaxial Thin Films. *Appl. Phys. Lett.* **2005**, *87*, 112901.

(61) Chang, K. S.; Aronova, M. A.; Lin, C. L.; Murakami, M.; Yu, M. H.; Hattrick-Simpers, J.; Famodu, O. O.; Lee, S. Y.; Ramesh, R.; Wuttig, M.; Takeuchi, I.; Gao, C.; Bendersky, L. A. Exploration of Artificial Multiferroic Thin-Film Heterostructures Using Composition Spreads. *Appl. Phys. Lett.* **2004**, *84*, 3091.

(62) Ryu, S.; Park, J. H.; Jang, H. M. Magnetoelectric Coupling of [00l]-Oriented $Pb(Zr_{0.4}Ti_{0.6})O3$–Ni0.8Zn0.2Fe2O4 Multilayered Thin Films. *Appl. Phys. Lett.* **2007**, *91*, 142910.

(63) He, H. C.; Wang, J.; Zhou, J. P.; Nan, C. W. Ferroelectric and Ferromagnetic Behavior of $Pb(Zr_{0.52}Ti_{0.48})O_3$–$Co_{0.9}Zn_{0.1}Fe_2O_4$ Multilayered Thin Films Prepared via Solution Processing. *Adv. Funct. Mater.* **2007**, *17*, 1333–1338.

(64) Ryu, H.; Murugavel, P.; Lee, J. H.; Chae, S. C.; Noh, T. W.; Oh, Y. S.; Kim, H. J.; Kim, K. H.; Jang, J. H.; Kim, M.; Bae, C.; Park, J. G. Magnetoelectric Effects of Nanoparticulate $Pb(Zr_{0.52}Ti_{0.48})O_3$–$NiFe_2O_4$ Composite Films. *Appl. Phys. Lett.* **2006**, *89*, 102907.

(65) Mayeen, A.; Kala, M. S.; Jayalakshmy, M. S.; Thomas, S.; Philip, J.; Rouxel, D.; Bhowmik, R. N.; Kalarikkal, N. Flexible and Self-Standing Nickel Ferrite–PVDF-TrFE Cast Films: Promising Candidates for High-End Magnetoelectric Applications. *Dalt. Trans.* **2019**, *48*, 16961–16973.

(66) Choi, M. H.; Yang, S. C. $CoFe_2O_4$ Nanofiller Effect on β-Phase Formation of PVDF Matrix for Polymer-Based Magnetoelectric Composites. *Mater. Lett.* **2018**, *223*, 73–77.

(67) Luo, H.; Yang, H.; Baily, S. A.; Ugurlu, O.; Jain, M.; Hawley, M. E.; McCleskey, T. M.; Burrell, A. K.; Bauer, E.; Civale, L.; Holesinger, T. G.; Jia, Q. Self-Assembled Epitaxial Nanocomposite $BaTiO_3$-$NiFe_2O_4$ Films Prepared by Polymer-Assisted Deposition. *J. Am. Chem. Soc.* **2007**, *129*, 14132–14133.

(68) Yan, L. H.; Liang, W. Z.; Liu, S. H.; Huang, W.; Lin, Y. Multiferroic $BaTiO_3$-$CoFe_2O_4$ Nano Composite Thin Films Grown by Polymer-Assisted Deposition. *Integr. Ferroelectr.* **2011**, *131*, 82–88.

(69) Mori, K.; Kondo, Y.; Yamashita, H. Synthesis and Characterization of FePd Magnetic Nanoparticles Modified with Chiral BINAP Ligand as a Recoverable Catalyst Vehicle for the Asymmetric Coupling Reaction. *Phys. Chem. Chem. Phys.* **2009**, *11*, 8949–8954.

(70) Corral-Flores, V.; Bueno-Baques, D.; Carrillo-Flores, D.; Matutes-Aquino, J. A. Enhanced Magnetoelectric Effect in Core-Shell Particulate Composites. *J. Appl. Phys.* **2006**, *99*, 08J503.

(71) Lindemann, S.; Irwin, J.; Kim, G. Y.; Wang, B.; Eom, K.; Wang, J.; Hu, J.; Chen, L. Q.; Choi, S. Y.; Eom, C. B.; Rzchowski, M. S. Low-Voltage Magnetoelectric Coupling in Membrane Heterostructures. *Sci. Adv.* **2021**, *7*, 2294.

(72) Zheng, H.; Kreisel, J.; Chu, Y. H.; Ramesh, R.; Salamanca-Riba, L. Heteroepitaxially Enhanced Magnetic Anisotropy in $BaTiO_3$–$CoFe_2O_4$ Nanostructures. *Appl. Phys. Lett.* **2007**, *90*, 113113.

(73) Gao, X.; Li, L.; Jian, J.; Wang, H.; Fan, M.; Huang, J.; Wang, X.; Wang, H. Vertically Aligned Nanocomposite $BaTiO_3$:$YMnO_3$ Thin Films with Room Temperature Multiferroic Properties toward Nanoscale Memory Devices. *ACS Appl. Nano Mater.* **2018**, *1*, 2509–2514.

(74) Deng, C.; Zhang, Y.; Ma, J.; Lin, Y.; Nan, C. W. Magnetoelectric Effect in Multiferroic Heteroepitaxial $BaTiO_3$–$NiFe_2O_4$ Composite Thin Films. *Acta Mater.* **2008**, *56*, 405–412.

(75) Zhang, S. T.; Zhang, Y.; Luo, Z. L.; Lu, M. H.; Gu, Z. Bin; Chen, Y. F. Multiferroic Properties of $Bi_{0.8}La_{0.2}FeO_3$/$CoFe_2O_4$ Multilayer Thin Films. *Appl. Surf. Sci.* **2009**, *255*, 5092–5095.

(76) Brezesinski, T.; Wang, J.; Senter, R.; Brezesinski, K.; Dunn, B.; Tolbert, S. H. On the Correlation between Mechanical Flexibility, Nanoscale Structure, and Charge Storage in Periodic Mesoporous CeO2 Thin Films. *ACS Nano* **2010**, *4*, 967–977.

(77) Sree, S. P.; Dendooven, J.; Smeets, D.; Deduytsche, D.; Aerts, A.; Vanstreels, K.; Baklanov, M. R.; Seo, J. W.; Temst, K.; Vantomme, A.; Detavernier, C.; Martens, J. A. Spacious and Mechanically Flexible Mesoporous Silica Thin Film Composed of an Open Network of Interlinked Nanoslabs. *J. Mater. Chem.* **2011**, *21*, 7692–7699.

(78) Seth, S.; Jhulki, S. Porous Flexible Frameworks: Origins of Flexibility and Applications.

Mater. Horizons **2021**, *8*, 700–727.

(79) Huang, S.; Karaba, C. T.; Patel, S. K.; Neal, A.; Tolbert, S. H.; Marian, J. Simulating the Non-Monotonic Strain Response of Nanoporous Multiferroic Composites under Electric Field Control. *Appl. Phys. Lett.* **2022**, *120*, 213501.

(80) Buditama, A. N.; Fitzell, K.; Chien, D.; Karaba, C. T.; Patel, S. K.; Kang, H. Y.; Chang, J. P.; Tolbert, S. H. Strain Transfer in Porous Multiferroic Composites of $CoFe_2O_4$ and $PbZr_xTi_{1-x}O_3$. *Appl. Phys. Lett.* **2022**, *120*, 192902.

(81) Liang, X.; Dong, C.; Chen, H.; Wang, J.; Wei, Y.; Zaeimbashi, M.; He, Y.; Matyushov, A.; Sun, C.; Sun, N. A Review of Thin-Film Magnetoelastic Materials for Magnetoelectric Applications. *Sensors* **2020**, *20*, 1532.

(82) Yang, P.; Zhao, D.; Margolese, D. I.; Chmelka, B. F.; Stucky, G. D. Block Copolymer Templating Syntheses of Mesoporous Metal Oxides with Large Ordering Lengths and Semicrystalline Framework. *Chem. Mater.* **1999**, *11*, 2813–2826.

(83) Galo, G. J.; Crepaldi, E. L.; Grosso, D.; Sanchez, C. Block Copolymer-Templated Mesoporous Oxides. *Curr. Opin. Colloid Interface Sci.* **2003**, *8*, 109–126.

(84) Kim, D. M.; Eom, C. B.; Nagarajan, V.; Ouyang, J.; Ramesh, R.; Vaithyanathan, V.; Schlom, D. G. Thickness Dependence of Structural and Piezoelectric Properties of Epitaxial $Pb(Zr_{0.52}Ti_{0.48})O_3$ Films on Si and $SrTiO_3$ Substrates. *Appl. Phys. Lett.* **2006**, *88*, 142904.

(85) Araújo, E. B.; Lima, E. C.; Bdikin, I. K.; Kholkin, A. L. Thickness Dependence of Structure and Piezoelectric Properties at Nanoscale of Polycrystalline Lead Zirconate Titanate Thin Films. *J. Appl. Phys.* **2013**, *113*, 187206.

(86) Daniel Chen, H.; Udayakumar, K. R.; Kewen, K. L. I.; Gaskey, C. J.; Eric Cross, L.

Dielectric Breakdown Strength in Sol-Gel Derived PZT Thick Films. *Integr. Ferroelectr.* **2006**, *15*, 89–98.

(87) Kim, Y.; Pham, C.; Chang, J. P. Potentials and Challenges of Integration for Complex Metal Oxides in CMOS Devices and Beyond. *J. Phys. D. Appl. Phys.* **2015**, *48*, 063001.

(88) Pham, C. D.; Chang, J.; Zurbuchen, M. A.; Chang, J. P. Synthesis and Characterization of $BiFeO_3$ Thin Films for Multiferroic Applications by Radical Enhanced Atomic Layer Deposition. *Chem. Mater.* **2015**, *27*, 7282–7288.

(89) Chien, D.; Buditama, A. N.; Schelhas, L. T.; Kang, H. Y.; Robbennolt, S.; Chang, J. P.; Tolbert, S. H. Tuning Magnetoelectric Coupling Using Porosity in Multiferroic Nanocomposites of ALD-Grown Pb(Zr,Ti)O3 and Templated Mesoporous CoFe2O4. *Appl. Phys. Lett.* **2016**, *109*, 112904.

(90) Baklanov, M. R.; Mogilnikov, K. P.; Polovinkin, V. G.; Dultsev, F. N. Determination of Pore Size Distribution in Thin Films by Ellipsometric Porosimetry. *J. Vac. Sci. Technol. B Microelectron. Nanom. Struct. Process. Meas. Phenom.* **2000**, *18*, 1385.

(91) S. J. Gregg; K. S. W. Sing. *Adsorption, Surface Area, and Porosity*, 2nd ed.; R. Haul, Ed.; Academic Press: London, New York, 1982; Vol. 86.

(92) Suzuki, Y.; Van Dover, R. B.; Gyorgy, E. M.; Phillips, J. M.; Korenivski, V.; Werder, D. J.; Chen, C. H.; Felder, R. J.; Cava, R. J.; Krajewski, J. J.; Peck, W. F. Magnetic Properties of Epitaxial Ferrite Multilayer Films. *J. Appl. Phys.* **1998**, *79*, 5923.

(93) Wang, Y. G.; Zhong, W. L.; Zhang, P. L. Size Effects on the Curie Temperature of Ferroelectric Particles. *Solid State Commun.* **1994**, *92*, 519–523.

(94) Zhong, W. L.; Wang, Y. G.; Zhang, P. L. Size Effects on Phase Transitions in Ferroelectric Films. *Phys. Lett. A* **1994**, *189*, 121–126.

(95) Wang, C. L.; Smith, S. R. P. Landau Theory of the Size-Driven Phase Transition in Ferroelectrics. *J. Phys. Condens. Matter* **1995**, *7*, 7163.

(96) Alrub, A. M.; Ong, L. H. Thickness Dependence of Switching Time and Coercive Field in Ferroelectric Thin Films. *J. Appl. Phys.* **2011**, *109*, 084109.

(97) Ishibashi, Y.; Orihara, H.; Tilley, D. R. Thickness Transitions of Ferroelectricity in Thin Films. *J. Phys. Soc. Japan* **2013**, *67*, 3292–3297.

(98) Robbennolt, S.; Menéndez, E.; Quintana, A.; Gómez, A.; Auffret, S.; Baltz, V.; Pellicer, E.; Sort, J. Reversible, Electric-Field Induced Magneto-Ionic Control of Magnetism in Mesoporous Cobalt Ferrite Thin Films. *Sci. Rep.* **2019**, *9*, 1–14.

(99) Robbennolt, S.; Yu, P.; Nicolenco, A.; Mercier Fernandez, P.; Coll, M.; Sort, J. Magneto-Ionic Control of Magnetism in Two-Oxide Nanocomposite Thin Films Comprising Mesoporous Cobalt Ferrite Conformally Nanocoated with HfO_2. *Nanoscale* **2020**, *12*, 5987–5994.

(100) Nichterwitz, M.; Honnali, S.; Kutuzau, M.; Guo, S.; Zehner, J.; Nielsch, K.; Leistner, K. Advances in Magneto-Ionic Materials and Perspectives for Their Application. *APL Mater.* **2021**, *9*, 030903.

(101) Bauer, U.; Yao, L.; Tan, A. J.; Agrawal, P.; Emori, S.; Tuller, H. L.; Van Dijken, S.; Beach, G. S. D. Magneto-Ionic Control of Interfacial Magnetism. *Nat. Mater.* **2015**, *14*, 174–181.

(102) Tang, X.; Viswan, R.; Gao, M.; Leung, C. M.; Folger, C.; Luo, H.; Howe, B.; Li, J.; Viehland, D. Nanopillars with E-Field Accessible Multi-State ($N \geq 4$) Magnetization Having Giant Magnetization Changes in Self-Assembled $BiFeO_3$-$CoFe_2O_4$/$Pb(Mg_{1/3}Nb_{2/3})$-38at%$PbTiO_3$ Heterostructures. *Sci. Rep.* **2018**, *8*, 1–7.

(103) Zavaliche, F.; Zheng, H.; Mohaddes-Ardabili, L.; Yang, S. Y.; Zhan, Q.; Shafer, P.; Reilly, E.; Chopdekar, R.; Jia, Y.; Wright, P.; Schlom, D. G.; Suzuki, Y.; Ramesh, R. Electric Field-Induced Magnetization Switching in Epitaxial Columnar Nanostructures. *Nano Lett.* **2005**, *5*, 1793–1796.

(104) Tang, X.; Gao, M.; Leung, C. M.; Luo, H.; Li, J.; Viehland, D. Non-Volatility Using Materials with Only Volatile Properties: Vertically Integrated Magnetoelectric Heterostructures and Their Potential for Multi-Level-Cell Devices. *Appl. Phys. Lett.* **2019**, *114*, 242903.

(105) Xue, F.; Sato, N.; Bi, C.; Hu, J.; He, J.; Wang, S. X. Large Voltage Control of Magnetic Anisotropy in CoFeB/MgO/OX Structures at Room Temperature. *APL Mater.* **2019**, *7*, 101112.

(106) Zhao, J. L.; Lu, H. X.; Sun, J. R.; Shen, B. G. Thickness Dependence of Piezoelectric Property of Ultrathin $BiFeO_3$ Films. *Phys. B Condens. Matter* **2012**, *407*, 2258–2261.

(107) Srinivasan, G. Magnetoelectric Composites. *Annu. Rev. Mater. Res.* **2010**, *40*, 153–178.

(108) Van Den Boomgaard, J.; Van Run, A. M. J. G.; Van Suchtelen, J. Piezoelectric-Piezomagnetic Composites with Magnetoelectric Effect. *Ferroelectrics* **2011**, *14*, 727–728.

(109) Domann, J.; Wu, T.; Chung, T. K.; Carman, G. Strain-Mediated Magnetoelectric Storage, Transmission, and Processing: Putting the Squeeze on Data. *MRS Bull.* **2018**, *43*, 848–853.

(110) Xiao, Z.; Lai, C.; Zheng, R.; Goiriena-Goikoetxea, M.; Tamura, N.; Juarez, C. T.; Perry, C.; Singh, H.; Bokor, J.; Carman, G. P.; Candler, R. N. Localized Strain Profile in Surface Electrode Array for Programmable Composite Multiferroic Devices. *Appl. Phys. Lett.*

2021, *118*, 182901.

(111) Ryu, S.; Park, J. H.; Jang, H. M. Magnetoelectric Coupling of [00l]-Oriented $Pb(Zr_{0.4}Ti_{0.6})O_3$–$Ni_{0.8}Zn_{0.2}Fe_2O_4$ Multilayered Thin Films. *Appl. Phys. Lett.* **2007**, *91*, 142910.

(112) Aubert, A.; Loyau, V.; Pascal, Y.; Mazaleyrat, F.; Lobue, M. Dynamic Magnetostriction of $CoFe_2O_4$ and Its Role in Magnetoelectric Composites. *Phys. Rev. Appl.* **2018**, *9*, 044035.

(113) Guchhait, S.; Aireddy, H.; Das, A. K. The Emergence of High Room Temperature In-Plane and out-of-Plane Magnetostriction in Polycrystalline $CoFe_2O_4$ Film. *Sci. Rep.* **2021**, *11*, 1–8.

(114) George, S. M. Atomic Layer Deposition: An Overview. *Chem. Rev.* **2010**, *110*, 111–131.

(115) Leskelä, M.; Ritala, M. Atomic Layer Deposition Chemistry: Recent Developments and Future Challenges. *Angew. Chemie Int. Ed.* **2003**, *42*, 5548–5554.

(116) Johnson, R. W.; Hultqvist, A.; Bent, S. F. A Brief Review of Atomic Layer Deposition: From Fundamentals to Applications. *Mater. Today* **2014**, *17*, 236–246.

(117) Patel, S. K.; Karaba, C. T.; Robertson, D. D.; Chang, J.; Fitzell, K.; Salamat, C. Z.; Chang, J. P.; Tolbert, S. H. Increased Magnetoelectric Coupling in Porous Nanocomposites of $CoFe_2O_4$ and $BiFeO_3$ with Residual Porosity for Switchable Magnetic Devices. *ACS Appl. Nano Mater.* **2023**, *6*, 4141–4150.

(118) Park, M. H.; Lee, Y. H.; Mikolajick, T.; Schroeder, U.; Hwang, C. S. Review and Perspective on Ferroelectric HfO_2-Based Thin Films for Memory Applications. *MRS Commun.* **2018**, *8*, 795–808.

(119) Kim, S. J.; Mohan, J.; Summerfelt, S. R.; Kim, J. Ferroelectric $Hf_{0.5}Zr_{0.5}O_2$ Thin Films: A

Review of Recent Advances. *JOM* **2019**, *71*, 246–255.

(120) Kim, J. Y.; Choi, M. J.; Jang, H. W. Ferroelectric Field Effect Transistors: Progress and Perspective. *APL Mater.* **2021**, *9*, 021102.

(121) Peng, W. L.; Zhang, J. Y.; Feng, G. N.; Xu, X. L.; Yang, C.; Jia, Y. L.; Yu, G. H. Tunable Damping-like and Field-like Spin-Orbit-Torque in Pt/Co/HfO_2 Films via Interfacial Charge Transfer. *Appl. Phys. Lett.* **2019**, *115*, 172403.

(122) Yang, Q.; Tao, L.; Jiang, Z.; Zhou, Y.; Tsymbal, E. Y.; Alexandrov, V. Magnetoelectric Effect at the Ni/HfO_2 Interface Induced by Ferroelectric Polarization. *Phys. Rev. Appl.* **2019**, *12*, 024044.

(123) Wei, Y.; Matzen, S.; Maroutian, T.; Agnus, G.; Salverda, M.; Nukala, P.; Chen, Q.; Ye, J.; Lecoeur, P.; Noheda, B. Magnetic Tunnel Junctions Based on Ferroelectric $Hf_{0.5}Zr_{0.5}O_2$ Tunnel Barriers. *Phys. Rev. Appl.* **2019**, *12*, 031001.

(124) Vermeulen, B. F.; Ciubotaru, F.; Popovici, M. I.; Swerts, J.; Couet, S.; Radu, I. P.; Stancu, A.; Temst, K.; Groeseneken, G.; Adelmann, C.; Martens, K. M. Ferroelectric Control of Magnetism in Ultrathin HfO_2/Co/Pt Layers. *ACS Appl. Mater. Interfaces* **2019**, *11*, 34385–34393.

(125) Dmitriyeva, A.; Mikheev, V.; Zarubin, S.; Chouprik, A.; Vinai, G.; Polewczyk, V.; Torelli, P.; Matveyev, Y.; Schlueter, C.; Karateev, I.; Yang, Q.; Chen, Z.; Tao, L.; Tsymbal, E. Y.; Zenkevich, A. Magnetoelectric Coupling at the Ni/$Hf_{0.5}Zr_{0.5}O_2$ Interface. *ACS Nano* **2021**, *15*, 14891–14902.

(126) Chen, J.; Zhao, L.; Tian, G.; Yang, T.; Cao, W.; Xu, J.; Gao, J.; Li, J.; Wang, W.; Kang, J.; Bu, W.; Zheng, K.; Yang, B.; Yue, L.; Cui, Y.; Luo, J. Highly Efficient Voltage-Controlled Magnetism in HfZrO/CoFeB Hybrid Film and Hall Device. *Jpn. J. Appl. Phys.*

2022, *61*, SJ1006.

(127) Materlik, R.; Kunneth, C.; Kersch, A. The Origin of Ferroelectricity in $Hf_{1-x}Zr_xO_2$: A Computational Investigation and a Surface Energy Model. *J. Appl. Phys.* **2015**, *117*, 134109.

(128) Dutta, S.; Buragohain, P.; Glinsek, S.; Richter, C.; Aramberri, H.; Lu, H.; Schroeder, U.; Defay, E.; Gruverman, A.; Íñiguez, J. Piezoelectricity in Hafnia. *Nat. Commun.* **2021**, *12*, 1–10.

(129) Lefki, K.; Dormans, G. J. M. Measurement of Piezoelectric Coefficients of Ferroelectric Thin Films. *J. Appl. Phys.* **1998**, *76*, 1764.

(130) Cheema, S. S.; Shanker, N.; Hsu, S. L.; Rho, Y.; Hsu, C. H.; Stoica, V. A.; Zhang, Z.; Freeland, J. W.; Shafer, P.; Grigoropoulos, C. P.; Ciston, J.; Salahuddin, S. Emergent Ferroelectricity in Subnanometer Binary Oxide Films on Silicon. *Science.* **2022**, *376*, 648–652.

(131) Cheema, S. S.; Kwon, D.; Shanker, N.; dos Reis, R.; Hsu, S. L.; Xiao, J.; Zhang, H.; Wagner, R.; Datar, A.; McCarter, M. R.; Serrao, C. R.; Yadav, A. K.; Karbasian, G.; Hsu, C. H.; Tan, A. J.; Wang, L. C.; Thakare, V.; Zhang, X.; Mehta, A.; Karapetrova, E.; Chopdekar, R. V.; Shafer, P.; Arenholz, E.; Hu, C.; Proksch, R.; Ramesh, R.; Ciston, J.; Salahuddin, S. Enhanced Ferroelectricity in Ultrathin Films Grown Directly on Silicon. *Nature* **2020**, *580*, 478–482.

(132) Cao, J.; Shi, S.; Zhu, Y.; Chen, J. An Overview of Ferroelectric Hafnia and Epitaxial Growth. *Phys. status solidi – Rapid Res. Lett.* **2021**, *15*, 2100025.

(133) Hu, G.; Harris, V. G.; Suzuki, Y. Microstructure and Magnetic Properties of Cobalt Ferrite Thin Films. *IEEE Trans. Magn.* **2001**, *37*, 2347–2349.

(134) Pramanik, N. C.; Fujii, T.; Nakanishi, M.; Takada, J. Effect of Co^{2+} Ion on the Magnetic Properties of Sol–Gel Cobalt Ferrite Thin Films. *J. Mater. Chem*. **2004**, *14*, 3328–3332.

(135) Suzuki, Y.; Hu, G.; Van Dover, R. B.; Cava, R. J. Magnetic Anisotropy of Epitaxial Cobalt Ferrite Thin Films. *J. Magn. Magn. Mater.* **1999**, *191*, 1–8.

(136) Wayne, R. C.; Samara, G. A.; Lefever, R. A. Effects of Pressure on the Magnetization of Ferrites: Anomalies Due to Strain-Induced Anisotropy in Porous Samples. *J. Appl. Phys.* **2003**, *41*, 633.

(137) Royce, E. B. Anomalous Shock-Induced Demagnetization of Nickel Ferrite. *J. Appl. Phys.* **2004**, *37*, 4066.

(138) Liu, H. J.; Wang, C. K.; Su, D.; Amrillah, T.; Hsieh, Y. H.; Wu, K. H.; Chen, Y. C.; Juang, J. Y.; Eng, L. M.; Jen, S. U.; Chu, Y. H. Flexible Heteroepitaxy of $CoFe_2O_4$/Muscovite Bimorph with Large Magnetostriction. *ACS Appl. Mater. Interfaces* **2017**, *9*, 7297–7304.

(139) Zhang, Y.; Shen, L.; Liu, M.; Li, X.; Lu, X.; Lu, L.; Ma, C.; You, C.; Chen, A.; Huang, C.; Chen, L.; Alexe, M.; Jia, C. L. Flexible Quasi-Two-Dimensional $CoFe_2O_4$ Epitaxial Thin Films for Continuous Strain Tuning of Magnetic Properties. *ACS Nano* **2017**, *11*, 8002–8009.

(140) Wang, Z.; Viswan, R.; Hu, B.; Li, J. F.; Harris, V. G.; Viehland, D. Domain Rotation Induced Strain Effect on the Magnetic and Magneto-Electric Response in CoFe2O4/Pb(Mg,Nb)O3-PbTiO3 Heterostructures. *J. Appl. Phys.* **2012**, *111*, 034108.

(141) Rus, S. F.; Herklotz, A.; Roth, R.; Schultz, L.; Dörr, K. Thickness Dependence of the Magnetoelastic Effect of $CoFe_2O_4$ Films Grown on Piezoelectric Substrates. *J. Appl. Phys.* **2013**, *114*, 043913.

(142) Yang, J. J.; Zhao, Y. G.; Tian, H. F.; Luo, L. B.; Zhang, H. Y.; He, Y. J.; Luo, H. S. Electric Field Manipulation of Magnetization at Room Temperature in Multiferroic $CoFe_2O_4$/$Pb(Mg_{1/3}Nb_{2/3})_{0.7}Ti_{0.3}O_3$ Heterostructures. *Appl. Phys. Lett.* **2009**, *94*, 212504.

(143) Fritsch, D.; Ederer, C. Effect of Epitaxial Strain on the Cation Distribution in Spinel Ferrites CoFe2O4 and NiFe2O4: A Density Functional Theory Study. *Appl. Phys. Lett.* **2011**, *99*, 081916.

(144) Vermeulen, B. F.; Ciubotaru, F.; Popovici, M. I.; Swerts, J.; Couet, S.; Radu, I. P.; Stancu, A.; Temst, K.; Groeseneken, G.; Adelmann, C.; Martens, K. M. Ferroelectric Control of Magnetism in Ultrathin HfO_2/Co/Pt Layers. *ACS Appl. Mater. Interfaces* **2019**, *11*, 34385–34393.

(145) Tatarenko, A. S.; Gheevarughese, V.; Srinivasan, G. Magnetoelectric Microwave Bandpass Filter. *Electron. Lett.* **2006**, *42*, 540–541.

(146) Petrov, R. V.; Tatarenko, A. S.; Pandey, S.; Srinivasan, G.; Mantese, J. V.; Azadegan, R. Miniature Antenna Based on Magnetoelectric Composites. *Electron. Lett.* **2008**, *44*, 506–508.

(147) Hauser, C.; Richter, T.; Homonnay, N.; Eisenschmidt, C.; Qaid, M.; Deniz, H.; Hesse, D.; Sawicki, M.; Ebbinghaus, S. G.; Schmidt, G. Yttrium Iron Garnet Thin Films with Very Low Damping Obtained by Recrystallization of Amorphous Material. *Sci. Rep.* **2016**, *6*, 1–8.

(148) Yahya, N. B.; Koziol, K. K. K.; Bin Mansor, M. K. Synthesis and Characterization of Single Crystals Y3Fe5O12 and Bi3Fe5O12 Prepared via Sol Gel Technique. *Defect Diffus. Forum* **2008**, *283–286*, 406–412.

(149) Stadler, B. J. H.; Mizumoto, T. Integrated Magneto-Optical Materials and Isolators: A

Review. *IEEE Photonics J.* **2014**, *6*.

(150) Ghosh, S.; Keyvaninia, S.; Shoji, Y.; Van Roy, W.; Mizumoto, T.; Roelkens, G.; Baets, R. G. Compact Mach-Zehnder Interferometer Ce:YIG/SOI Optical Isolators. *IEEE Photonics Technol. Lett.* **2012**, *24*, 1653–1656.

(151) Firby, C. J.; Elezzabi, A. Y. Design of Integrated YIG-Based Isolators and High-Speed Modulators. *Ultrafast Phenom. Nanophotonics* **2016**, *9746*, 108–115.

(152) How, H.; Shi, P.; Vittoria, C.; Kempel, L. C.; Trott, K. D. Single-Crystal YIG Phase Shifter Using Composite Stripline Structure at X Band. *J. Appl. Phys.* **2000**, *87*, 4966.

(153) Wang, X. guang; Chotorlishvili, L.; Guo, G. hua; Berakdar, J. Electric Field Controlled Spin Waveguide Phase Shifter in YIG. *J. Appl. Phys.* **2018**, *124*, 073903.

(154) Yang, X.; Gao, Y.; Wu, J.; Zhou, Z.; Beguhn, S.; Nan, T.; Sun, N. X. Voltage Tunable Multiferroic Phase Shifter with YIG/PMN-PT Heterostructure. *IEEE Microw. Wirel. Components Lett.* **2014**, *24*, 191–193.

(155) Baños-López, E.; Cortés-Escobedo, C. A.; Sánchez-De Jesús, F.; Barba-Pingarrón, A.; Bolarín-Miró, A. M. Crystal Structure and Magnetic Properties of Cerium-Doped YIG: Effect of Doping Concentration and Annealing Temperature. *J. Alloys Compd.* **2018**, *730*, 127–134.

(156) Hansen, P.; Witter, K.; Tolksdorf, W. Magnetic and Magneto-Optic Properties of Lead- and Bismuth-Substituted Yttrium Iron Garnet Films. *Phys. Rev. B* **1983**, *27*, 6608–6625.

(157) Krishnan, R.; Cagan, V.; Rivoire, M.; Graham, C. D.; Rhyne, J. J. Magnetostriction in Ruthenium-Doped YIG Crystals. In *AIP Conference Proceedings*; AIP, 2012; Vol. 5, pp 704–706.

(158) Comstock, R. L.; Raymond, J. J. Magnetostriction of Ytterbium and Cerium in YIG. *J.*

Appl. Phys. **1967**, *38*, 3737–3739.

(159) Kehlberger, A.; Richter, K.; Onbasli, M. C.; Jakob, G.; Kim, D. H.; Goto, T.; Ross, C. A.; Götz, G.; Reiss, G.; Kuschel, T.; Kläui, M. Enhanced Magneto-Optic Kerr Effect and Magnetic Properties of $CeY_2Fe_5O_{12}$ Epitaxial Thin Films. *Phys. Rev. Appl.* **2015**, *4*, 014008.

(160) Enke, K.; Fleishhauer, J.; Gunsser, W.; Hanser, P.; Nomura, S.; Tolksdorf, W.; Winkler, G.; Wolfmeier, U.; Hellwege, K.-H.; Hellwege, A. M. *Magnetic and Other Properties of Oxides and Related Compounds: Part A: Garnets and Perovskites*; Springer-Verlag: New York, 1978.

(161) Smith, A. B.; Jones, R. V. Magnetostriction Constants from Ferromagnetic Resonance. *J. Appl. Phys.* **1963**, *34*, 1283–1284.

(162) Lage, E.; Beran, L.; Quindeau, A. U.; Ohnoutek, L.; Kucera, M.; Antos, R.; Sani, S. R.; Dionne, G. F.; Veis, M.; Ross, C. A. Temperature-Dependent Faraday Rotation and Magnetization Reorientation in Cerium-Substituted Yttrium Iron Garnet Thin Films. *APL Mater.* **2017**, *5*, 036104.

(163) Kuila, M.; Deshpande, U.; Choudhary, R. J.; Rajput, P.; Phase, D. M.; Raghavendra Reddy, V. Study of Magneto-Optical Activity in Cerium Substituted Yttrium Iron Garnet (Ce:YIG) Epitaxial Thin Films. *J. Appl. Phys.* **2021**, *129*, 93903.

(164) Onbasli, M. C.; Beran, L.; Zahradník, M.; Kucera, M.; Antoš, R.; Mistrík, J.; Dionne, G. F.; Veis, M.; Ross, C. A. Optical and Magneto-Optical Behavior of Cerium Yttrium Iron Garnet Thin Films at Wavelengths of 200-1770 Nm. *Sci. Rep.* **2016**, *6*, 1–10.

(165) Dionne, G. F. The Magnetoelastic Ion: Friend and Foe to Microwaves. *IEEE Trans. Magn.* **2011**, *47*, 272–278.

(166) Acosta, A.; Fitzell, K.; Schneider, J. D.; Dong, C.; Yao, Z.; Sheil, R.; Wang, Y. E.; Carman, G. P.; Sun, N. X.; Chang, J. P. Underlayer Effect on the Soft Magnetic, High Frequency, and Magnetostrictive Properties of FeGa Thin Films. *J. Appl. Phys.* **2020**, *128*, 013903.

(167) Gu, W.; Xu, Q.; Wang, Y. E. Two Dimensional (2D) Complex Permeability Characterization of Thin Film Ferromagnetic Material. In *2016 IEEE Conference on Antenna Measurements & Applications (CAMA 2016)*; Syracuse, 2016; pp 224–228.

(168) Bonnet, M.; Delapalme, A.; Fuess, H.; Thomas, M.; IUCr. Refinement of the Structure of Yttrium Iron Garnet (YIG): A Case of Severe Extinction and Absorption. *Acta Crystallogr.* **1975**, *31*, 2233–2240.

(169) Geller, S. Magnetic Behavior of Substituted Ferrimagnetic Garnets. *J. Appl. Phys.* **2004**, *37*, 1408.

(170) K.H. Hellwege; A.M. Hellwege. *Landolt-Börnstein - Group III Crystal and Solid State Physics*; Spinger-Werlag: Berlin/Heidelberg, 1978; Vol. 18a.

(171) Hansen, P. Ferromagnetic Resonance in Ruthenium-doped Yttrium–Iron Garnet. *Phys. status solidi* **1971**, *47*, 565–572.

(172) Öztürk, Y.; Avgin, I.; Erol, M.; Çelik, E. Cerium-Doped Yttrium Iron Garnet Thin Films Prepared by Sol-Gel Process: Synthesis, Characterization, and Magnetic Properties. In *Advances in Nanoscale Magnetism*; 2009; pp 113–129.

(173) Shirsath, S. E.; Gaikwad, A. S.; Kadam, A. B.; Borade, R. B.; Patange, S. M.; Kadam, S. B.; Vats, G.; Kadam, R. H. Polycrystalline to Preferred-(100) Single Crystal Texture Phase Transformation of Yttrium Iron Garnet Nanoparticles. *Nanoscale Adv.* **2018**.

(174) Casals, B.; Espínola, M.; Cichelero, R.; Geprägs, S.; Opel, M.; Gross, R.; Herranz, G.;

Fontcuberta, J. Untangling the Contributions of Cerium and Iron to the Magnetism of Ce-Doped Yttrium Iron Garnet. *Appl. Phys. Lett.* **2016**, *108*.

(175) Niyaifar, M.; Mohammadpour, H.; Khalafi, N. Effects of Structural Distortion on Magnetic Properties of $Ce_xY_{3-x}Fe_5O_{12}$. *J. Alloys Compd.* **2016**, *688*, 357–362.

(176) Gharibshahi, M. Physical Properties of Cerium Doped-Yttrium Iron Garnet Ultrathin Films for Photovoltaic Application. *Ceram. Int.* **2019**, *45*, 24437–24445.

(177) Sharma, V.; Saha, J.; Patnaik, S.; Kuanr, B. K. Synthesis and Characterization of Yttrium Iron Garnet (YIG) Nanoparticles - Microwave Material. *AIP Adv.* **2016**, *7*, 056405.

(178) Peña-Garcia, R.; Delgado, A.; Guerra, Y.; Farias, B. V. M.; Martinez, D.; Skovroinski, E.; Galembeck, A.; Padrón-Hernández, E. Magnetic and Structural Properties of Zn-Doped Yttrium Iron Garnet Nanoparticles. *Phys. Status Solidi Appl. Mater. Sci.* **2016**, *213*, 2485–2491.

(179) Kuchi, R.; Kim, S. Il; Lee, K. M.; Lee, Y.; Park, S. Y.; Jeong, J. R. Annealing Effect on Ferromagnetic Resonance and Magnetic Properties of YIG Nanocrystals Prepared by Citrate Precursor Sol-Gel Method. *Nanosci. Nanotechnol. Lett.* **2015**.

(180) Nguyet, D. T. T.; Duong, N. P.; Satoh, T.; Anh, L. N.; Hien, T. D. Temperature-Dependent Magnetic Properties of Yttrium Iron Garnet Nanoparticles Prepared by Citrate Sol–Gel. *J. Alloys Compd.* **2012**, *541*, 18–22.

(181) Musa, M. A.; Azis, R. S.; Osman, N. H.; Hassan, J.; Zangina, T. Structural and Magnetic Properties of Yttrium Iron Garnet (YIG) and Yttrium Aluminum Iron Garnet (YAlG) Nanoferrite via Sol-Gel Synthesis. *Results Phys.* **2017**, *7*, 1135–1142.

(182) Leal, L. R. F.; Guerra, Y.; Padrón-Hernández, E.; Rodrigues, A. R.; Santos, F. E. P.; Peña-Garcia, R. Structural and Magnetic Properties of Yttrium Iron Garnet Nanoparticles

Doped with Copper Obtained by Sol Gel Method. *Mater. Lett.* **2019**, *236*, 547–549.

(183) Borade, R. B.; Shirsath, S. E.; Vats, G.; Gaikwad, A. S.; Patange, S. M.; Kadam, S. B.; Kadam, R. H.; Kadam, A. B. Polycrystalline to Preferred-(100) Single Crystal Texture Phase Transformation of Yttrium Iron Garnet Nanoparticles. *Nanoscale Adv.* **2019**, *1*, 403–413.

(184) Peña-Garcia, R.; Delgado, A.; Guerra, Y.; Padrón- Hernández, E. Yig Films With Low Magnetic Damping Obtained By Solgel On Silicon (100). *Mater. Lett.* **2015**, *161*, 384–386.

(185) Liu, F.; Ye, S. YIG Thin Film for RF Integrated Inductor. *J. Wuhan Univ. Technol. Mater. Sci. Ed.* **2017**.

(186) Tsuchiya, T.; Sei, T.; Kanda, H. Sol-Gel Preparation of YIG (Y3Fe5O12) Thin Film Showing Opto-Magnetic Effect. *J. Non. Cryst. Solids* **1992**.

(187) Shaiboub, R. E.; Ibrahim, N. B. Characterization of Erbium Substituted Yttrium Iron Garnet Films Prepared by Sol-Gel Method. *J. Nanosci.* **2014**.

(188) Delgado, A.; Guerra, Y.; Padrón-Hernández, E.; Peña-Garcia, R. Combining the Sol Gel Method and Spin Coating to Obtain YIG Films with Low FMR Linewidth on Silicon (100) Substrate. *Mater. Res. Express* **2018**.

(189) Lucas, I.; Jiménez-Cavero, P.; Vila-Fungueiriño, J. M.; Magén, C.; Sangiao, S.; De Teresa, J. M.; Morellón, L.; Rivadulla, F. Chemical Solution Synthesis and Ferromagnetic Resonance of Epitaxial Thin Films of Yttrium Iron Garnet. *Phys. Rev. Mater.* **2017**, *1*, 074407.

(190) Guo, X.; Chen, Y.; Wang, G.; Zhang, Y.; Ge, J.; Tang, X.; Ponchel, F.; Rémiens, D.; Dong, X. Growth and Characterization of Yttrium Iron Garnet Films on Si Substrates by

Chemical Solution Deposition (CSD) Technique. *J. Alloys Compd.* **2016**, *671*, 234–237.

(191) Singh, B. K.; Mishra, S. K. Microstructure and Surface Morphology of YIG and 2 Wt% Ce-Doped YIG Thin Films Synthesized via Sol-Gel Method. *Mater. Today Proc.* **2020**, *44*, 886–889.

(192) Chen, F.; Wang, X.; Nie, Y.; Li, Q.; Ouyang, J.; Feng, Z.; Chen, Y.; Harris, V. G. Ferromagnetic Resonance Induced Large Microwave Magnetodielectric Effect in Cerium Doped $Y_3Fe_5O_{12}$ Ferrites. *Sci. Rep.* **2016**, *6*, 1–8.

(193) Oosterhout, S. D.; Savikhin, V.; Zhang, J.; Zhang, Y.; Burgers, M. A.; Marder, S. R.; Bazan, G. C.; Toney, M. F. Mixing Behavior in Small Molecule:Fullerene Organic Photovoltaics. *Chem. Mater.* **2017**, *29*, 3062–3069.

(194) Ilavsky, J. Nika: Software for Two-Dimensional Data Reduction. *J. Appl. Crystallogr.* **2012**, *45*, 324–328.

(195) Xu, Q.; Gu, W.; Wang, Y. E. Two Dimensional (2D) Complex Permeability Characterization of Thin Film Ferromagnetic Material. In *2016 IEEE Conference on Antenna Measurements and Applications, CAMA 2016*; Institute of Electrical and Electronics Engineers Inc., 2017.

(196) Onbasli, M. C.; Kehlberger, A.; Kim, D. H.; Jakob, G.; Kläui, M.; Chumak, A. V.; Hillebrands, B.; Ross, C. A. Pulsed Laser Deposition of Epitaxial Yttrium Iron Garnet Films with Low Gilbert Damping and Bulk-like Magnetization. *APL Mater.* **2014**, *2*, 106102.

(197) Hauser, H.; Jiles, D. C.; Melikhov, Y.; Li, L.; Grössinger, R. An Approach to Modeling the Dependence of Magnetization on Magnetic Field in the High Field Regime. *J. Magn. Magn. Mater.* **2006**, *300*, 273–283.

(198) Yaln, O.; Lo, C.-K.; Montiel, H.; Alvarez, G.; Sharma, M.; Pathak, S.; Sharma, M.; Widuch, S.; Stamps, R. L.; Skrzypek, D.; Celinski, Z.; Vázquez-Victorio, G.; Acevedo-Salas, U.; Valenzuela, R.; Yoshikiyo, M.; Namai, A.; Ohkoshi, S.; Fu, S.-F.; Wang, X.-Z. *Ferromagnetic Resonance*; Yaln, O., Ed.; InTech, 2013.

(199) Dubs, C.; Surzhenko, O.; Linke, R.; Danilewsky, A.; Brückner, U.; Dellith, J. Sub-Micrometer Yttrium Iron Garnet LPE Films with Low Ferromagnetic Resonance Losses. *J. Phys. D. Appl. Phys.* **2017**, *50*, 204005.

(200) Beaujour, J. M.; Ravelosona, D.; Tudosa, I.; Fullerton, E. E.; Kent, A. D. Ferromagnetic Resonance Linewidth in Ultrathin Films with Perpendicular Magnetic Anisotropy. *Phys. Rev. B - Condens. Matter Mater. Phys.* **2009**, *80*, 180415.

(201) Hurben, M. J.; Patton, C. E. Theory of Two Magnon Scattering Microwave Relaxation and Ferromagnetic Resonance Linewidth in Magnetic Thin Films. *J. Appl. Phys.* **1998**, *83*, 4344–4365.

(202) Kalarickal, S. S.; Mo, N.; Krivosik, P.; Patton, C. E. Ferromagnetic Resonance Linewidth Mechanisms in Polycrystalline Ferrites: Role of Grain-to-Grain and Grain-Boundary Two-Magnon Scattering Processes. *Phys. Rev. B - Condens. Matter Mater. Phys.* **2009**, *79*, 094427.

(203) Man, H.; Shi, Z.; Xu, G.; Xu, Y.; Chen, X.; Sullivan, S.; Zhou, J.; Xia, K.; Shi, J.; Dai, P. Direct Observation of Magnon-Phonon Coupling in Yttrium Iron Garnet. *Phys. Rev. B* **2017**.

(204) Fetisov, Y. K.; Srinivasan, G. Ferrite/Piezoelectric Microwave Phase Shifter: Studies on Electric Field Tunability. *Electron. Lett.* **2005**, *41*, 1066–1067.

(205) Kittel, C. On the Theory of Ferromagnetic Resonance Absorption. *Phys. Rev.* **1948**, *73*,

155.

(206) Man, H.; Shi, Z.; Xu, G.; Xu, Y.; Chen, X.; Sullivan, S.; Zhou, J.; Xia, K.; Shi, J.; Dai, P. Direct Observation of Magnon-Phonon Coupling in Yttrium Iron Garnet. *Phys. Rev. B* **2017**, *96*, 100406.

(207) Kittel, C. Theory of Ferromagnetic Resonance in Rare Earth Garnets. *Phys. Rev.* **1959**, *115*, 1587.

(208) Rosenberg, E. R.; Litzius, K.; Shaw, J. M.; Riley, G. A.; Beach, G. S. D.; Nembach, H. T.; Ross, C. A. Magnetic Properties and Growth-Induced Anisotropy in Yttrium Thulium Iron Garnet Thin Films. *Adv. Electron. Mater.* **2021**, *7*, 2100452.

(209) Dieny, B.; Prejbeanu, I. L.; Garello, K.; Gambardella, P.; Freitas, P.; Lehndorff, R.; Raberg, W.; Ebels, U.; Demokritov, S. O.; Akerman, J.; Deac, A.; Pirro, P.; Adelmann, C.; Anane, A.; Chumak, A. V.; Hirohata, A.; Mangin, S.; Valenzuela, S. O.; Onbaşlı, M. C.; D'Aquino, M.; Prenat, G.; Finocchio, G.; Lopez-Diaz, L.; Chantrell, R.; Chubykalo-Fesenko, O.; Bortolotti, P. Opportunities and Challenges for Spintronics in the Microelectronics Industry. *Nat. Electron.* **2020**, *3*, 446–459.

(210) Slonczewski, J. C. Current-Driven Excitation of Magnetic Multilayers. *J. Magn. Magn. Mater.* **1996**, *159*, L1–L7.

(211) Berger, L. Emission of Spin Waves by a Magnetic Multilayer Traversed by a Current. *Phys. Rev. B* **1996**, *54*, 9353.

(212) Miron, I. M.; Garello, K.; Gaudin, G.; Zermatten, P. J.; Costache, M. V.; Auffret, S.; Bandiera, S.; Rodmacq, B.; Schuhl, A.; Gambardella, P. Perpendicular Switching of a Single Ferromagnetic Layer Induced by In-Plane Current Injection. *Nature* **2011**, *476*, 189–193.

(213) Apalkov, D.; Dieny, B.; Slaughter, J. M. Magnetoresistive Random Access Memory. *Proc. IEEE* **2016**, *104*, 1796–1830.

(214) Parkin, S. S. P.; Hayashi, M.; Thomas, L. Magnetic Domain-Wall Racetrack Memory. *Science.* **2008**, *320*, 190–194.

(215) Parkin, S.; Yang, S. H. Memory on the Racetrack. *Nat. Nanotechnol.* **2015**, *10*, 195–198.

(216) Caretta, L.; Mann, M.; Büttner, F.; Ueda, K.; Pfau, B.; Günther, C. M.; Hessing, P.; Churikova, A.; Klose, C.; Schneider, M.; Engel, D.; Marcus, C.; Bono, D.; Bagschik, K.; Eisebitt, S.; Beach, G. S. D. Fast Current-Driven Domain Walls and Small Skyrmions in a Compensated Ferrimagnet. *Nat. Nanotechnol.* **2018**, *13*, 1154–1160.

(217) Freitas, P. P.; Ferreira, R.; Cardoso, S. Spintronic Sensors. *Proc. IEEE* **2016**, *104*, 1894–1918.

(218) Paz, E.; Serrano-Guisan, S.; Ferreira, R.; Freitas, P. P. Room Temperature Direct Detection of Low Frequency Magnetic Fields in the 100 PT/Hz0.5 Range Using Large Arrays of Magnetic Tunnel Junctions. *J. Appl. Phys.* **2014**, *115*.

(219) Chen, T.; Dumas, R. K.; Eklund, A.; Muduli, P. K.; Houshang, A.; Awad, A. A.; Dürrenfeld, P.; Malm, B. G.; Rusu, A.; Akerman, J. Spin-Torque and Spin-Hall Nano-Oscillators. *Proc. IEEE* **2016**, *104*, 1919–1945.

(220) Liu, L.; Pai, C. F.; Ralph, D. C.; Buhrman, R. A. Magnetic Oscillations Driven by the Spin Hall Effect in 3-Terminal Magnetic Tunnel Junction Devices. *Phys. Rev. Lett.* **2012**, *109*, 186602.

(221) Demidov, V. E.; Urazhdin, S.; Ulrichs, H.; Tiberkevich, V.; Slavin, A.; Baither, D.; Schmitz, G.; Demokritov, S. O. Magnetic Nano-Oscillator Driven by Pure Spin Current. *Nat. Mater.* **2012**, *11*, 1028–1031.

(222) Akpakwu, G. A.; Silva, B. J.; Hancke, G. P.; Abu-Mahfouz, A. M. A Survey on 5G Networks for the Internet of Things: Communication Technologies and Challenges. *IEEE Access* **2017**, *6*, 3619–3647.

(223) Zahedinejad, M.; Awad, A. A.; Muralidhar, S.; Khymyn, R.; Fulara, H.; Mazraati, H.; Dvornik, M.; Åkerman, J. Two-Dimensional Mutually Synchronized Spin Hall Nano-Oscillator Arrays for Neuromorphic Computing. *Nat. Nanotechnol.* **2019**, *15*, 47–52.

(224) Felser, C.; Fecher, G. H.; Balke, B. Spintronics: A Challenge for Materials Science and Solid-State Chemistry. *Angew. Chemie Int. Ed.* **2007**, *46*, 668–699.

(225) Hirohata, A.; Sukegawa, H.; Yanagihara, H.; Zutic, I.; Seki, T.; Mizukami, S.; Swaminathan, R. Roadmap for Emerging Materials for Spintronic Device Applications. *IEEE Trans. Magn.* **2015**, *51*.

(226) Emori, S.; Li, P. Ferrimagnetic Insulators for Spintronics: Beyond Garnets. *J. Appl. Phys.* **2021**, *129*, 20901.

(227) Sinova, J.; Žutić, I. New Moves of the Spintronics Tango. *Nat. Mater.* **2012**, *11*, 368–371.

(228) Quindeau, A.; Avci, C. O.; Liu, W.; Sun, C.; Mann, M.; Tang, A. S.; Onbasli, M. C.; Bono, D.; Voyles, P. M.; Xu, Y.; Robinson, J.; D Beach, G. S.; Ross, C. A.; Quindeau, A.; Avci, C. O.; Mann, M.; Tang, A. S.; Onbasli, M. C.; Bono, D.; D Beach, G. S.; Ross, C. A.; Liu, W.; Xu, Y.; Robinson, J.; Sun, C.; Voyles, P. M. Tm3Fe5O12/Pt Heterostructures with Perpendicular Magnetic Anisotropy for Spintronic Applications. *Adv. Electron. Mater.* **2017**, *3*, 1600376.

(229) Soumah, L.; Beaulieu, N.; Qassym, L.; Carrétéro, C.; Jacquet, E.; Lebourgeois, R.; Ben Youssef, J.; Bortolotti, P.; Cros, V.; Anane, A. Ultra-Low Damping Insulating Magnetic Thin Films Get Perpendicular. *Nat. Commun.* **2018**, *9*, 1–6.

(230) Capku, Z.; Yildiz, F. Spin Wave Modes Observation in YIG Thin Films with Perpendicular Magnetic Anisotropy. *J. Magn. Magn. Mater.* **2021**, *538*, 168290.

(231) Serga, A. A.; Chumak, A. V.; Hillebrands, B. YIG Magnonics. *J. Phys. D. Appl. Phys.* **2010**, *43*, 264002.

(232) Sun, Y.; Wu, M. Yttrium Iron Garnet Nano Films: Epitaxial Growth, Spin-Pumping Efficiency, and Pt-Capping-Caused Damping. In *Solid State Physics - Advances in Research and Applications*; 2013; Vol. 64, pp 157–191.

(233) Onbasli, M. C.; Kehlberger, A.; Kim, D. H.; Jakob, G.; Kläui, M.; Chumak, A. V.; Hillebrands, B.; Ross, C. A. Pulsed Laser Deposition of Epitaxial Yttrium Iron Garnet Films with Low Gilbert Damping and Bulk-like Magnetization. *APL Mater.* **2014**, *2*, 106102.

(234) Lu, Z.; Yang, Y.; Wen, L.; Feng, J.; Lao, B.; Zheng, X.; Li, S.; Zhao, K.; Cao, B.; Ren, Z.; Song, D.; Du, H.; Guo, Y.; Zhong, Z.; Hao, X.; Wang, Z.; Li, R. W. Cooperative Control of Perpendicular Magnetic Anisotropy via Crystal Structure and Orientation in Freestanding SrRuO3 Membranes. *npj Flex. Electron.* **2022**, *6*, 1–8.

(235) Dieny, B.; Chshiev, M. Perpendicular Magnetic Anisotropy at Transition Metal/Oxide Interfaces and Applications. *Rev. Mod. Phys.* **2017**, *89*, 025008.

(236) Ikeda, S.; Miura, K.; Yamamoto, H.; Mizunuma, K.; Gan, H. D.; Endo, M.; Kanai, S.; Hayakawa, J.; Matsukura, F.; Ohno, H. A Perpendicular-Anisotropy CoFeB–MgO Magnetic Tunnel Junction. *Nat. Mater.* **2010**, *9*, 721–724.

(237) Mangin, S.; Ravelosona, D.; Katine, J. A.; Carey, M. J.; Terris, B. D.; Fullerton, E. E. Current-Induced Magnetization Reversal in Nanopillars with Perpendicular Anisotropy. *Nat. Mater.* **2006**, *5*, 210–215.

(238) Spaldin, N. A. *Magnetic Materials: Fundamentals and Applications*, 2nd ed.; Cambridge University Press: New York, 2010.

(239) Patel, S. K.; Karaba, C. T.; Tolbert, S. H. Delineating Magnetization Dynamics in Solution-Processed Doped Yttrium Iron Garnet Thin Films. *J. Appl. Phys.* **2023**, *133*, 014102.

(240) Stadler, B. J. H.; Srinivasan, K. Magneto-Optical Materials and Designs for Integrated TE- and TM-Mode Planar Waveguide Isolators: A Review. *Opt. Mater. Express* **2018**, *8*, 3307–3318.

(241) Carothers, K. J.; Norwood, R. A.; Pyun, J. High Verdet Constant Materials for Magneto-Optical Faraday Rotation: A Review. *Chem. Mater.* **2022**, *34*, 2531–2544.

(242) Fakhrul, T.; Tazlaru, S.; Khurana, B.; Beran, L.; Bauer, J.; Vančík, M.; Marchese, A.; Tsotsos, E.; Kučera, M.; Zhang, Y.; Veis, M.; Ross, C. A. High Figure of Merit Magneto-Optical Ce- and Bi-Substituted Terbium Iron Garnet Films Integrated on Si. *Adv. Opt. Mater.* **2021**, *9*, 2100512.

(243) Mokarian Zanjani, S.; Onbaşlı, M. C. Predicting New Iron Garnet Thin Films with Perpendicular Magnetic Anisotropy. *J. Magn. Magn. Mater.* **2020**, *499*, 166108.

(244) Bauer, J. J.; Rosenberg, E. R.; Kundu, S.; Mkhoyan, K. A.; Quarterman, P.; Grutter, A. J.; Kirby, B. J.; Borchers, J. A.; Ross, C. A. Dysprosium Iron Garnet Thin Films with Perpendicular Magnetic Anisotropy on Silicon. *Adv. Electron. Mater.* **2020**, *6*, 1900820.

(245) Rosenberg, E. R.; Beran, L.; Avci, C. O.; Zeledon, C.; Song, B.; Gonzalez-Fuentes, C.; Mendil, J.; Gambardella, P.; Veis, M.; Garcia, C.; Beach, G. S. D.; Ross, C. A. Magnetism and Spin Transport in Rare-Earth-Rich Epitaxial Terbium and Europium Iron Garnet Films. *Phys. Rev. Mater.* **2018**, *2*, 094405.

(246) Syvorotka, I. I.; Syvorotka, I. M.; Kityk, I. V. Surface Morphological Changes and Magnetic Properties of Sc-Substituted Y3Fe5O12 Epitaxial Films Deposited on the GGG Substrate. *J. Magn. Magn. Mater.* **2010**, *322*, 3314–3319.

(247) Marysko, M. Anisotropy and FMR in Cobalt Doped YIG Films. *IEEE Trans. Magn.* **1994**, *30*, 978–980.

(248) Sturge, M. D.; Gyorgy, E. M.; Lecraw, R. C.; Remeika, J. P. Magnetic Behavior of Cobalt in Garnets. II. Magnetocrystalline Anisotropy and Ferrimagnetic Resonance of Cobalt-Doped Yttrium Iron Garnet. *Phys. Rev.* **1969**, *180*, 413.

(249) Maziewski, A.; Půst, L.; Görnert, P. Magnetometrical Study of Cobalt Doped YIG Garnet Films. *J. Magn. Magn. Mater.* **1990**, *83*, 87–88.

(250) Hansen, P. Contribution of Some 4d and 5d Transition-Metal Ions on Octahedral Sites to the Anisotropy of Ferrites and Garnets. *Phys. Rev. B* **1971**, *3*, 862.

(251) Liu, Q. B.; Meng, K. K.; Xu, Z. D.; Zhu, T.; Xu, X. G.; Miao, J.; Jiang, Y. Unusual Anomalous Hall Effect in Perpendicularly Magnetized YIG Films with a Small Gilbert Damping Constant. *Phys. Rev. B* **2020**, *101*, 174431.

(252) Yoshimoto, T.; Goto, T.; Shimada, K.; Iwamoto, B.; Nakamura, Y.; Uchida, H.; Ross, C. A.; Inoue, M. Static and Dynamic Magnetic Properties of Single-Crystalline Yttrium Iron Garnet Films Epitaxially Grown on Three Garnet Substrates. *Adv. Electron. Mater.* **2018**, *4*, 1800106.

(253) Fu, J.; Hua, M.; Wen, X.; Xue, M.; Ding, S.; Wang, M.; Yu, P.; Liu, S.; Han, J.; Wang, C.; Du, H.; Yang, Y.; Yang, J. Epitaxial Growth of Y3Fe5O12 Thin Films with Perpendicular Magnetic Anisotropy. *Appl. Phys. Lett.* **2017**, *110*.

(254) Wang, H.; Du, C.; Hammel, P. C.; Yang, F. Strain-Tunable Magnetocrystalline

Anisotropy in Epitaxial Y3Fe5 O12 Thin Films. *Phys. Rev. B - Condens. Matter Mater. Phys.* **2014**, *89*, 134404.

(255) Zeyfang, R. Stresses in Epitaxially Grown Single-Crystal Films: YIG on YAG. *J. Appl. Phys.* **1970**, *41*, 3718–3721.

(256) Krysztofik, A.; Özoğlu, S.; McMichael, R. D.; Coy, E. Effect of Strain-Induced Anisotropy on Magnetization Dynamics in Y3Fe5O12 Films Recrystallized on a Lattice-Mismatched Substrate. *Sci. Reports 2021 111* **2021**, *11*, 1–10.

(257) Liu, Y.; Zhou, P.; Bidthanapally, R.; Zhang, J.; Zhang, W.; Page, M. R.; Zhang, T.; Srinivasan, G. Strain Control of Magnetic Anisotropy in Yttrium Iron Garnet Films in a Composite Structure with Yttrium Aluminum Garnet Substrate. *J. Compos. Sci.* **2022**, *6*, 203.

(258) Soumah, L.; Beaulieu, N.; Qassym, L.; Carrétéro, C.; Jacquet, E.; Lebourgeois, R.; Ben Youssef, J.; Bortolotti, P.; Cros, V.; Anane, A. Ultra-Low Damping Insulating Magnetic Thin Films Get Perpendicular. *Nat. Commun. 2018 91* **2018**, *9*, 1–6.

(259) Su, T.; Ning, S.; Cho, E.; Ross, C. A. Magnetism and Site Occupancy in Epitaxial Y-Rich Yttrium Iron Garnet Films. *Phys. Rev. Mater.* **2021**, *5*, 094403.

(260) Lee, A. J.; Guo, S.; Ahmed, A. S.; Yang, F. Crystal Orientation Dependence of Interfacial Magnetic Anisotropy at Heavy-Metal/Magnetic-Garnet Interfaces. *Phys. Rev. B* **2020**, *102*, 174434.

(261) Van Erk, W.; Van Hoek-Martens, H. J. G. J.; Bartels, G. The Effect of Substrate Orientation on the Growth Kinetics of Garnet Liquid Phase Epitaxy. *J. Cryst. Growth* **1980**, *48*, 621–634.

(262) Hsia, L. C.; Wigen, P. E.; De Gasperis, P.; Borghese, C. Enhancement of Uniaxial

Anisotropy Constant by Introducing Oxygen Vacancies in Ca-doped YIG. *J. Appl. Phys.* **1981**, *52*, 2261–2263.

(263) Robertson, J. M.; Neate, B. W. Some Observations on the Growth of YIG under Oxygen Pressure by the "Fluxed Melt" Technique. *J. Cryst. Growth* **1972**, *13–14*, 576–578.

(264) Jha, S. K.; Sharma, M.; Puri, N. K.; Kuanr, B. K. Effect of Oxygen Growth-Pressure on Microstructural and Magnetic Properties of Pulse Laser Deposited Epitaxial YIG Thin Films. *J. Alloys Compd.* **2021**, *889*, 161741.

(265) Bhoi, B.; Mahender, C.; Venkataramani, N.; Aiyar, R. P. R. C.; Prasad, S. Effect of Oxygen Pressure on the Magnetic Properties of Yttrium-Iron-Garnet Thin Films Made by Pulsed Laser Deposition. *IEEE Magn. Lett.* **2016**, *7*.

(266) Swamy, V.; Mi, S.; Huang, H.; Mei, C.; Lu, Y.; Song, D.; Du, H.; Zhao, Y. Structural, Magnetic, and Low-Temperature Electrical Transport Properties of YIG Thin Films with Heavily Reduced Oxygen Contents. *ACS Appl. Electron. Mater.* **2021**, *3*, 3313–3320.

(267) Lehmann-Szweykowska, A.; Szamer, A.; Wojciechowski, R. J.; Micnas, R.; Lulek, T. A Microscopic Model of Oxygen Vacancies in Ca-Doped YIG. *J. Phys. Conf. Ser.* **2006**, *30*, 278.

(268) Gyorgy, E. M.; LeCraw, R. C.; Blank, S. L.; Pierce, R. D.; Johnson, D. W. Dependence of Oxygen Diffusion in Epitaxial YIG : Ca on Defect Concentration. *J. Appl. Phys.* **1978**, *49*, 1885–1887.

(269) Antonini, B.; Blank, S. L.; Lagomarsino, S.; Paoletti, A.; Paroli, P.; Scarinci, F.; Tucciarone, A. Oxidizing Effects of High Temperature Annealing in Reducing Atmosphere in Ca-Doped YIG Films. *J. Magn. Magn. Mater.* **1980**, *20*, 216–219.

(270) Antonini, B.; Brandle, C. D.; Lagomarsino, S.; Paoletti, A.; Paroli, P.; Tucciarone, A.

Surface Layer Contraction of the Lattice in YIG:Ca Films. *J. Appl. Phys.* **1984**, *55*, 2179–2181.

(271) Noun, W.; Popova, E.; Bardelli, F.; Dumont, Y.; Bertacco, R.; Tagliaferri, A.; Tessier, M.; Guyot, M.; Berini, B.; Keller, N. Determination of Yttrium Iron Garnet Superexchange Parameters as a Function of Oxygen and Cation Stoichiometry. *Phys. Rev. B - Condens. Matter Mater. Phys.* **2010**, *81*, 054411.

(272) Dionne, G. F. Molecular Field Coefficients of Substituted Yttrium Iron Garnets. *J. Appl. Phys.* **1970**, *41*, 4874–4881.

(273) Vaqueiro, P.; López-Quintela, M. A. Influence of Complexing Agents and PH on Yttrium-Iron Garnet Synthesized by the Sol-Gel Method. *Chem. Mater.* **1997**, *9*, 2836–2841.

(274) Pal, M.; Chakravorty, D. Synthesis of Nanocrystalline Yttrium Iron Garnet by Sol–Gel Route. *Phys. E Low-dimensional Syst. Nanostructures* **1999**, *5*, 200–203.

(275) Xu, H.; Yang, H.; Xu, W.; Feng, S. Magnetic Properties of Ce,Gd-Substituted Yttrium Iron Garnet Ferrite Powders Fabricated Using a Sol–Gel Method. *J. Mater. Process. Technol.* **2008**, *197*, 296–300.

(276) Zou, G. F.; Zhao, J.; Luo, H. M.; Mc Cleskey, T. M.; Burrell, A. K.; Jia, Q. X. Polymer-Assisted-Deposition: A Chemical Solution Route for a Wide Range of Materials. *Chem. Soc. Rev.* **2013**, *42*, 439–449.

(277) Jia, Q. X.; McCleskey, T. M.; Burrell, A. K.; Lin, Y.; Collis, G. E.; Wang, H.; Li, A. D. Q.; Foltyn, S. R. Polymer-Assisted Deposition of Metal-Oxide Films. *Nat. Mater.* **2004**, *3*, 529–532.

(278) Burrell, A. K.; Mark McCleskey, T.; Jia, Q. X. Polymer Assisted Deposition. *Chemical Communications*. Royal Society of Chemistry March 7, 2008, pp 1271–1277.

(279) Suturin, S. M.; Korovin, A. M.; Bursian, V. E.; Lutsev, L. V.; Bourobina, V.; Yakovlev, N. L.; Montecchi, M.; Pasquali, L.; Ukleev, V.; Vorobiev, A.; Devishvili, A.; Sokolov, N. S. Role of Gallium Diffusion in the Formation of a Magnetically Dead Layer at the Y3Fe5 O12/Gd3Ga5 O12 Epitaxial Interface. *Phys. Rev. Mater.* **2018**, *2*, 104404.

(280) Šimša, Z.; Zemek, J. XPS Investigation of LPE Garnet Films. *Czechoslov. J. Phys.* **1990**, *40*, 1274–1282.

(281) Sawada, H. Electron Density Study of Garnets:Z3Ga5O12;Z=Nd, Sm, Gd, Tb. *J. Solid State Chem.* **1997**, *132*, 300–307.

(282) Blank, S. L.; Nielsen, J. W. The Growth of Magnetic Garnets by Liquid Phase Epitaxy. *J. Cryst. Growth* **1972**, *17*, 302–311.

(283) Cullity, B. D. *Elements of X-Ray Diffraction*, 2nd ed.; Addison-Wesley Publishing Company Inc.: Menlo Park, 1978.

(284) Skiba, E.; Chen, T.; Perry -, N. H.; Ma, Y.; Perry, N. H.; -, al; Frederick Harrington, G.; Sasaki, K.; Hun Kim, D.; Aimon, N. M.; Bi, L.; Florez, J. M.; Dionne, G. F.; Ross, C. A. Magnetostriction in Epitaxial SrTi1−xFexO3−δ Perovskite Films with x = 0.13 and 0.35. *J. Phys. Condens. Matter* **2012**, *25*, 026002.

(285) Büttner, F.; Mawass, M. A.; Bauer, J.; Rosenberg, E.; Caretta, L.; Avci, C. O.; Gräfe, J.; Finizio, S.; Vaz, C. A. F.; Novakovic, N.; Weigand, M.; Litzius, K.; Förster, J.; Träger, N.; Groß, F.; Suzuki, D.; Huang, M.; Bartell, J.; Kronast, F.; Raabe, J.; Schütz, G.; Ross, C. A.; Beach, G. S. D. Thermal Nucleation and High-Resolution Imaging of Submicrometer Magnetic Bubbles in Thin Thulium Iron Garnet Films with Perpendicular Anisotropy. *Phys. Rev. Mater.* **2020**, *4*, 011401.

(286) Rosenberg, E. R.; Litzius, K.; Shaw, J. M.; Riley, G. A.; Beach, G. S. D.; Nembach, H. T.;

Ross, C. A. Magnetic Properties and Growth-Induced Anisotropy in Yttrium Thulium Iron Garnet Thin Films. *Adv. Electron. Mater.* **2021**, *7*, 2100452.

(287) Linares, R. C.; McGraw, R. B.; Schroeder, J. B. Growth and Properties of Yttrium Iron Garnet Single-Crystal Films. *J. Appl. Phys.* **1965**, *36*, 2884–2886.

(288) Geller, S.; Espinosa, G. P.; Crandall, P. B. Thermal Expansion of Yttrium and Gadolinium Iron, Gallium and Aluminum Garnets. *J. Appl. Crystallogr.* **1969**, *2*, 86–88.

(289) Liang, R. S.; Liu, F. C. Measurement of Thermal Expansion Coefficient of Substrate GGG and Its Epitaxial Layer YIG. *Powder Diffr.* **1999**, *14*, 2–4.

(290) Rao, Y.-H.; Zhang, H.-W.; Yang, Q.-H.; Zhang, D.-N.; Jin, L.-C.; Ma, B.; Wu, Y.-J. Liquid Phase Epitaxy Magnetic Garnet Films and Their Applications*. *Chinese Phys. B* **2018**, *27*, 086701.

(291) Krishnan, R.; Paoletti, A.; Paroli, P.; Pisarev, R.; Tucciarone, A. Angular Variation of Magnetic Linear Dichroism in Ru-Doped Yig(+). *IEEE Trans. Magn.* **1981**, *17*, 3223–3225.

(292) Krishnan, R. Crystal Growth and Some Magnetic Properties of Ruthenium Doped YIG. *Phys Stat Sol* **1970**, No. 1, K17–K20.

(293) Solt, I. H. Temperature Dependence of YIG Magnetization. *J. Appl. Phys.* **1962**, *33*, 1189–1191.

(294) O'Handley, R. C. *Modern Magnetic Materials*; John Wiley & Sons, Inc.: New York, 2000.

(295) Mada, J.; Yamaguchi, K.; Uchishiba, H. Magnetocrystalline Anisotropy Energy K1 of Co2+ and Ru3+ Substituted Bubble Garnet Films. *J. Magn. Magn. Mater.* **1983**, *35*, 326–328.

(296) Bauer, J. J.; Rosenberg, E. R.; Ross, C. A. Perpendicular Magnetic Anisotropy and Spin Mixing Conductance in Polycrystalline Europium Iron Garnet Thin Films. *Appl. Phys. Lett.* **2019**, *114*, 52403.

(297) Clark, A. E.; Strakna, R. E. Elastic Constants of Single-Crystal YIG. *J. Appl. Phys.* **1961**, *32*, 1172–1173.

(298) Gilleo, M. A.; Geller, S. Magnetic and Crystallographic Properties of Substituted Yttrium-Iron Garnet. *Phys. Rev.* **1958**, *110*, 73.

(299) Dunitz, J. D.; Orgel, L. E. Electronic Properties of Transition-Metal Oxides-II: Cation Distribution amongst Octahedral and Tetrahedral Sites. *J. Phys. Chem. Solids* **1957**, *3*, 318–323.

(300) Yoon, S. D.; Vittoria, C.; Oliver, S. A. Magnetic and Microwave Magnetic Properties of Barium Hexaferrite Permanent Magnet Films Having the C-Axis in the Film Plane. *J. Appl. Phys.* **2003**, *93*, 4023–4026.

(301) Klingler, S.; Maier-Flaig, H.; Dubs, C.; Surzhenko, O.; Gross, R.; Huebl, H.; Goennenwein, S. T. B.; Weiler, M. Gilbert Damping of Magnetostatic Modes in a Yttrium Iron Garnet Sphere. *Appl. Phys. Lett.* **2017**, *110*, 092409.

(302) Schuster, M.; Göbel, H. Parallel-Beam Coupling into Channel-Cut Monochromators Using Curved Graded Multilayers. *J. Phys. D. Appl. Phys.* **1995**, *28*, A270.

(303) Raghunathan, A.; Nlebedim, I. C.; Jiles, D. C.; Snyder, J. E. Growth of Crystalline Cobalt Ferrite Thin Films at Lower Temperatures Using Pulsed-Laser Deposition Technique. *J. Appl. Phys.* **2010**, *107*, 09A516.

(304) Zhou, J. ping; He, H. cai; Nan, C. W. Effects of Substrate Temperature and Oxygen Pressure on the Magnetic Properties and Structures of $CoFe_2O_4$ Thin Films Prepared by

Pulsed-Laser Deposition. *Appl. Surf. Sci.* **2007**, *253*, 7456–7460.

(305) Hui-Can Mao, G.; Li, Y.-F. The Correlation between Mechanical Stress and Magnetic Anisotropy in Ultrathin Films. *Reports Prog. Phys.* **1999**, *62*, 809.

(306) Sander, D.; Enders, A.; Kirschner, J. Stress and Magnetic Properties of Surfaces and Ultrathin Films. *J. Magn. Magn. Mater.* **1999**, *200*, 439–455.

(307) Zembilgotov, A. G.; Pertsev, N. A.; Kohlstedt, H.; Waser, R. Ultrathin Epitaxial Ferroelectric Films Grown on Compressive Substrates: Competition between the Surface and Strain Effects. *J. Appl. Phys.* **2002**, *91*, 2247.